Quantitative Optical Gas Imaging using Broadband Mid-wavelength Infrared Single-Channel and Multispectral Cameras

by

Michael Christopher Nagorski

A thesis

presented to the University of Waterloo

in fulfillment of the

thesis requirement for the degree of

Master of Applied Science

in

Mechanical and Mechatronics Engineering

Waterloo, Ontario, Canada, 2022

Author’s Declaration

I hereby declare that I am the sole author of this thesis. This is a true copy of the thesis, including any required final revisions, as accepted by my examiners.

I understand that my thesis may be made electronically available to the public.

Abstract

Methane is a potent greenhouse gas that is the main component of natural gas and a by-product of crude oil extraction. Quantifying and limiting methane emissions from upstream oil and gas is an efficient strategy to reduce anthropogenic climate change and has received considerable attention from regulators in recent years. Quantification technologies are needed to address this problem and quantitative optical gas imaging (QOGI) using broadband mid-wavelength infrared (MWIR) cameras is a promising solution that can provide instantaneous flow rate estimates over large areas and at a distance. Optical gas imaging (OGI) has become the standard for leak detection and repair (LDAR) surveys in the oil and gas industry, and quantification systems that utilize these cameras are now being used in the field but their limitations and accuracy have not been adequately studied. Independent research on the accuracy of these QOGI systems in controlled and real-world conditions is needed. Further, these single-channel camera systems contain a single bandpass filter which makes their estimates sensitive to uncertain gas temperature. Multispectral broadband MWIR cameras integrate multiple bandpass filters to provide unique spectral information which can be used to infer additional parameters such as the gas temperature. Multispectral OGI cameras have been used to quantify methane path concentrations in literature, but further research is needed to fully demonstrate their QOGI capabilities and assess their accuracy.

This thesis seeks to fill these knowledge gaps in broadband MWIR QOGI. A spectroscopic model is developed to obtain column density estimates based on the pixel intensities measured by the camera. The column densities are combined with the apparent velocity of the pixels from an optical flow velocimetry model to yield instantaneous flow rate estimates. The QOGI algorithms are experimentally-validated using a FLIR GF320 and controlled release apparatus that releases methane

at controlled flow rates and ambient temperature. The algorithms are benchmarked against the FLIR QL320 quantification system which is a commercial tablet-based software that works with the GF320. The 15 Hz frame rate of the GF320 posed a problem for the optical flow velocimetry, but using an average velocity based on the flow rate and exit diameter resulted in an average error of -10% to -19%. Meanwhile, the QL320 had an average error of +18% to -55% depending on the choice of wind speed setting which affects the cross-correlation velocimetry algorithm used by the software. The in-house QOGI algorithms and QL320 were then tested with methane heated to 55°C to examine the effect of uncertain gas temperature. The in-house QOGI algorithms now overpredicted the actual release rate by +21% to +37% while the QL320 estimates were between 5-times lower and 5-times higher depending on the assumed temperature and wind speed setting. This result highlights the importance of an accurate gas temperature to QOGI estimates and motivates the study of multispectral QOGI. Field testing of the GF320 and QL320 was done in conjunction with a PTAC- and CRIN-funded project focused on assessing methane quantification technologies including QOGI. The QL320 had an average error of -46% while the in-house spectroscopic model combined with wind anemometry data had an average error of -35%.

Multispectral QOGI was explored using the Telops FAST M150 MWIR multispectral camera which has a four-filter fixed-position filter wheel. Initial experimental observations revealed that the radiometric temperature and in-band radiance values from the calibrated measurements were not accurate in the filtered channels for low temperatures which made QOGI infeasible. This problem was diagnosed to be caused by emission from the ambient temperature filters. Manual calibrations were performed indoors at 21°C and outdoors at 8°C which would lower the filter temperatures. The resulting calibration curves indicated a decrease in filter emission but the amount of cooling was insufficient to perform QOGI. Optical flow velocimetry was still able to be performed on the images obtained using

the controlled release apparatus thanks to the 100 Hz frame rate used, and the estimated velocities were deemed to be reasonably accurate but probably slightly underpredicted the true velocities. To overcome the warm filter emission problem, a CFD-large eddy simulation of a CH_4 and CO_2 plume was used with a camera and noise model to generate synthetic images which could be used to validate the multispectral QOGI algorithms. The QOGI estimates mostly underpredicted the ground truth by 20% or less. The column densities were shown to be very accurate while the estimated velocities were quite accurate most of the time but had many fluctuations which was the main source of error. Field measurements using the FAST M150 were performed on a methane flare and combustor but due to the limited filter selection and their calibration ranges, only the optical flow velocimetry could be tested. The results were encouraging as the velocities were relatively close to the wind speed at the time. Qualitative observations based on the different filter channels were difficult to make due to the unsynchronized acquisition.

Acknowledgements

This degree has been a tremendous learning experience and I would like to acknowledge all of those that made it possible.

I would like to thank my supervisor, Professor Kyle Daun, for being an amazing, helpful, knowledgeable, interesting, passionate, caring person and teacher. Your talent and enthusiasm in teaching drew me towards the study of heat transfer and I am so happy that I was able to pursue a master's degree under your guidance. The lab group that you have created is full of so many smart, incredible, and diverse people and I believe you make everyone feel welcome and supported all the time. You are one of the hardest working people that I know and still I can hardly understand how you manage to do everything that you do. Thank you for everything.

I would like to thank all my colleagues in the WatLIT lab that I have had the pleasure of working with during my time. You are all incredibly smart and I appreciate all the help and feedback I've received from you on my research. The Friday night online Skribbl and Codewords games were a highlight of the COVID lockdowns. Special thanks to those I've worked most closely with on QOGI: Rodrigo Miguel, Sina Talebi-Moghaddam, and Paule Lapeyre. I have learned so much from you and you have been extremely valuable in my research.

I would like to thank Kirk Osadetz from CMC Research Institutes, Matthew Johnson from Carleton University, and Robert Davies from the Southern Alberta Institute of Technology for lending me their cameras and tablets which enabled this research. I would like to thank Martin Chamberland and Jean-Philippe Gagnon at Telops for training and technical support. I would also like to thank all those that funded this research, including the University of Waterloo, NSERC, PTAC, CRIN, Alberta Innovates, and the governments of Ontario, Alberta, and Canada.

Last but definitely not least, I would like to thank my parents Anatol and Agnieszka Nagorski. Thank you for supporting me, instilling me with good values, and providing me with the opportunity to live and be educated in Canada. Your hard work and love has motivated and enabled me to achieve all that I have and more still.

Table of Contents

List of Figures

List of Tables

Chapter 1

Introduction

Oil and gas transformed human society during the industrial revolution as energy dense fuels which enabled manufacturing, transportation, and other industries. Today, oil and gas are responsible for an estimated 29% and 24% share of global energy production, respectively [1][2]. Unfortunately, production and consumption of fossil fuels releases harmful greenhouse gases (GHG) and contributes to climate change. Further, crude oil and natural gas are finite resources and so the world must transition to renewable energy sources to prevent the worst outcomes of climate change and ensure a sustainable energy future. Still, oil and gas production will likely persist to provide energy security and as a component to many products. As the world continues to rely on oil and gas now and into the future, it is important to understand and quantify the impact of the use of this resource.

Countries that have signed the Paris Agreement are obliged to reduce GHG emissions as soon as possible. Canada's 2030 Emissions Reduction Plan aims to reduce total emissions by 40% below 2005 levels by 2030 and net-zero by 2050 [3]. Considerable attention has focused on developing new ways of measuring GHG emissions to monitor and meet these goals. Methane (CH_4) emissions from Canada's oil and gas sector receive special attention because methane has a 72-times greater global warming potential than CO_2 over 20 years [4]. Several studies in the past decade have indicated that fugitive and vented methane emissions are significantly higher than previous estimates [5][6][7]. In 2020, CH_4 accounted for 14% of Canada's total CO_2 equivalent emissions, primarily from oil and gas systems but also agriculture and landfills [8]. Quantifying and reducing methane emissions from upstream oil and gas is an efficient strategy to maximize impact.

Natural gas is predominately methane and can be found in reservoirs of porous rock, coal, and crude oil. It is then separated, stored, and further processed as needed [9]. Methane emission can happen

at several points during extraction and production as shown in Figure 1, and span a wide range of emission rates from 400 kg/hr to 0.5 kg/hr or less. Vented emissions are deliberate releases of excess gas to maintain safe operating conditions, while fugitive emissions are unintentional leaks. Vented hydrocarbon emissions can be converted into less potent CO_2 through flaring. The contribution of each emission source to total inventories is an important topic of study so that efforts can be focused on reducing emissions from the largest and most common sources [10][11]. This necessitates the use of different techniques that are capable of screening and quantifying emissions at all scales. Recent studies have explored satellite, aircraft, drone, mobile truck, fixed sensor, and handheld technologies but conclude that more work needs to be done to evaluate their performance in terms of screening and quantification [12][13]. A synergistic approach wherein large spatial scale techniques screen and direct higher accuracy close-range techniques may be the most effective and accurate strategy. Quantification techniques that allow for stand-off or fence line emission measurements are desirable, in part because many of the sites and equipment are inaccessible and dangerous. Quantitative optical gas imaging (QOGI) is well-suited to address these challenges because of its ability to capture instantaneous emission rates over small and large areas and at a distance.

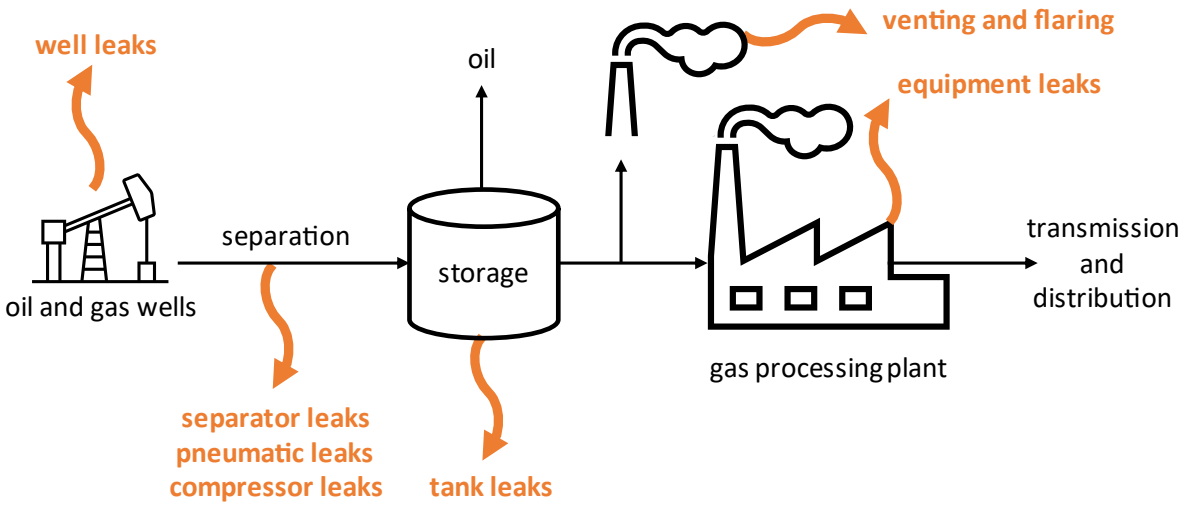

Figure 1: Schematic of oil and gas extraction and production and common sources of methane emission

Mid-wavelength infrared (MWIR) cameras equipped with bandpass filters can qualitatively visualize either absorption or emission by hydrocarbon gases from the principal C-H bond stretching mode provided there is sufficient column density (concentration along a line-of-sight, LOS) and temperature contrast with the background. QOGI takes this a step further and implements a spectroscopic model that relates the pixel intensities to the background temperature and gas thermodynamic state along the LOS. This measurement model can be inverted to estimate the column density, which is combined with the projected velocities inferred from an optical flow velocimetry model to obtain a mass flow rate estimate.

1.1 Current state of QOGI

Infrared imaging systems were first developed in the 1960s and further developed alongside CCD sensors in the 1970s and CMOS sensors in the 1990s [14][15][16][17]. The use of IR imaging for the visualization of gases can be traced to at least the 1980s [18][19]. The Canadian Environmental

Protection Act, 1999 was appended in 2020 to require oil and gas producers to establish and maintain a leak detection and repair (LDAR) program to control volatile organic compound (VOC) emissions [20]. In recent years, optical gas imaging (OGI) cameras have become the standard for conducting LDAR surveys in industrial settings [12].

OGI cameras exist in several forms. Active gas cameras illuminate the gas within the scene (e.g. with a tunable diode laser) and image the reflected and/or backscattered light [21][22], while passive cameras measure radiation emitted by the gas and its background [23][24]. Passive OGI cameras can be further classified into: single-channel (SC), multispectral (MS), and hyperspectral (HS) cameras. A SC OGI camera consists of a single bandpass filter and infrared detector that integrates spectral intensity over the transparent band to produce an infrared image. MS cameras integrate multiple bandpass filters, often mounted on a filter wheel, that produce multiple broadband images over different wavelength ranges [25][26]. HS cameras typically utilize a Fourier-transform infrared spectrometer (FTIR) to produce image hypercubes where each pixel includes high-resolution spectral intensity data [27][28][29]. Advancing from single-channel to multispectral to hyperspectral imaging introduces more spectral information about the scene which is beneficial to inferring the gas species, concentrations, and temperatures but with the trade-offs of complexity, cost, and temporal resolution. This research focuses on passive single-channel and multispectral cameras.

Several methods to quantify gas flow rates based on OGI measurements have emerged. The least sophisticated approach involves various methods of OGI screening, counting emissions, and applying emissions factors based on other quantitative estimates [30]. Another approach uses a model of a frictionless nozzle, a Gaussian dispersion model, the environmental conditions, the minimum detectable path concentration of the camera, and the size of the plume from the OGI image to infer the

leak rate. The accuracy is largely limited by the uncertainty in wind speed which governs the plume transport and the accuracy of the minimum detectable path concentration [31].

Another group of methods use the values measured by the IR camera to determine the path concentrations of gas. These methods can be divided into two types: the first performs reference experiments to correlate the difference between gas-containing and background pixel values to known path concentrations of gas at a known temperature [32][33][34]; the second uses a spectroscopic and radiative transfer model and inversion methods to infer the path concentration as well as temperature and other parameters as long as there is sufficient spectral information [28][29]. The path concentrations are then combined with velocities obtained from image-correlation or optical flow velocimetry to yield flow rate estimates [35][36]. The main limitation of the first type of method is that it relies on knowing the gas temperature which means uncertain gas temperature will introduce errors. The second type of method is more robust as long as an OGI camera that produces enough spectral information or appropriate assumptions are used.

Two QOGI systems are known to have been developed and currently in-use in industry: the FLIR QL320 and Opgal EyeCSite. These systems have tablet-based software that pair with their respective OGI cameras to provide emissions rate estimates of CH_4, VOCs, and CO_2. They are believed to be based on the background-subtraction and path concentration correlation method described above from the available patents and literature [33][34][37]. Since the OGI cameras made by FLIR and Opgal have become the standard in LDAR surveys, these QOGI systems can be quickly and conveniently deployed in industry but their accuracy requires further independent study. A 2017 study by Concawe, a division of the European Fuel Manufacturers Association, performed controlled-release field experiments using the Providence Photonics QL100 which is the predecessor to the QL320. 31 quantifications were made with propane, propylene, and methane with concrete, metal, brick, sky, and cool wet towel backgrounds

but only two tests used methane [38] which has a lower absorption cross-section than propane and propylene [39] and therefore has a lower detectability which may reduce QOGI accuracy. A 2018 study by the Saskatchewan Research Council performed controlled-release field experiments using the QL320 and investigated the impact of wind speed, ambient temperature, temperature contrast with the background, and distance. The study concluded that the QL320 measurements are expected to be within +/- 30% of the actual flow rate if the temperature contrast with the background is greater than 10°C, the flow rate is between 5 and 10 L/min, and a large number of samples are collected [40]. A 2020 study called the Alberta Methane Field Challenge involved several quantification technologies with QOGI using the QL320 acting as the baseline. The study claimed an 18% aggregate error for flow rates ranging from 10 scfh to over 3000 scfh (4.7 SLPM to 1400 SLPM) but once again individual measurements were sometimes up to an order of magnitude less than or greater than the actual release rate [41]. These results indicate that QOGI is not a perfect quantification solution and its accuracy deserves to be studied further to understand the cause of often egregious estimates and identify potential improvements.

Integrated QOGI systems using multispectral and hyperspectral cameras have not reached the market but QOGI using these types of cameras has been demonstrated in literature. ONERA, the French Aerospace Lab, has developed a prototype cooled-filter long-wavelength infrared (LWIR) multispectral camera and demonstrated its ability to infer path concentrations of methane in the field but provides minimal discussion of methods or accuracy [42]. Other research has used a warm-filter MWIR multispectral camera to infer temperature and column densities of CO_2 in a propane Bunsen flame with encouraging results [43]. Several papers have demonstrated QOGI using hyperspectral cameras [28][29][44] but the cost and complexity associated with the hardware and data analysis is a barrier to commercialization. Multispectral QOGI provides additional spectral information leading to more

robust estimates compared to single-channel measurements, at relatively low cost and complexity compared to hyperspectral QOGI.

Recent QOGI-related research is exploring the use of machine learning to retrieve concentrations and temperatures of NOx, CO_2, H_2O, and CO using hyperspectral data [45][46], and computer vision to automatically identify natural gas plumes [22][47]. Determining the detection limits of OGI and QOGI is another area of ongoing research [48][49][50] as well as uncertainty quantification of QOGI estimates due to model, technological, and human errors. A recent paper evaluated the model error associated with projecting a 3D plume into a 2D image for quantification and recommended using at least 10 second average measurements for flow rate estimates to minimize the error of concern [51].

1.2 Thesis outline

This thesis focuses on the use of broadband mid-wavelength infrared single-channel and multispectral cameras for quantitative optical gas imaging. The current state-of-the-art lacks sufficient independent research on the accuracy and limitations of commercial QOGI systems deployed in the field. The effect of uncertain gas temperature on their estimates is likely known to those well-versed in QOGI, but it has not been demonstrated in literature. Multispectral QOGI is a sensible upgrade from single-channel systems but has not been adequately explored in literature for its benefits in the quantification of methane and other GHG emissions in the oil and gas industry. This thesis aims to address these gaps by studying the accuracy of MWIR single-channel QOGI systems and the application of multispectral MWIR cameras to the field. Specifically, the objectives of this thesis are to:

- Develop robust QOGI models and inversion algorithms that can be used with single-channel and multispectral OGI cameras to infer methane flow rates,

- Test the algorithms on a lab-scale controlled release apparatus to assess their accuracy against known flow rates,
- Benchmark the algorithms against established QOGI systems and investigate suspected limitations,
- Demonstrate the difference in capabilities between single-channel and multispectral QOGI cameras,
- Test the QOGI systems in the field to evaluate their performance in real-world conditions,
- Explore the challenges encountered and consider potential improvements.

1.3 Non-candidate contributions

This research builds upon the models, codes, experiments, simulations, and other work done by other graduate students under the supervision of Professor Kyle Daun. The specific contributions are listed here:

- Rodrigo B. Miguel, PhD – MATLAB scripts for QOGI using hyperspectral and multispectral cameras, CFD-LES simulation input files, construction of original controlled release apparatus, lab training, experimental testing, and personal research support.
- Samuel J. Grauer, PhD – MATLAB scripts used in the spectroscopic model.
- Sina Talebi-Moghaddam, PhD – Lab training, experimental testing, and personal research support.
- Paule Lapeyre, PhD – Experimental testing and personal research support.

Chapter 2

Theory for Quantitative Optical Gas Imaging

This chapter serves to introduce the necessary theory to understand QOGI and the current state-of-the-art.

2.1 Physics of participating media

QOGI relies on radiation heat transfer in participating media and infrared imaging to obtain emission rate estimates. Radiation heat transfer is the transfer of energy through electromagnetic (EM) waves that are spontaneously emitted due to the finite temperature of matter. Energy levels at the atomic scale are quantized and all matter with finite temperature will experience spontaneous fluctuations between energy levels. These fluctuations result in the emission or absorption of photons or EM waves with energies equal to the difference in energy between quantized levels [52]. The energy carried by a wave is equal to the wave frequency times Planck's constant

$$E = h\nu \tag{1}$$

These EM waves can propagate through a vacuum or matter, and the absorption or emission of this energy by a medium can be used to characterize the species, path concentration, and temperature.

Polar diatomic and polyatomic gas molecules have rotational and vibrational energy states wherein transitions result in the absorption and emission of photons with frequencies in the infrared spectrum [52]. A photon can be spontaneously emitted with energy equal to the drop in rotational-vibrational energy states, or a photon can be absorbed if an incident photon closely matches the energy required to elevate to a higher energy state. Chemical bonds and gas molecules possess unique quantum energy states which allows the gas species to be identified by the frequency of light emitted or absorbed – this

is called *spectroscopy*. Higher temperature molecules result in a greater probability of quantum transitions occurring due to the increased kinetic energy. A higher number density of gas molecules also increases the probability of emissions and absorptions. This describes the relationship between the amount and frequency of EM radiation emitted or absorbed by a gas species along a path to its temperature and concentration which can be used to characterize the medium.

The attenuation of radiative intensity I_λ by a gas due to absorption along a path interval ds is described by

$$\frac{dI_\lambda}{ds} = -\kappa_\lambda I_\lambda \tag{2}$$

where κ_λ is the spectral absorption coefficient [m^{-1}]. The spectral absorption coefficient quantifies the amount of light of a particular wavelength or frequency that is absorbed by a given volume and is a function of the spectral lines of the species (or mixture of species) in the path, the local gas volume fraction, temperature, and pressure. For monodispersed matter like molecular gases, κ_λ can be calculated from the product of the absorption cross-section $C_{abs,\lambda}$ [m^2/molecule] and the number density of gas N [molecules/m^3]

$$\kappa_\lambda = C_{abs,\lambda} N \tag{3}$$

The absorption cross-section of a molecule is calculated by summing the contributions of each rotational-vibrational line. The contribution of each line is a function of the line strength and line shape function which can be found using a line spectrum database like HITRAN [53] and the thermodynamic state of the gas, namely the local temperature, pressure, and species volume fraction.

For gas molecules like methane and carbon dioxide and over the path lengths relevant to QOGI, scattering at infrared wavelengths is negligible compared to absorption because the molecule diameter is much smaller than the wavelength of light and so the EM wave does not significantly interact.

Gas molecules also emit thermal radiation. Kirchhoff's law states that the spectral, directional emissivity is equal to the spectral, directional absorptivity in order to satisfy the Second Law of Thermodynamics. Applying this to a single LOS through a gas means the spectral absorption coefficient can be used for both the emitted blackbody intensity and attenuated background intensity. The change in radiative intensity along a path interval containing a volume of gas then becomes

$$\frac{dI_\lambda}{ds} = -\kappa_\lambda I_\lambda + \kappa_\lambda I_{\lambda,\mathrm{b}}(T) \tag{4}$$

where $I_{\lambda,\mathrm{b}}(T)$ is the blackbody intensity at gas temperature T. The first term on the right-hand side represents the absorption by the gas and the second term represents the emission. This is called the differential form of the radiative transfer equation (RTE).

2.2 QOGI spectroscopic model

Equation (4) can be integrated along a LOS that extends from a surface or infinity to the camera, which yields an equation for the spectral intensity received at the camera. Expressed in terms of wavenumber η, the spectral intensity along the LOS entering the camera aperture $I_{\eta L}$, is modeled by

$$I_{\eta L} = I_{\eta 0} \exp\left\{-\int_0^L \kappa_\eta(s)\,ds\right\} + \int_0^L \kappa_\eta(s) I_{\eta,\mathrm{b}}\left[T(s)\right] \exp\left\{-\int_s^L \kappa_\eta(s)\,ds'\right\} ds \tag{5 [29]}$$

where s is a location along the LOS with $s = L$ corresponding to the camera aperture, and $I_{\eta 0}$ is the background spectral intensity, which is known by measuring pixels outside the plume. This is the integral form of the RTE and is illustrated in Figure 2 (left). The first term on the right-hand side

represents the background intensity attenuated by the gas along the LOS, while the second term represents gas emission and self-absorption. This equation serves as the model and the solution aims to minimize the difference between the measured pixel intensity and modeled pixel intensity in a least-squares sense.

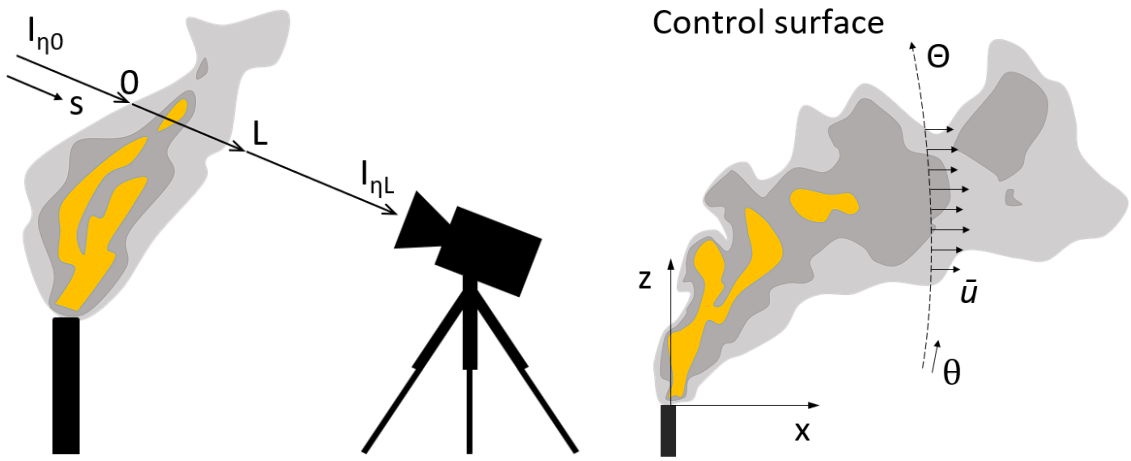

Figure 2: Schematic for understanding QOGI (left) integrated camera LOS intensity (right) plume coordinate system and control surface

The pixel intensity is a function of the gas thermodynamic state along the LOS which cannot be known exactly. The pressure along the LOS will be ambient pressure since the plume is unconstrained by any boundaries. However, the local temperature and species volume fraction will have non-uniform distributions due to unsteady flow. The distribution of these state variables has an impact on $I_{\eta L}$ as seen in the integrated RTE and an infinite number of distributions can explain the measured intensity which makes the problem ill-posed. An infinite combination of temperatures and species volume fractions can also explain the measured pixel intensity which also increases the ill-posedness of the inverse problem. Prior information must be introduced in order to constrain the problem and obtain a unique solution.

For turbulent plumes a Gaussian plume profile with a peak volume fraction, peak temperature, and plume depth is assumed [29]. This reduces the number of parameters to be inferred to two plus the

number of species of interest. For example, if we wish to estimate the combustion efficiency of a methane flare the species of interest are CH_4 and CO_2 so we need four parameters: 1) peak CH_4 volume fraction, 2) peak CO_2 volume fraction, 3) peak temperature, and 4) plume depth. Additional prior information can be used to reduce the number of inferred parameters if the gas is at a known temperature (e.g. ambient) and if the plume is assumed to be axisymmetric so that the plume depth can be measured from the plume profile perpendicular to the LOS (i.e. along the control surface chosen in the image). Prior information on the plume LOS distribution is necessary due to the limitations of 2D imaging on a 3D plume, but the other priors mentioned are not necessary when there is additional spectral information available (i.e., multispectral and hyperspectral measurements) which allows multiple parameters to be inferred.

The measured pixel intensity can be higher or lower than the background intensity depending on the relative temperatures of the gas and background. When the gas temperature is higher than the background, the gas emits with a higher blackbody intensity than the background and the measured pixel intensity will be higher than the background – this is called a "white plume." When the gas temperature is lower than the background, the gas absorbs radiation relative to the background and the measured pixel intensity will be lower than the background – this is called a "black plume." It should be noted that a temperature difference between the background and gas species is required in order to visualize the gas, since otherwise the emitted and absorbed spectral intensities by the gas are identical and there is no net radiative transfer along the LOS.

The column density is the density of gas along the LOS of a pixel and can be formulated using the ideal gas law

$$\rho = \frac{M}{A}\int_0^L \frac{\chi(s)\,p}{k_B T(s)}\,ds \qquad (6)\ [29]$$

where M is the molar mass of the gas species, A is Avogadro's number, $\chi(s)$ is the species volume fraction at location s, p is the total pressure, and k_B is Boltzmann's constant.

2.3 QOGI velocimetry model

The column densities are combined with a 2D-projected velocity field inferred from a sequence of images to obtain the mass flow rate across an arbitrary control surface. In reality the velocity field of the plume is 3D, but it is not possible to infer the velocity component or distribution along the LOS. Instead QOGI infers an intensity-weighted 2D velocity field using the broadband infrared images of the plume. The pixel intensities of each image are analyzed in sequence using a mathematical model that infers the apparent motion of each pixel in the plane of the image – this is called *optical flow*. If there is no background or foreground motion between images, this is a reasonable approximation of the average velocity of the gas within a pixel.

There are several optical flow models that can be used. This research focuses on algorithms developed by Horn-Schunck [54] and Lucas-Kanade [55]. Both algorithms are based on a brightness constancy assumption which states the brightness E of a particular point in a pattern is constant. Using the chain rule of differentiation this can be represented in a mathematical equation that relates the brightness gradients in space and time of a pixel, E_x E_y E_t, to the 2D velocity components u and v.

$$\frac{dE}{dt} = \frac{\partial E}{\partial x}\frac{dx}{dt} + \frac{\partial E}{\partial y}\frac{dy}{dt} + \frac{\partial E}{\partial t} = 0 \tag{7}$$

$$E_x u + E_y v + E_t = 0 \tag{8}$$

This assumption is based on the idea of constant brightness surfaces or objects which create patterns in the image plane. These patterns can be identified using the brightness gradients of the pixels in space, and the brightness of individual pixels change due solely to the apparent motion of the patterns across the image. Equation (8) has two unknown velocity components for each pixel, however, so the matrix is rank-deficient and additional information is needed to fully constrain the solution. The Horn-Schunck and Lucas-Kanade algorithms differ on the nature of this prior information and how it is incorporated into the velocity estimation.

The Horn-Schunck algorithm imposes a smoothness constraint which assumes the patterns are objects that undergo rigid motion so neighboring pixels have similar velocities. While a gas plume is not rigid, the assumption is reasonably accurate for small displacements between frames (i.e. low gas velocities relative to the camera frame rate). This is expressed mathematically by minimizing the Laplacians of the velocity components.

$$\nabla^2 u = \frac{\partial^2 u}{\partial x^2} + \frac{\partial^2 u}{\partial y^2} \tag{9}$$

$$\nabla^2 v = \frac{\partial^2 v}{\partial x^2} + \frac{\partial^2 v}{\partial y^2} \tag{10}$$

The Lucas-Kanade algorithm imposes a different form of smoothness constraint by dividing the image into smaller windows and assuming a constant velocity in each window. The solution amounts to minimizing Equation (11) for each window Ω. W is a matrix that weighs the brightness constancy

constraint differently for each pixel in the window and is analogous to the Laplacian operator in the Horn-Schunck algorithm.

$$\sum_{x \in \Omega} W^2 \left[E_x u + E_y v + E_t \right] \tag{11}$$

With these additional smoothness constraints, there are more equations than unknowns for each pixel and the two velocity components can be solved for using least-squares minimization. The velocity component normal to the control surface is then multiplied by the column density and integrated along the control surface to obtain the mass flow rate

$$\dot{m} = \int_0^{\Theta} \rho(\theta) u(\theta) \, d\theta \tag{12}$$

which is illustrated in Figure 2 (right).

2.4 Infrared detectors and spectral considerations

Infrared detectors are primarily classified into two types: thermal detectors and photon detectors [14][15]. Thermal detectors, also called bolometers, rely on a change in temperature of the sensor material due to the incident infrared radiation which changes some physical property of the material that can be converted into an electrical signal. Thermal detectors are inexpensive but suffer from low sensitivity and slow frame times. Photon detectors consist of a narrow-gap semiconductor called the focal plane array (FPA) that reacts to incident photons of a specific frequency range and a readout integrated circuit (ROIC) that measures and digitizes the incoming signal. This is very similar to the design of CMOS sensors in consumer cameras. However, silicon-based photodetectors are not sensitive to infrared wavelengths so different materials are used, typically indium antimonide (InSb) and mercury cadmium telluride (MCT or HgCdTe). Infrared radiation incident on these materials excites electrons

in the valence band so they may jump to the conduction band and then be measured by the ROIC. More photons and photons of higher energy will generate more excited electrons and a higher signal. Therefore, the signal is proportional to the time-integrated total irradiation of a pixel over the frequency range to which the material is sensitive. These sensors must be cooled to cryogenic temperatures to minimize the electrical noise generated by the movement of charge carriers in the FPA due to their thermal energy which greatly increases the cost. Despite this disadvantage, photon detector-type IR cameras are preferred in QOGI because of their superior sensitivity and frame rates.

Broadband infrared cameras produce a signal that is proportional to the integrated spectral intensity incident on the FPA. FPA materials can be specifically designed to be sensitive to certain wavelengths, and most IR cameras are designed to operate either in the mid-wavelength infrared (MWIR, 3–5 μm) or long-wavelength infrared (LWIR, 7–12 μm). To prevent unwanted frequencies of light from being measured or damaging the FPA, a bandpass filter or specially coated lens is used to block these frequencies. The FLIR GF320 is an example of a MWIR camera that is specifically designed to image hydrocarbons in the 3.2–3.4 μm range using a bandpass filter. Multispectral cameras like the Telops FAST M150 integrate multiple bandpass filters, often mounted on a filter wheel, that produce multiple broadband images over different wavelength ranges. The filter wheel can be fixed in position for a measurement, or certain models can rotate the filter wheel in-sync with the camera frame rate so that different wavelength ranges are imaged sequentially. Other multispectral cameras have the filter wheel fixed and use separate lenses for each bandpass filter to image each wavelength range simultaneously on the same FPA [42].

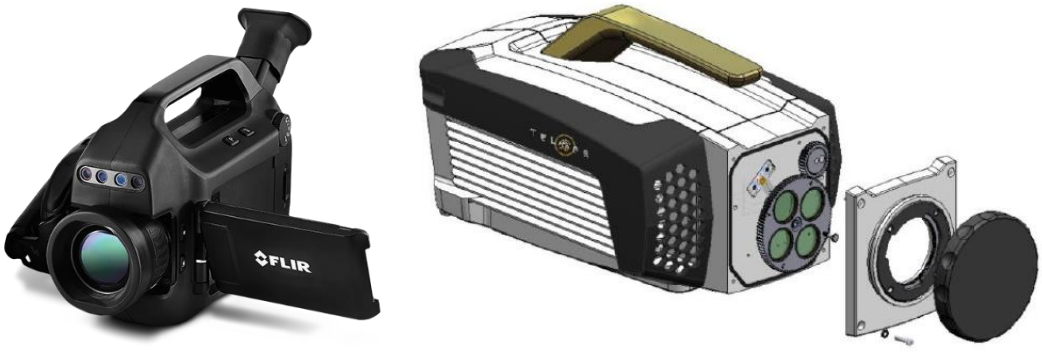

Figure 3: (left) FLIR GF320 single-channel camera (right) Telops FAST M150 multispectral camera

Methane has transition lines in the mid-wavelength IR range of 3.15–3.45 μm (2900–3175 cm^{-1}) and long-wavelength IR range of 7.2–8.2 μm (1220–1390 cm^{-1}). Carbon dioxide has transition lines in the mid-wavelength IR range of 4.18–4.38 μm (2280–2390 cm^{-1}) and long-wavelength IR range of 14–16 μm (625–715 cm^{-1}). Both MWIR and LWIR cameras are capable of QOGI but the appropriate camera should be used for different species of interest.

2.5 Broadband IR camera calibration

The signals produced by a broadband IR camera must be related to more useful quantities like the incident intensity or radiometric temperature through calibration. This is done by relating the signal produced while observing a known reference to the intensity or temperature of the reference. Blackbody radiation sources with temperature control can be used to produce a known amount of radiation for the camera. The blackbody spectral intensity $I_{\lambda,\mathrm{b}}$ produced by the calibration source is given by Planck's law.

$$I_{\lambda,\mathrm{b}}(\lambda,T)=\frac{2hc_0^2}{\lambda^5\left[\exp\left(hc_0/\lambda k_{\mathrm{B}}T\right)-1\right]} \tag{13}$$

The intensity received at the IR sensor I_b is the incident spectral intensity at the camera lens $I_{\lambda,i}$ times the spectral transmittance of the lens and any filters $\zeta(\lambda)$ integrated over the spectral range of the sensor

$$I_b = \int \zeta(\lambda) I_{\lambda,i} d\lambda \tag{14}$$

Assuming a clear LOS to the blackbody source with negligible emission or attenuation the incident intensity is equal to the blackbody intensity given in Equation (13).

The manufacturing processes of the unique materials used in the FPA are less mature compared to silicon, which makes producing high quality, high resolution sensors challenging. Each pixel in the FPA tends to have a unique signal gain and offset which must be corrected for with calibration. This process is called non-uniformity correction (NUC). Assuming the sensor has a linear response to the measured intensity I_b, the measured signal M [counts] is

$$M = g \cdot I_b + o \tag{15}$$

where g is the gain and o is the offset. A two-point calibration of a blackbody source at different temperatures and equal exposure times allows the unique gain and offset to be calculated for each pixel which are then applied to the raw signal to obtain the NUC signal C [counts]. The next step of the calibration procedure is to relate the NUC counts to the band-integrated radiance [W/m^2-sr] or radiometric temperature [K] of the scene. The blackbody source is measured at a combination of temperatures and exposures times to produce curves as in Figure 4. To make the calibration applicable to a continuous range of exposure times, the NUC signals for each temperature curve are divided by the exposure times to yield a counts flux F [counts/μs]. Each line in Figure 4 becomes a point on the curve in Figure 5. The counts flux versus blackbody temperature curve of Figure 5 then serves as the calibration for the camera. The blackbody or radiometric temperature can be converted to a band-

integrated radiance by multiplying Planck's law with the spectral response of the system and integrating over the wavelength band [56].

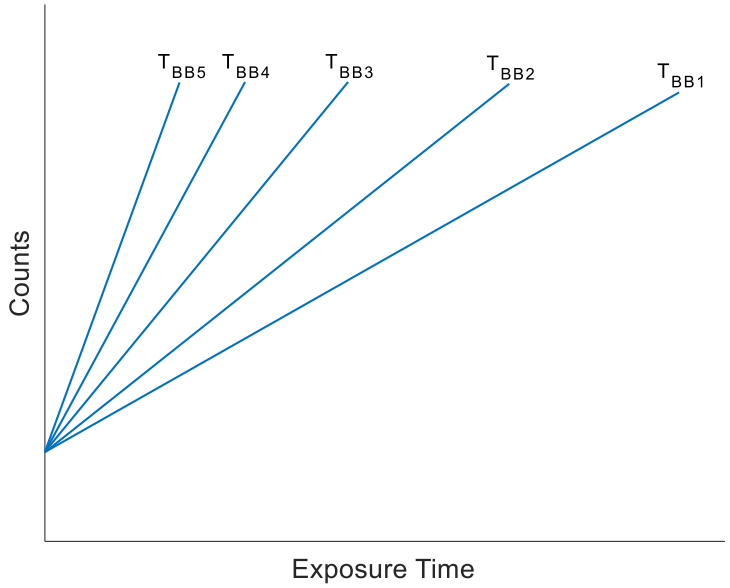

Figure 4: Example calibration curve showing counts versus exposure time at different blackbody temperatures

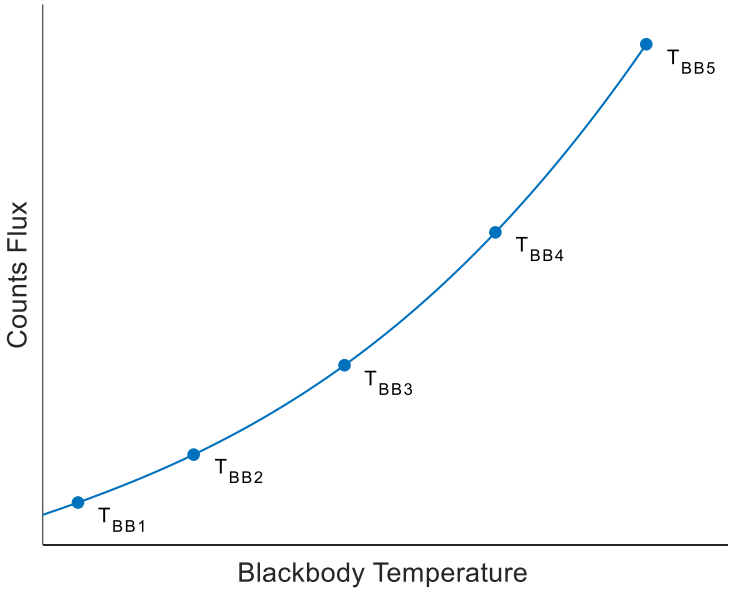

Figure 5: Example calibration curve showing counts flux versus blackbody temperature curve

Chapter 3

Single-Channel Broadband Imaging

Single-channel broadband OGI cameras such as the FLIR GF320 and OPGAL EyeCGas 2.0 have become mainstays for leak detection and repair in the oil and gas industry, and tablet-based quantification software has more recently been developed to provide instantaneous flow rate measurements of certain gases. The accuracy and capabilities of these quantification systems is an important area of interest for government and industry as emissions become more regulated and adoption of QOGI increases. This research develops similar quantification algorithms using the same single-channel broadband OGI cameras in order to fully understand the analyses being performed and possible simplifying assumptions, and to assess the performance of the commercial quantification systems. This chapter focuses on the validation of the single-channel broadband QOGI algorithms through lab-scale and field testing, and explore the performance of the commercial systems.

3.1 Lab-scale testing

To verify the QOGI measurements and algorithms developed by this research, lab-scale experimental testing was conducted so that the ambient conditions, background, gas species, flow rates and temperatures could be controlled to provide ideal conditions for the performance of QOGI and evaluate the accuracy of the estimates.

3.1.1 Controlled release apparatus

At the start of the research, a controlled release apparatus was available which consisted of: aluminum plates with passages for the flow of an ethylene glycol-water mixture; a heater-chiller pump system to control the temperature of the fluid and circulate it through the plates; a stack where the gases would

be vented from with a K-type thermocouple to measure the gas temperature; a heated hose and power supply to optionally heat the gases; and several mass flow controllers with a control box and data acquisition software. A hood vent is placed over the apparatus to evacuate the released gases outdoors. The plates were painted black to achieve a higher emissivity surface to serve as a temperature-controlled background for the gas releases. The mass flow controllers were calibrated by Trillium Measurement and Control for the gases CH_4, CO_2, and N_2 (for use with air) up to flow rates of 15 SLPM (standard litres per minute). Towards the end of the research, the apparatus was upgraded with larger aluminum plates, a more powerful heater-chiller pump, and new T-slotted framing to support the additional weight. The larger background makes visualization and measurement of the gas plume easier, especially in crosswind conditions and instances when the plume meanders to the side.

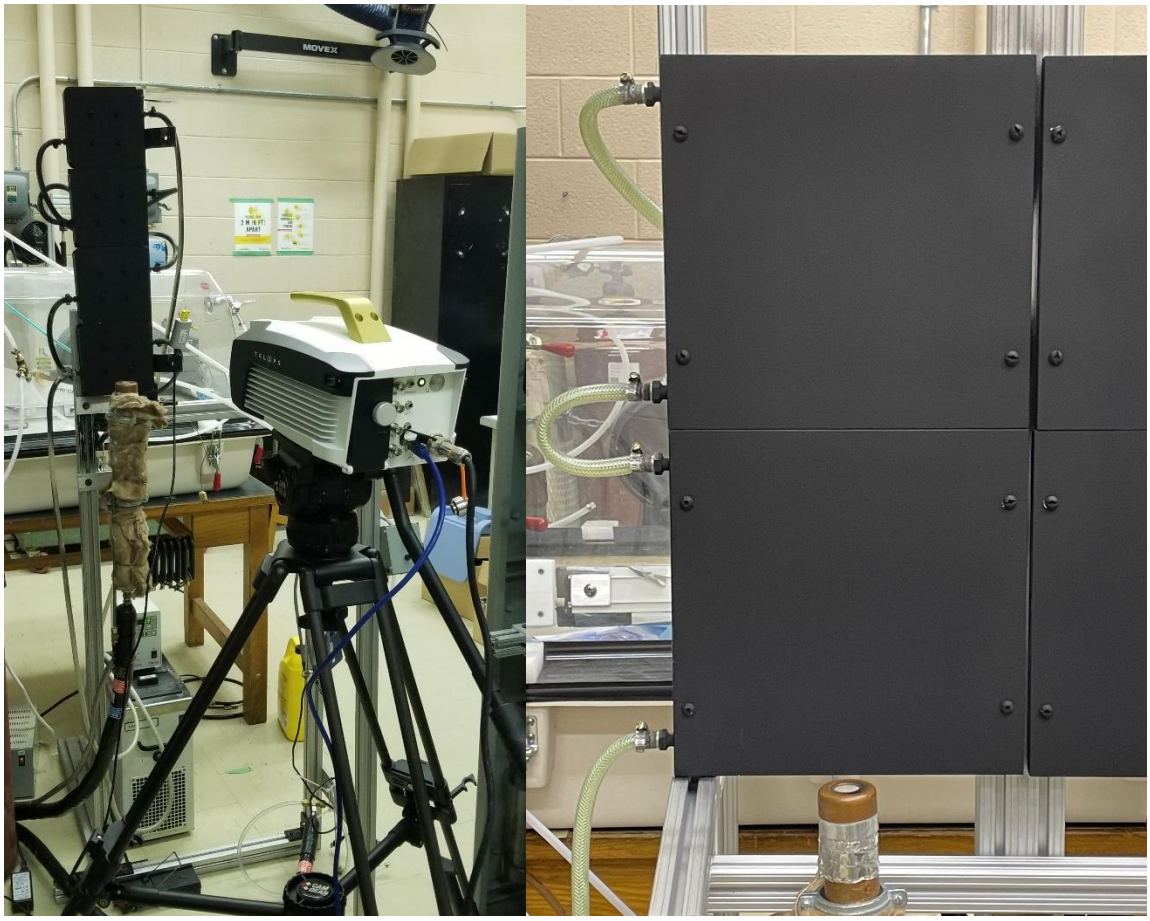

Figure 6: Experimental setups (left) original controlled release apparatus and Telops FAST M150 multispectral camera (right) new temperature-controlled background plates

3.1.2 Experimental validation using ambient temperature gas

The simplest way to validate the QOGI algorithms is using a single-channel camera to quantify a single species at a known temperature. This section will take an in-depth look into the results of a QOGI analysis.

A FLIR GF320 camera was used to image a release of ambient temperature methane (21.3°C) through the controlled release apparatus at 5 SLPM with a background temperature setpoint of 10.0°C. The actual background temperature was measured to be approximately 12.0°C using an infrared

thermometer and verified with the FLIR GF320. The actual background temperature varied across the plates and from the temperature setpoint due to heat transfer with the ambient air. Since an accurate background temperature is critical to QOGI, the temperature is taken from background pixels adjacent to the control surface to mitigate temperature variations. The measurement distance from the camera to the background plates was 1.5 m and the measurement duration was 20.8 seconds at 15 frames per second resulting in 312 frames.

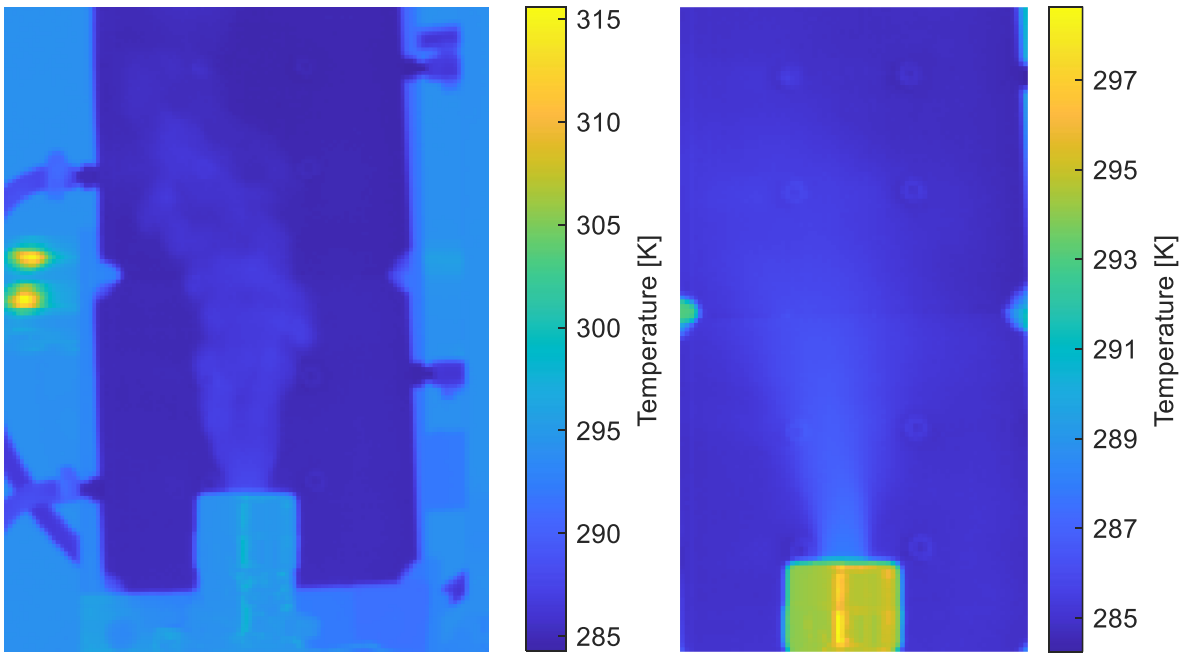

Figure 7: FLIR GF320 radiometric temperature image of ambient temperature methane through controlled release apparatus (left) instantaneous image (right) time-averaged

The radiometric temperatures are converted to an in-band radiance using Planck's law and the spectral range of the GF320 and averaged to produce a single image. Applying the QOGI algorithms to the time-averaged image as opposed to analyzing each frame individually then averaging the results yields similar column density estimates so the former approach is used to save on computational time.

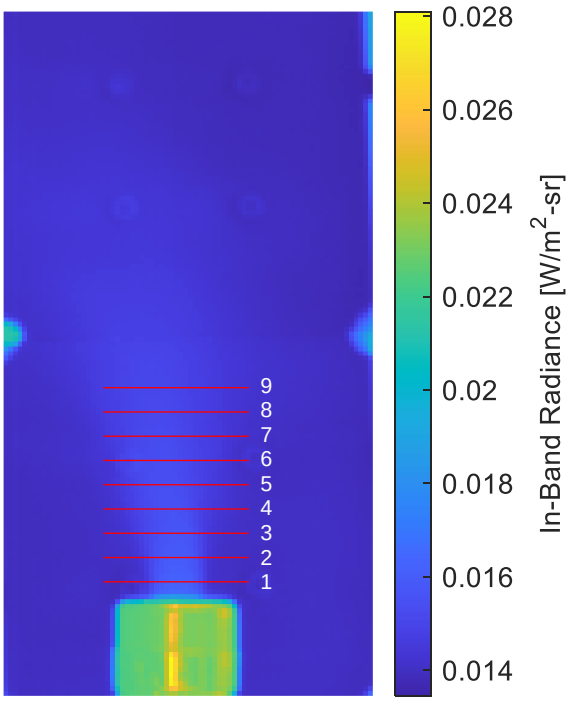

Figure 8: FLIR GF320 time-averaged in-band radiance image and several control surfaces used for analysis

Nine control surfaces are defined at height intervals of 5 pixels, or about 1 cm apart. This is to show the pixel intensities at different heights of the plume and evaluate the accuracy of the QOGI estimates at each location which is a subjective decision made during the analysis. Figure 9 and Figure 10 show how the pixel intensities and methane column densities decrease and widen due to the dispersion of the plume with increasing height.

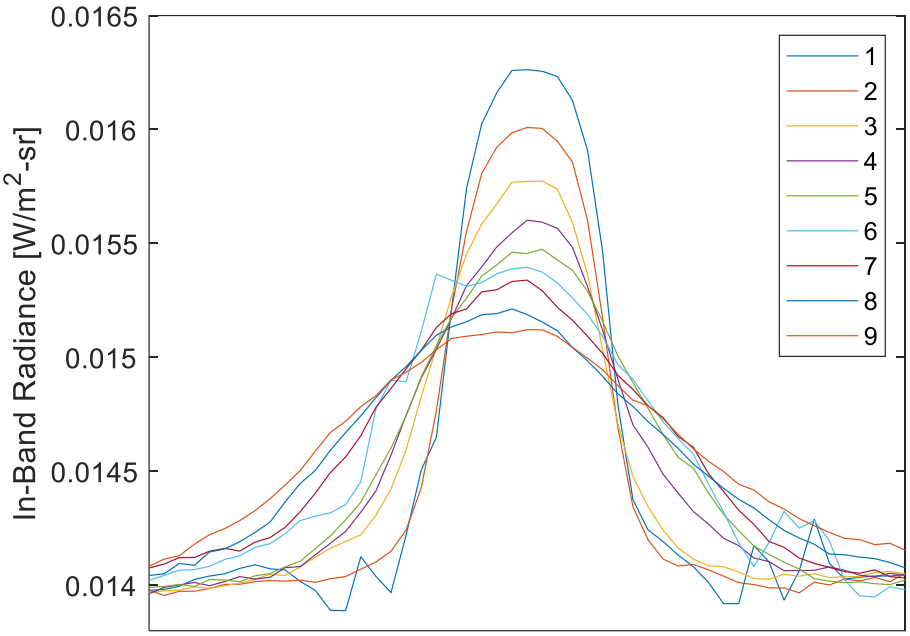

Figure 9: FLIR GF320 pixel intensities across different control surface heights

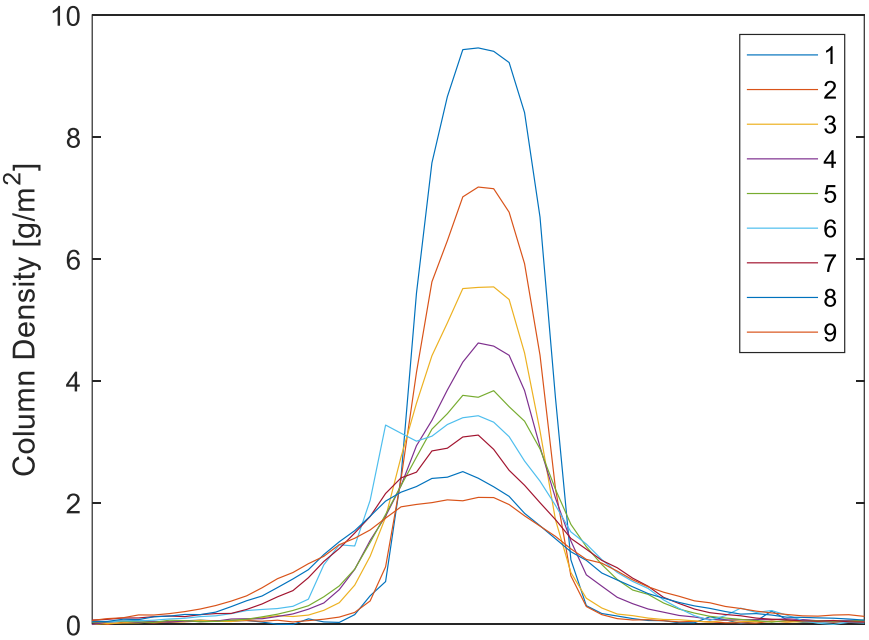

Figure 10: FLIR GF320 QOGI-inferred methane column densities at different control surface heights

A CFD-LES simulation of the controlled release apparatus at a 5 SLPM flow rate can be used to verify the QOGI-inferred column densities, although some key differences are noted. The plume in the simulation is much more stable and narrows with height whereas the plume in the experiment tends to meander and disperses horizontally. The inferred column densities are about 27% lower than the simulated column densities near the stack exit and about 75% lower further away. This does not clearly indicate that the column density estimates become less accurate at greater heights because the plume distributions between experiment and simulation are quite different further from the release point. Still, this establishes confidence in the QOGI-inferred column densities.

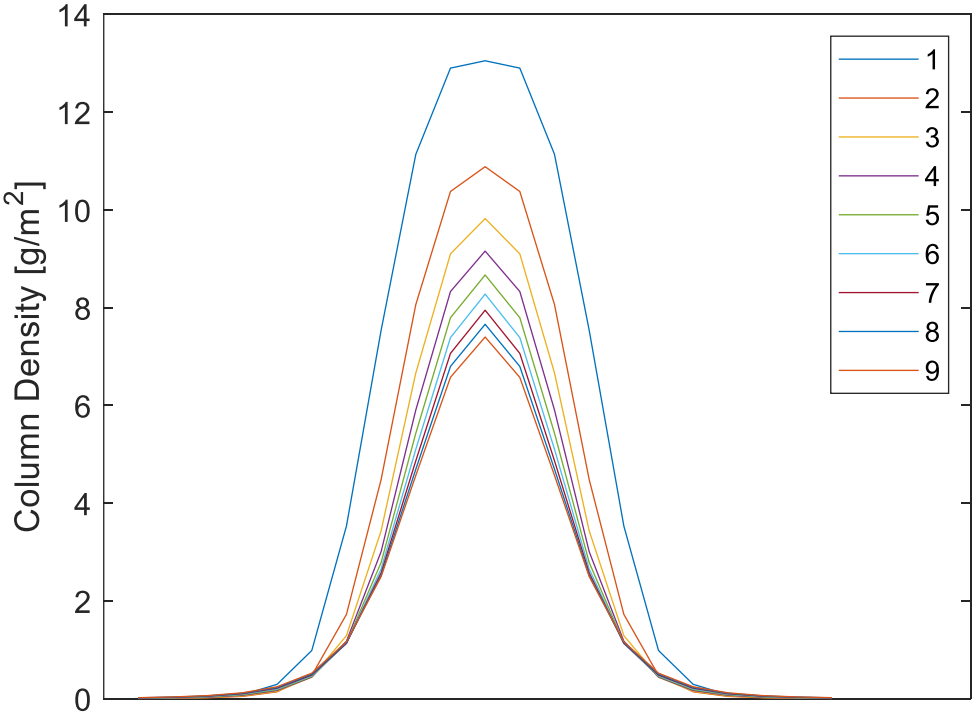

Figure 11: CFD-LES column densities of 5 SLPM release through 1.9 cm orifice at the same control surfaces as Figure 10

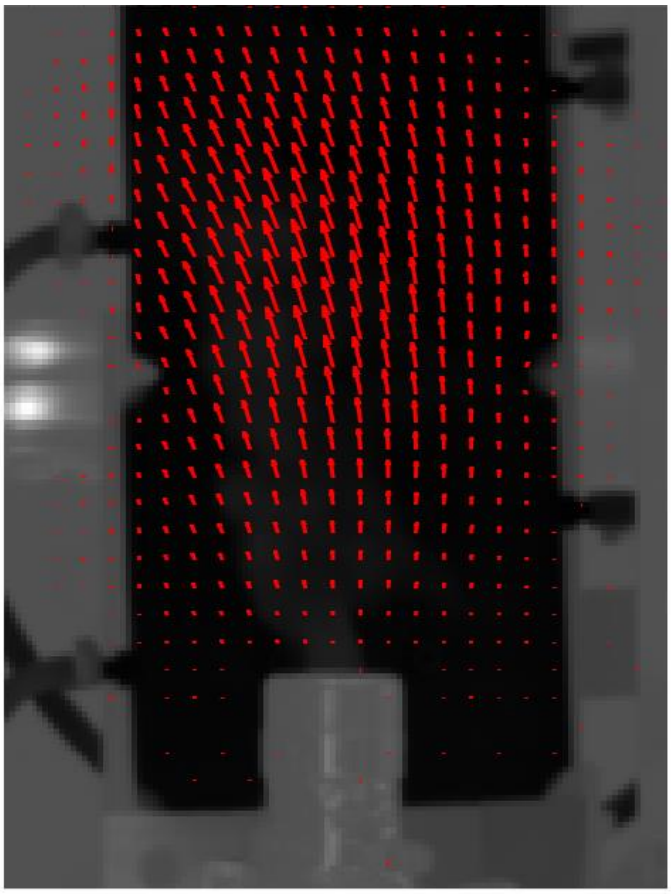

Figure 12: Time-averaged velocity field of methane through the controlled release apparatus estimated using optical flow

Figure 12 shows the time-averaged velocity field over the 312 frames, or 20.8 seconds. The Horn-Schunck optical flow is able to determine the general upwards velocity of the plume except near the stack exit where the plume appears to be stationary and lacks turbulent features or brightness gradients. The magnitude of the largest velocity is only about 0.05 m/s, which is unrealistically low considering that a 5 SLPM flow rate through a 1.9 cm diameter exit has an average velocity of 0.29 m/s. The velocity of the plume is expected to increase with height because the density of methane (0.657 kg/m^3) is lower than air (1.2 kg/m^3), so the buoyant force will accelerate the methane upwards.

Looking closer at the instantaneous velocity fields, it is observed that a large number of frames do not exhibit a clear upwards velocity for the plume. The left image of Figure 13 shows an example of a "good" optical flow result while the right image shows a "poor" result. These poor results in the instantaneous velocity fields bias the average velocity field lower, but even the "good" result has incorrect velocity magnitudes. The largest instantaneous velocities are about 0.08 m/s, which is still lower than expected based on the imposed flow rate. It is concluded that the camera frame rate of 15 Hz is too low relative to the motion of the plume. Physically this means the plume advection between frames is too large and the plume motion cannot be determined accurately. Mathematically, the brightness gradients between frames are changing significantly and the smoothness assumption is invalid.

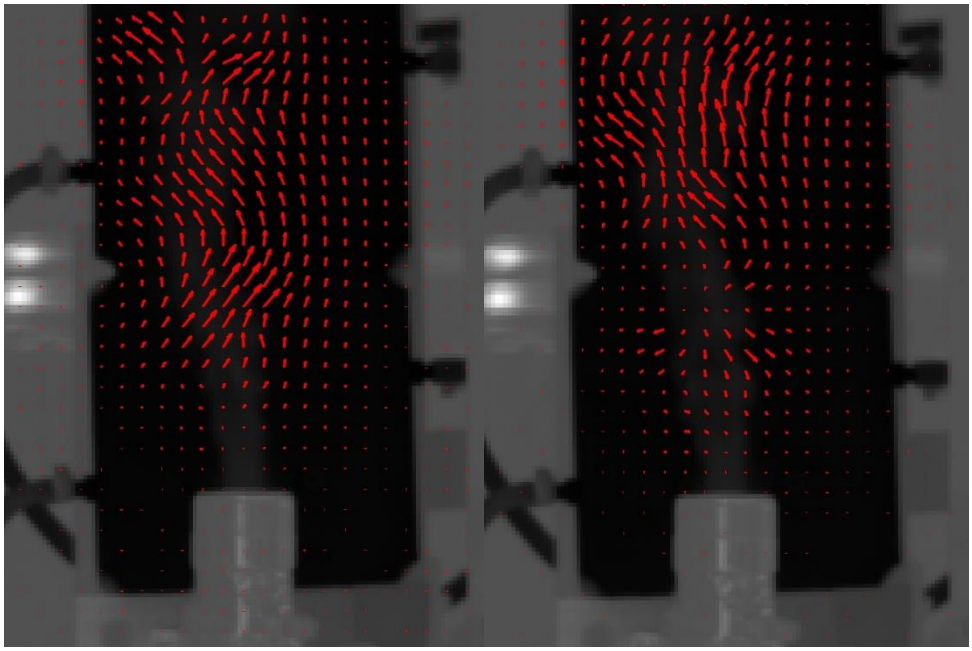

Figure 13: (left) optical flow result showing upwards velocity for a majority of the plume (right) optical flow result where the velocities are near-zero and even downwards for a majority of the plume

Using the same CFD-LES data from before, a mass-averaged velocity can be calculated by weighing the velocity of each volume element along the LOS by the density of methane within the element. This effectively marginalizes the 3D velocity field into 2D so that a comparison can be made with the intensity-weighted velocities from the infrared images. Figure 14 shows that the methane velocity is about 0.29 m/s at the exit and accelerates as it rises as expected.

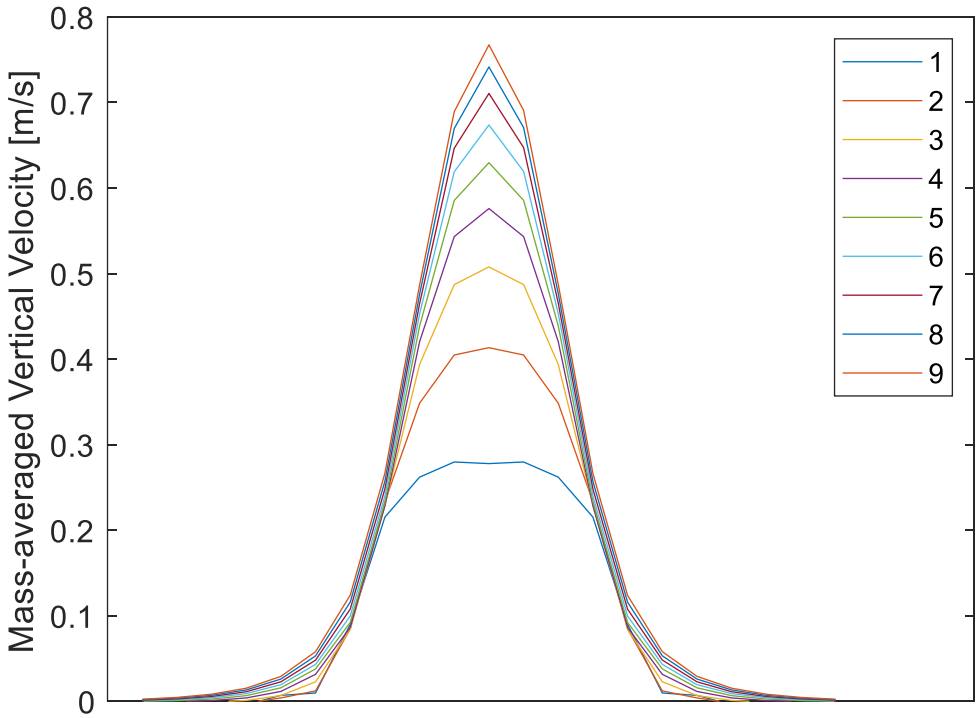

Figure 14: CFD-LES velocities of 5 SLPM release through 1.9 cm orifice at the same control surfaces as Figure 10.

Since the optical flow velocimetry results are near-zero close to the stack exit, combining them with the column densities would severely underpredict the release rate. Instead, the column densities can be combined with the average velocity based on the flow rate and exit diameter. This is not a true "blind" estimate since the flow rate is known from the mass flow controller. This average velocity

assumption also becomes less accurate further from the stack exit; however, it is still useful in evaluating the accuracy of a QOGI estimate. The actual release rate for these tests was 5 SLPM.

Table 1: Summary of QOGI estimates using FLIR GF320 and in-house algorithms on controlled release apparatus at 5 SLPM

Control surface no.	Height above exit [cm]	Estimated release rate [SLPM]	% Error
1	0.96	3.96	-20.8%
2	1.92	2.84	-43.2%
3	2.88	2.56	-48.8%
4	3.85	2.34	-53.2%
5	4.81	2.25	-55.0%
6	5.77	2.44	-51.2%
7	6.73	2.20	-56.0%
8	7.69	2.03	-59.4%
9	8.65	2.01	-59.8%

Assuming an average velocity of 0.29 m/s, the most accurate QOGI estimate was nearest the stack exit at 3.96 SLPM, which is an error of -20.8% versus the ground truth. The assumed velocity is expected to be reasonably accurate close to the stack exit so this error largely constitutes the error in the inferred column densities. Further from the stack exit, the errors increase rapidly up to about -60%. It is difficult to decouple the error associated with the column densities from the velocities at these greater heights because the optical flow velocimetry was largely unsuccessful and the plume dispersion in the experiment was much wider than simulation. Still, this analysis demonstrates the capability of single-channel QOGI in inferring the column densities of ambient temperature methane and the challenges of optical flow velocimetry.

3.1.3 Comparison to FLIR QL320 quantification system

The previous analysis can be expanded to more test conditions by varying the release rate and background temperature. A larger release rate of 10 SLPM was used as well as background temperatures that were above and below the ambient temperature to test the capability of both absorption and emission spectroscopy. Several background temperatures were used to see whether increasing temperature difference between the gas and the background could improve QOGI accuracy. The results from the UW QOGI algorithms are also compared to the FLIR QL320 quantification system which is a commercial tablet-based system that works alongside the GF320 to provide instantaneous emission rate estimates.

The exact methods and models used within the QL320 system are proprietary and owned by Providence Photonics and FLIR, but a basic understanding can be derived from their literature and patents [33][34]. The system seems to use a simplified version of the RTE discussed in Section 2.2 that assumes a uniform path concentration along the plume length. The system identifies gas-containing pixels and background pixels, subtracts the background intensity from the gas-containing pixel intensity to obtain the emission or absorption of the gas, and uses a lookup table of known path concentrations at a given temperature to estimate the path concentration. Then the system uses the optical magnification, pixel size, and distance to calculate the plume length perpendicular to the frame and an undescribed algorithm to determine the LOS length of the plume. Finally, a cross-correlation algorithm is used to track the displacement of clusters of gas pixels between frames and combines that with the camera frame rate to yield the velocity of the plume. The concentrations, plume dimensions, and velocity are combined to produce a flow rate estimate. Providence Photonics and ExxonMobil controlled lab testing show that the estimated flow rates are within -17% to +43% of the actual flow

rates which ranged from 0.13 to 0.49 SLPM of propane [34]. The average error when quantifying methane was +24% with a standard deviation of 39% for flow rates of 1.38 to 2.75 SLPM [34].

The QOGI algorithms developed by this research will be referred to as the "UW QOGI" results while the estimates provided by the FLIR QL320 quantification system will be referred to as the "QL320" results with appropriate distinctions. All results are 20-second time averages and use a control surface placed about 1 cm above the stack exit. Different control surface heights were trialed with the QL320, and this height provided the most accurate results. The UW QOGI results assume an average velocity based on the flow rate and exit diameter due to the frame rate limitation of the GF320 which makes optical flow velocimetry inaccurate. The QL320 requires a user-specified wind speed setting that includes Calm (0-2 mph), Normal (2-10 mph), and High (10+ mph) options corresponding to 0-0.9 m/s, 0.9-4.5 m/s, and 4.5+ m/s respectively. The expected gas velocities at 5 and 10 SLPM are below 0.9 m/s but both the Calm and Normal wind speed settings were trialed. While the physical meaning of this setting is unclear and not specified in the product literature, it is hypothesized that these settings modify some parameters in the cross-correlation velocimetry algorithm.

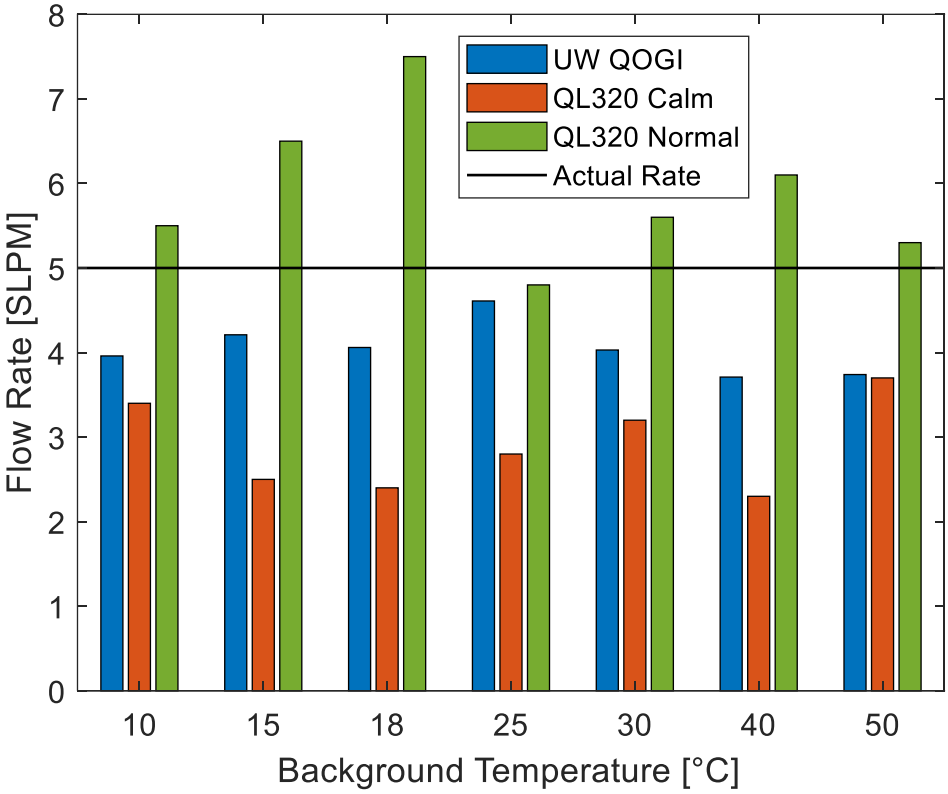

Figure 15: UW QOGI versus QL320 estimates both using GF320 at 5 SLPM ambient temperature methane

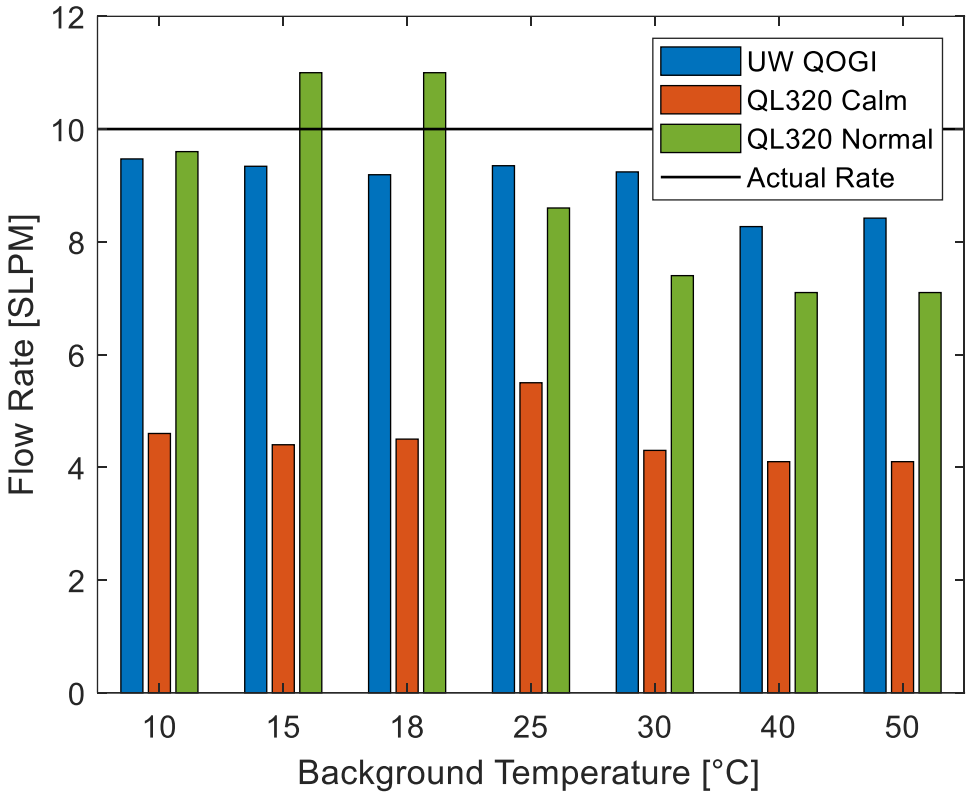

Figure 16: UW QOGI versus QL320 estimates both using GF320 at 10 SLPM ambient temperature methane

At a flow rate of 5 SLPM, the average error of the UW QOGI estimates was -19% while the QL320 had an average error of -42% and +18% at Calm and Normal wind speed settings, respectively. At a flow rate of 10 SLPM, the average error of the UW QOGI estimates was -10% while the QL320 had an average error of -55% and -8% at Calm and Normal wind speed settings, respectively. The QL320 with the Calm wind speed setting significantly underpredicted the actual flow rate despite the expected gas velocities being within the setting's range. The QL320 with the Normal wind speed setting overpredicted the actual flow rate at 5 SLPM and straddled the actual flow rate at 10 SLPM. The UW QOGI consistently underpredicted the actual flow rate with very little variation, which indicates consistency in the column density estimates because the velocities are not being inferred. This leads to

the belief that the variation in the QL320 estimates is mostly due to inconsistency in the cross-correlation velocimetry, but there is still an advantage to this system in this respect because the optical flow velocimetry was entirely inaccurate at a frame rate of 15 Hz. It was also noted that the optical flow velocimetry did not perform any better at greater background temperature differences, even though this would increase the gas-background contrast and possibly improve the brightness gradient weights of the optical flow algorithms.

From this comparison, it is concluded that both the UW QOGI algorithms and QL320 system are capable of quantifying methane column densities with at least 20% accuracy in controlled conditions. The 15 Hz frame rate of the GF320 is a limitation when it comes to optical flow velocimetry, but the cross-correlation velocimetry algorithm of the QL320 seems to be well-suited and well-tuned for the application when using the appropriate wind speed setting. The ambiguity of the wind speed setting may pose a problem for operators in the field and lead to inaccurate estimates if the incorrect setting is used. Lastly, there was no clear trend observed by changing the background temperature difference. As long as there was sufficient temperature difference between the gas and background, emissive and absorptive plumes could be quantified with approximately equal accuracy. The detection limits of methane with the GF320 depending on temperature, flow rate, and distance are known [48][49][50] and the quantification accuracy near these limits was not the focus of this experiment.

3.1.4 Effect of uncertain gas temperature

Another research question was the effect of uncertain gas temperature on quantification accuracy. The QL320 assumes the gas is at ambient temperature [57], because with a single-channel measurement, only one quantity-of-interest can be inferred without making the problem even more ill-posed. The intensity measured by the camera depends on the gas temperature as seen in Equation (5), so using an

accurate gas temperature in QOGI is critical. The controlled release apparatus can be used with a heated hose to increase the temperature of the gas above ambient temperature. This was done to examine the sensitivity of the QL320 estimates to uncertain gas temperature because operators in the field may assume the gas is at ambient temperature and unknowingly produce inaccurate estimates because the quantification system does not simultaneously infer the gas temperature.

Methane was heated to 55°C at the stack exit with a background temperature of 13°C. Both 5 SLPM and 10 SLPM flow rates were tested using Calm and Normal wind speed settings in the QL320 and the ambient temperature was set to: (1) the actual room ambient temperature of 22°C, and (2) the highest ambient temperature possible in the interface of 49.5°C. The UW QOGI algorithms are included for reference using average velocity assumptions based on the flow rate and exit diameter, and the temperature of the gas in the algorithms is set to 55°C. The control surfaces are located 1 cm above the stack exit. At this position, the gas is expected to have decreased in temperature from the initial 55°C inside the stack but has not reached ambient temperature. The two temperatures selected in the QL320 interface should realistically represent upper and lower limits on the actual gas temperature at the control surface.

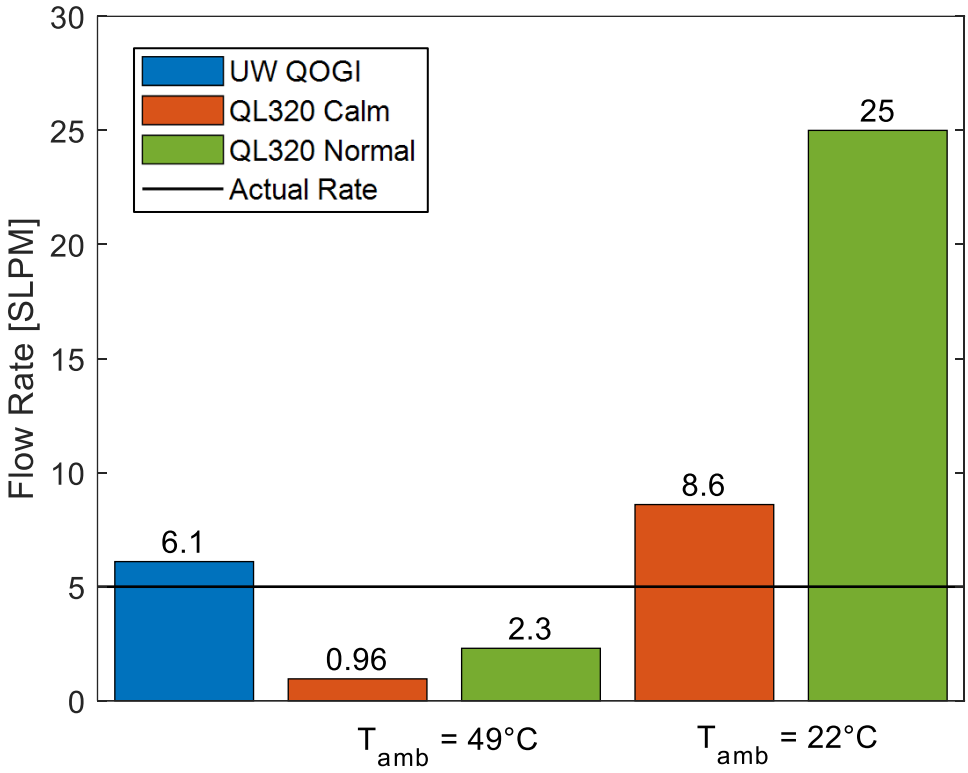

Figure 17: UW QOGI versus QL320 estimates both using GF320 at 5 SLPM heated methane

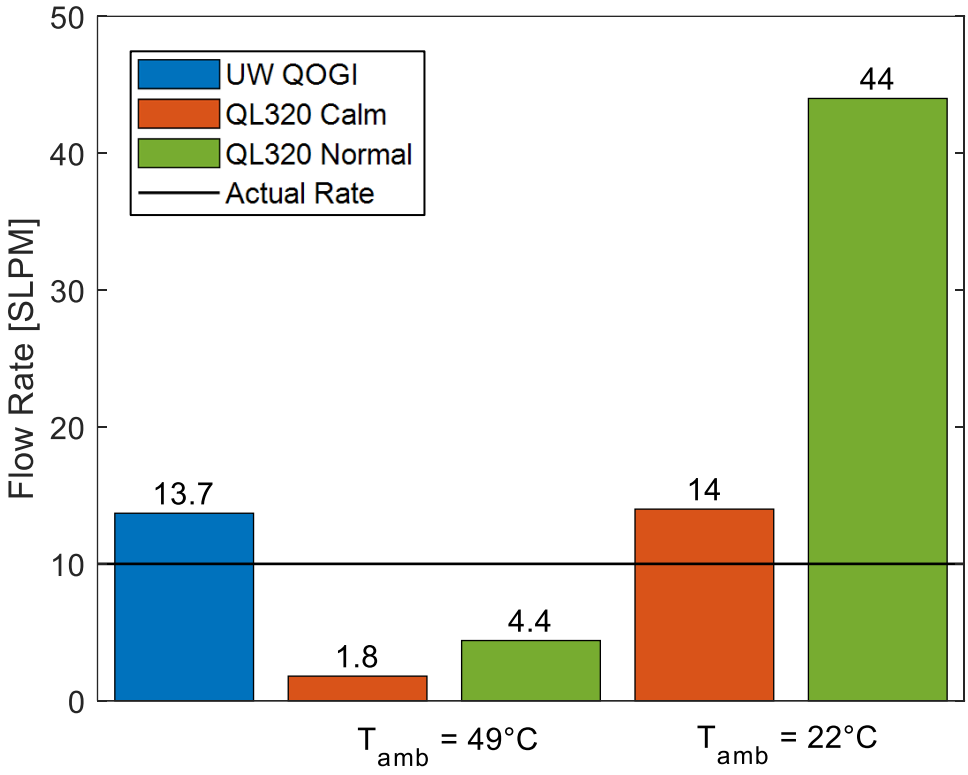

Figure 18: UW QOGI versus QL320 estimates both using GF320 at 10 SLPM heated methane

Figure 17 and Figure 18 reveal the importance of an accurate gas temperature. The UW QOGI estimate using a gas temperature of 55°C measured at the stack exit overpredicts the actual flow rate by 21 to 37%. The QL320 estimates using ambient temperatures of 49.5°C to 22°C and Calm and Normal wind speed settings can underpredict the actual flow by 80% or overpredict by 400% depending on the combination of input parameters. Using a gas temperature of 55°C or 49.5°C means the blackbody intensity of the gas is higher which means a lower path concentration is required to achieve the measured pixel intensity, so when the actual gas temperature is lower the inferred column density is lower than it should be, and the flow rate is underpredicted. This inverse relationship between

temperature and concentration on pixel intensity holds true when the actual temperature is higher than the specified gas temperature, leading to the flow rate to be overpredicted.

Uncertainty in gas temperature can be a very relevant problem in field measurements when there are hot gases being emitted or compressed gases which experience Joule-Thomson cooling upon expansion [58]. The assumption that the gas is at ambient temperature will always become true as the gas moves downstream and equilibrates with the ambient air, however the gas will also be diffusing which decreases the path concentration and depending on the flow rate, wind speed, measurement distance, and background temperature difference, quantification can be more difficult downstream.

3.2 Field testing

Field trials were organized by the University of Waterloo, Arolytics Inc., and Carbon Management Canada (CMC), and funded by the Petroleum Technology Alliance Canada (PTAC) and Clean Resources Innovation Network (CRIN) in Brooks, Alberta for April 20th to 24th 2022. The objective of this project was to survey and assess the performance of methane quantification technologies under industrially relevant conditions, with a focus on estimating quantification uncertainty. This research contributed to the study of QOGI technology in the project by performing measurements with the FLIR GF320 single-channel camera and QL320 quantification system, and separately analyzing the radiometric data using the spectroscopic and velocimetry models developed by this research. The Telops FAST M150 multispectral camera was also tested, and those results will be discussed in Section 4.2. The project's objective of quantifying uncertainty, particularly for QOGI, is important considering the motivation of this research, but beyond the scope of this thesis and the individual contributions made.

3.2.1 Test equipment and setup

The controlled releases were made from a 1.42 m tall stack that could be extended to 3.18 m and a 6 cm diameter outlet. Several sensors were placed on site to monitor the temperature and wind speed every minute. The ambient temperatures ranged from 10.9°C to 16.2°C and the wind from 0.6 m/s to 7.6 m/s during the measurements. The methane was passed through a heat exchanger exposed to ambient air before being released.

The measurements were made with a sky background which ranged from clear to partially cloudy. Partial cloud coverage poses a challenge to QOGI in two ways: a non-uniform background intensity affects the spectroscopic model, and background motion affects the optical flow velocimetry. For these reasons, only measurements with clear sky background across the control surface were analyzed. QOGI in overcast conditions is still feasible because the clouds are relatively uniform and stationary, however, there must be sufficient ΔT between the clouds and gas for visualization and quantification. Overcast conditions were not present during the field trials and could not be tested.

Scenes were recorded for at least 1 min duration, which results in 900+ frames at 15 Hz. Measurements were taken as close as possible to the release point while maintaining a LOS perpendicular to the wind and clear background.

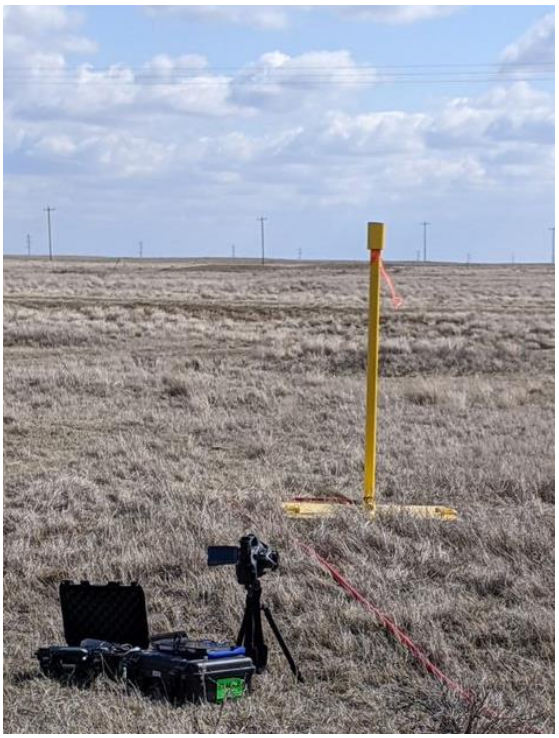

Figure 19: Alberta field measurements 1.42 m tall stack release setup

3.2.2 Low flow rate measurements

The initial test plan for the field trial focused on a third-party QOGI service provider using the FLIR GF320 and QL320. A wide range of flow rates were investigated, ranging from 0.25 to 30 kg/hr (5.9 to 706 SLPM). Another GF320 and QL320 became available in the second half of the field trials, which was operated by UW personnel. The result was that the lowest flow rate measurement made independently was at 5 kg/hr (118 SLPM) using the 1.42 m tall stack. Figure 20 shows the image and visualization overlays from the QL320 quantification system directly. The QL320 is able to mask pixels in red where there is insufficient ΔT with the gas as well as highlight pixels where gas is detected. The blue arc indicates the control surface for the QL320 quantification. This image shows that the QL320

is able to detect methane with a clear sky background. The QL320 estimate was 60 SLPM for this measurement which is an error of -49%.

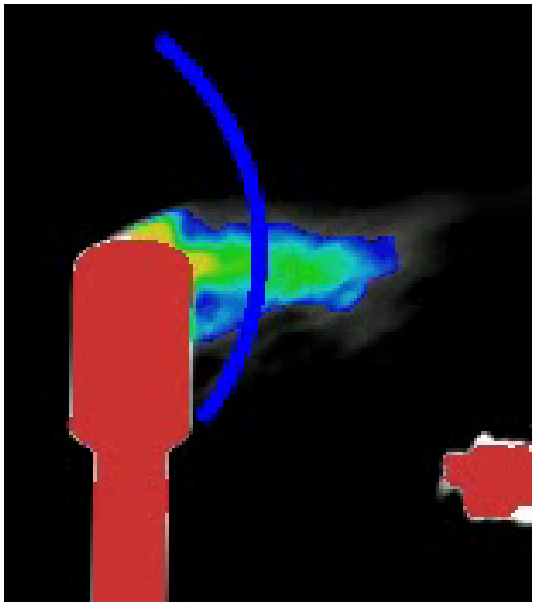

Figure 20: QL320 visualization of 5 kg/hr, 1.42 m stack release from Alberta field measurements

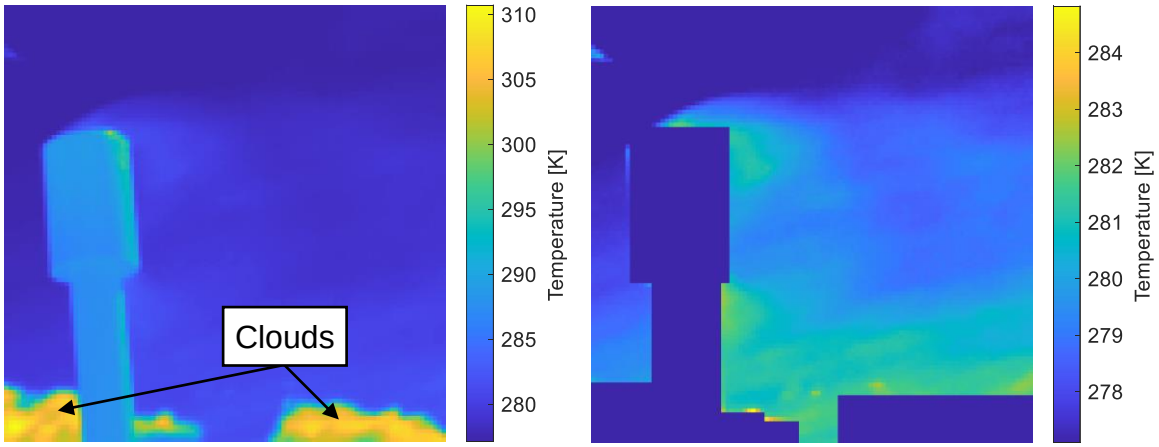

Figure 21: GF320 images of 5 kg/hr, 1.42 m stack release from Alberta field measurements (left) no mask (right) with mask

Figure 21 shows the GF320 images in terms of radiometric temperature. This shows that the clouds are reflecting the sun and have the highest radiometric temperature in the scene at over 300 K or 27°C. With the gas temperature being about 11.8°C at the time, there should be sufficient ΔT with the clouds to quantify the plume which leads to conclusion that the QL320 is masking pixels above or below a temperature threshold based on the ambient temperature and whether the user specifies an emissive or absorptive plume. Manually masking the clouds and stack in the image highlights the plume. At this relatively low flow rate and high wind speed, it is evident that there is significant downwash of the plume into the low-pressure wake created by the stack. This downwash is not captured by the QL320 visualization, and this likely contributes to the -49% error in its estimate. QOGI of the downwash is especially difficult because the distribution is no longer Gaussian along the control surface, and in the case of the measurement presented, the downwash appears to coincide with the clouds. Nonetheless, the in-house spectroscopic model can be applied to the radiometric data from the GF320 while the wind speed can be used in-lieu of the velocimetry model which has been demonstrated to be inaccurate with the 15 Hz frame rate.

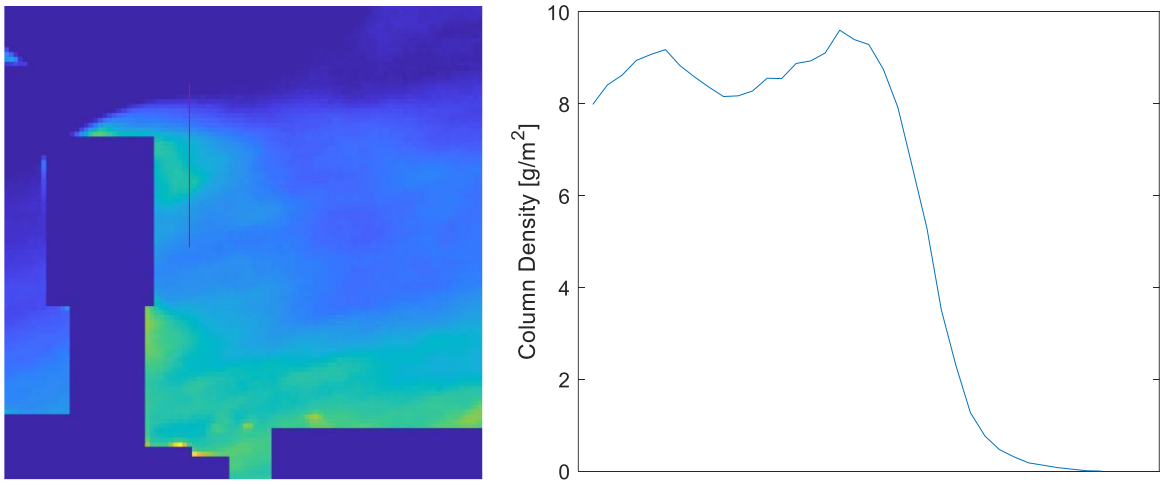

Figure 22: In-house QOGI of 5 kg/hr, 1.42 m stack release from Alberta field measurements using GF320 (left) control surface (right) inferred column densities

The control surface used is similar to the one used with the QL320. The wind speed is taken as 6.6 m/s based on the 1 minute average from the anemometer deemed most accurate. The estimated flow rate based on the inferred column densities and wind speed is 25 kg/hr or 589 SLPM, which is an error of +400%. The first explanation for this large error is that the velocity of the methane likely has not reached the wind speed at the chosen control surface which is quite close to the stack. Another explanation is that the wind speed is measured by an anemometer at a different height and location from the stack exit which means it may not be representative of the gas velocity. The column densities are plausible but difficult to ascertain without an accurate simulation of the stack and wind conditions. Also, the amount of downwash near the bottom of the frame is suspiciously high and may be sun reflection of thinner cloud coverage. All things considered, the low flow rate and high wind speed leading to downwash and low frame rate of the GF320 make QOGI very challenging in this scenario. Additional measurements with completely clear skies and lower wind speeds would be beneficial to better understand the extent of the downwash. A higher frame rate would also enable optical flow velocimetry to obtain instantaneous pixel velocities so that a definite conclusion on the accuracy of the QOGI estimates can be made.

3.2.3 High flow rate measurements

Higher flow rate measurements ranged from 20 to 50 kg/hr (471 to 1177 SLPM) and used a 3.18 m tall stack. The wind speed varied from 4.5 to 6.6 m/s during the measurements. Figure 23 shows the GF320 images of a 20 kg/hr release through the 3.18 m stack using both horizontal and vertical lines-of-sight. The idea to use a vertical LOS through the plume came later in the field trials and has the benefits of 1) having the shortest possible LOS and 2) capturing any downwash gas in the LOS. However, the vertical LOS may deviate from the Gaussian plume profile assumption close to the stack due to the

downwash effect. As seen in the horizontal LOS image, the downwash of the plume has reduced due to the higher flow rate which gives the gas more vertical momentum as it exits the stack.

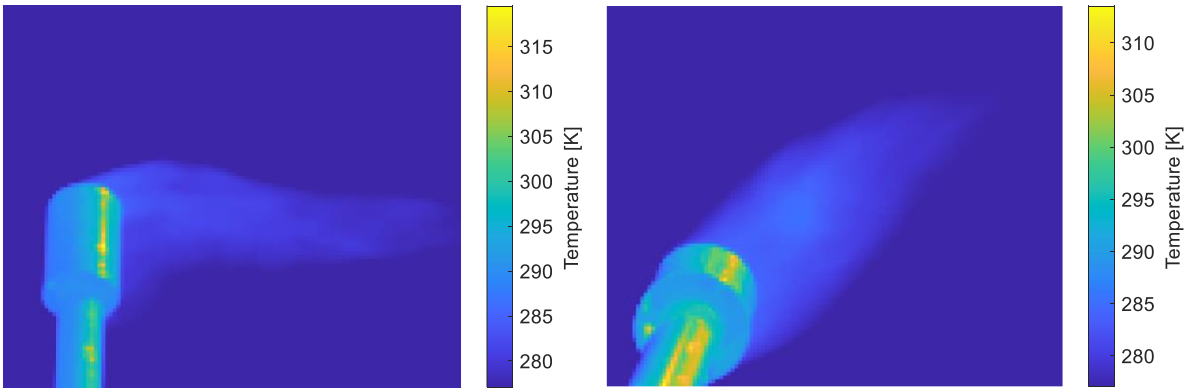

Figure 23: GF320 images of 20 kg/hr, 3.18 m stack release from Alberta field measurements (left) horizontal LOS (right) vertical LOS

Table 2: Summary of QL320 and in-house QOGI estimates for 3.18 m tall stack release from Alberta field measurements

Actual Release Rate [kg/hr (SLPM)]	QL320 Estimate [kg/hr (SLPM)]	% Error	QOGI Estimate [kg/hr (SLPM)]	% Error
20 (471)	10.2 (240)	-49%	14.6 (344)	-27%
20 (471)	11.5 (270)	-43%	15.6 (367)	-22%
30 (706)	16.6 (390)	-45%	22.0 (518)	-27%
40 (942)	23.4 (550)	-42%	25.9 (610)	-35%
40 (942)	29.7 (700)	-26%	29.5 (694)	-26%
50 (1177)	23.4 (550)	-53%	22.0 (518)	-56%
50 (1177)	22.9 (540)	-54%	23.0 (541)	-54%
	Average	-46%	Average	-35%

Table 2 shows a summary of the QL320 estimates and QOGI estimates using the algorithms developed in this research. Both approaches consistently underpredict the actual release rate with an average error of -46% for the QL320 and -35% for the in-house spectroscopic model combined with wind speeds.

The accuracy of the spectroscopic model can be examined by comparing the inferred column densities to those calculated from a Gaussian dispersion model [59]. The Gaussian dispersion model relates the local concentration of a gas as a function of the source strength (flow rate), wind speed, and dispersion coefficients. For brevity, only the 20 kg/hr flow rate will be presented with a wind speed of 6 m/s. The dispersion coefficients in the Gaussian dispersion model are manually fitted such that the width of the modeled and measured plumes are roughly equal (12 cm wide at 6 cm downwind).

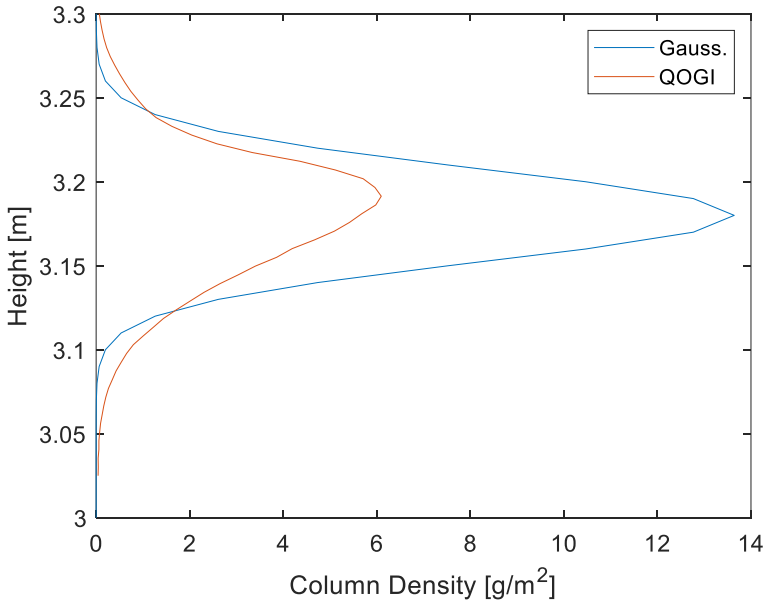

Figure 24: Comparison of inferred column densities to Gaussian dispersion model

The expected column densities based on the Gaussian dispersion model show that the inferred column densities are 44% lower when integrated across the control surface. Given that the wind speed-

derived flow rate estimate was 27% lower than the actual release rate for this particular measurement, it seems that the inferred column densities are underestimated by the spectroscopic model, while the wind speed is overestimating the gas velocity across the control surface. It's not possible to decouple these error sources for the QL320 estimate.

3.3 Chapter summary

This chapter focused on QOGI using single-channel broadband MWIR imaging. The in-house QOGI algorithms developed by this research were validated experimentally using a FLIR GF320 and a controlled release apparatus that vented methane at ambient temperature and controlled indoor conditions. The column densities obtained using the spectroscopic model were deemed to be reasonably accurate, but the optical flow velocimetry was unsuccessful due to the 15 Hz frame rate of the GF320. An average velocity based on the flow rate and exit diameter was used and the QOGI estimate underpredicted the actual flow rate by 21% at best. The in-house QOGI algorithms were benchmarked against the FLIR QL320 quantification system at 5 SLPM and 10 SLPM over a range of background temperatures. The average error of the in-house QOGI estimates were -19% and -10% at 5 SLPM and 10 SLPM, respectively, while the QL320 had an average error of -42% and -55% using the Calm wind speed setting. and +18% and -8% using the Normal wind speed setting. The error in the in-house QOGI estimates is believed to be mostly due to the inferred column densities. The column density and velocimetry errors in the QL320 estimates cannot be decoupled, but the variation in the estimates is attributed to inconsistency in the cross-correlation velocimetry algorithm. The last of the lab-scale testing was using heated methane to examine the effect of uncertain gas temperature on QOGI estimates. Using a gas exit temperature of 55°C as measured by a thermocouple placed in the stack exit, the in-house QOGI estimates now overpredicted the actual flow rate by 21% and 37% at 5 SLPM and

10 SLPM, respectively. The QL320 was tested using the maximum 49.5°C user-specified temperature and actual 22°C ambient temperature, and the results were between 5-times higher and 5-times lower than the actual flow rate depending on the choice of wind speed setting and temperature. This effectively demonstrated the importance of gas temperature to the accuracy of QOGI estimates and the limitation of single-channel QOGI in these scenarios which may be solved by multispectral QOGI.

Field testing using the single-channel GF320 camera and QL320 quantification system demonstrated some of the challenges that arise in certain conditions. Partial cloudiness poses a challenge to QOGI since the non-uniform background intensity interferes with the spectroscopic model and cloud motion interferes with the velocimetry model. High wind speeds with low flow rates leads to rapid plume dispersion and thinning which makes quantification difficult. At the single low flow rate that was tested, the QL320 estimate had an error of -49%. Optical flow velocimetry could not be performed once again due to the 15 Hz frame rate of the GF320, but using the wind speed in-lieu of inferred velocities resulted in a QOGI estimate that was 5-times greater than the actual release rate. Large errors are likely present in both the spectroscopic model and wind speed approximation in this scenario. At higher flow rates, the QL320 had an average error of -46% and the in-house QOGI using wind speed data had an average error of -35%. Based on a Gaussian dispersion model, the column densities are likely underpredicted while the wind speed is likely higher than the local gas velocity.

Chapter 4

Multispectral Imaging

Multispectral spectral imaging introduces additional spectral information about the scene, which allows more parameters to be inferred simultaneously, such as the gas temperature, LOS plume thickness, and concentrations of multiple gas species. This chapter will explore the lab-scale and field testing of the Telops FAST M150 camera and challenges encountered, as well as simulation of a hypothetical cooled-filter multispectral camera to demonstrate the advantages over warm filters.

4.1 Lab-scale testing

4.1.1 Filters transmittance measurement

The FAST M150 has interchangeable filters and lenses which allows them to be removed and measured. Measuring the transmittances of the optical elements improves the accuracy of the QOGI spectroscopic model in comparison to Heaviside function approximations using the manufacturer specifications. Filter and lens transmittances were measured using a Bruker Invenio Fourier-transform infrared spectrometer (FTIR). The filter transmittances were measured in both directions to ensure the installation orientation was not critical. Note that position 1 in the filter wheel does not contain a filter. Also, the sharp drop in lens transmittance at 1852 cm^{-1} (5.4 μm) corresponds to one limit of the FPA spectral range so to simulate the sensitive range of the FPA the transmittance is manually set to zero below 1852 cm^{-1}. The other limit of the FPA is 6667 cm^{-1} (1.5 μm) but the FTIR measurement was setup only to measure until 4000 cm^{-1} because the spectral range of the lens was stated to be 2000 cm^{-1} to 3333 cm^{-1} (3.0 to 5.0 μm) by the manufacturer. It was later found that the lens had a non-zero transmittance above 3333 cm^{-1} which means the FPA would receive light above this range and the lens

transmittance should be remeasured. However, the FTIR measurement was not redone after all because the QOGI and warm filter correction was found to be unfeasible.

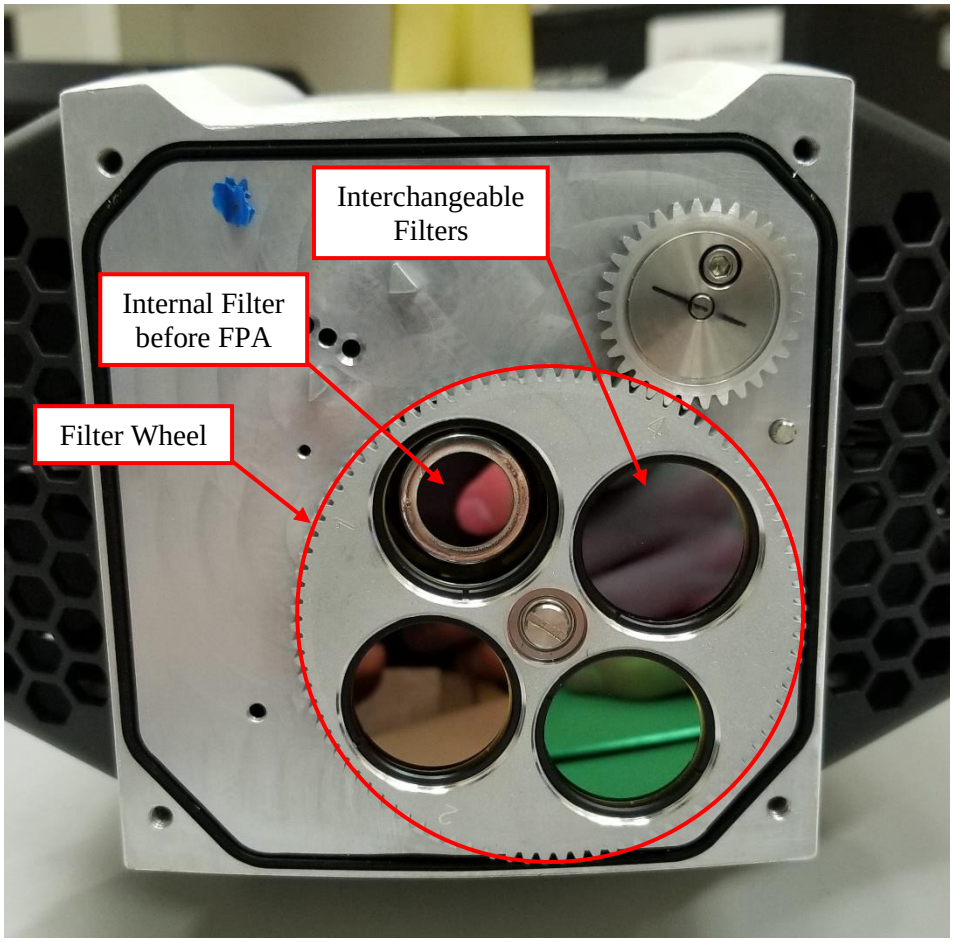

Figure 25: FAST M150 exposed filter wheel

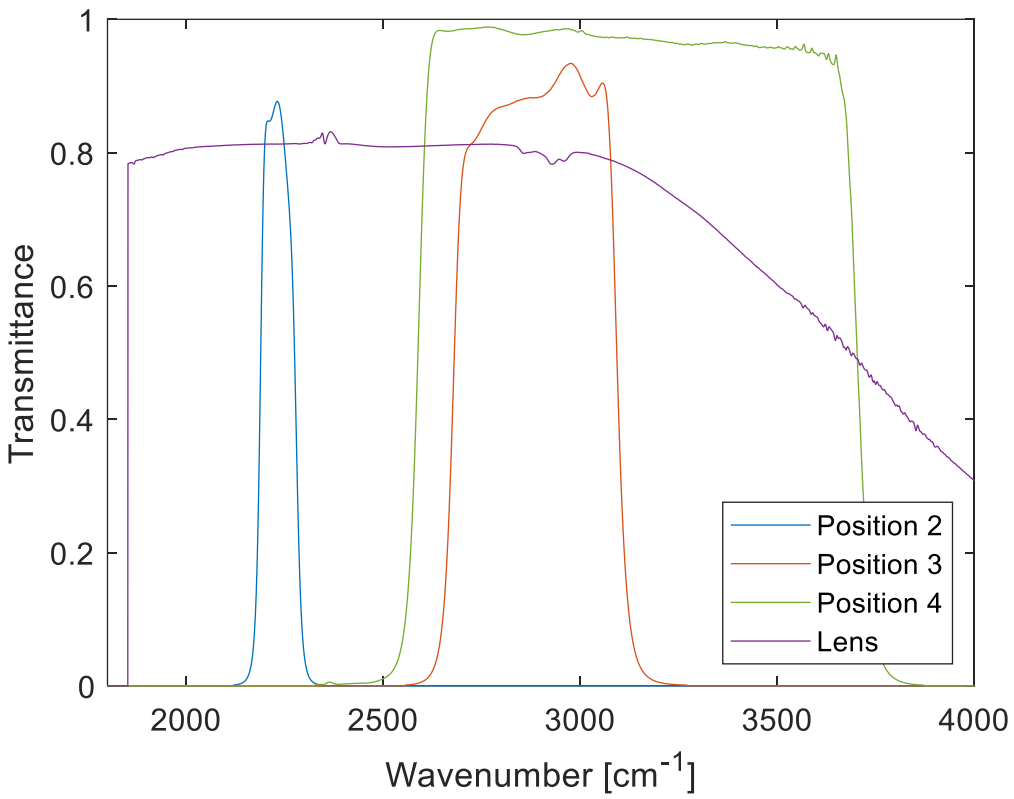

Figure 26: FAST M150 filter and lens transmittance measurements made with the FTIR. Position 1 contains no filter.

Figure 27 shows the filter transmittances alongside the spectral absorption coefficients of CH_4, CO_2, and H_2O at 20°C, 100% volume fraction, and 1 bar. This shows that position 2 is capable of isolating CO_2, position 3 is capable of isolating CH_4, and position 4 captures CH_4 and H_2O. The filter transmittances in this figure have been multiplied by the lens transmittance in this plot to represent the total transmittance of the optical elements. It is observed that the transmittance of the filter in position 2 barely captures the spectral lines of CO_2, which could pose a challenge for accurate quantification of this gas since the intensity measured by this channel will not be sensitive to changes in the intensity of CO_2 emission and absorption. It is also observed that positions 1 and 4 will capture ambient water vapour which must be considered when the LOS is very long.

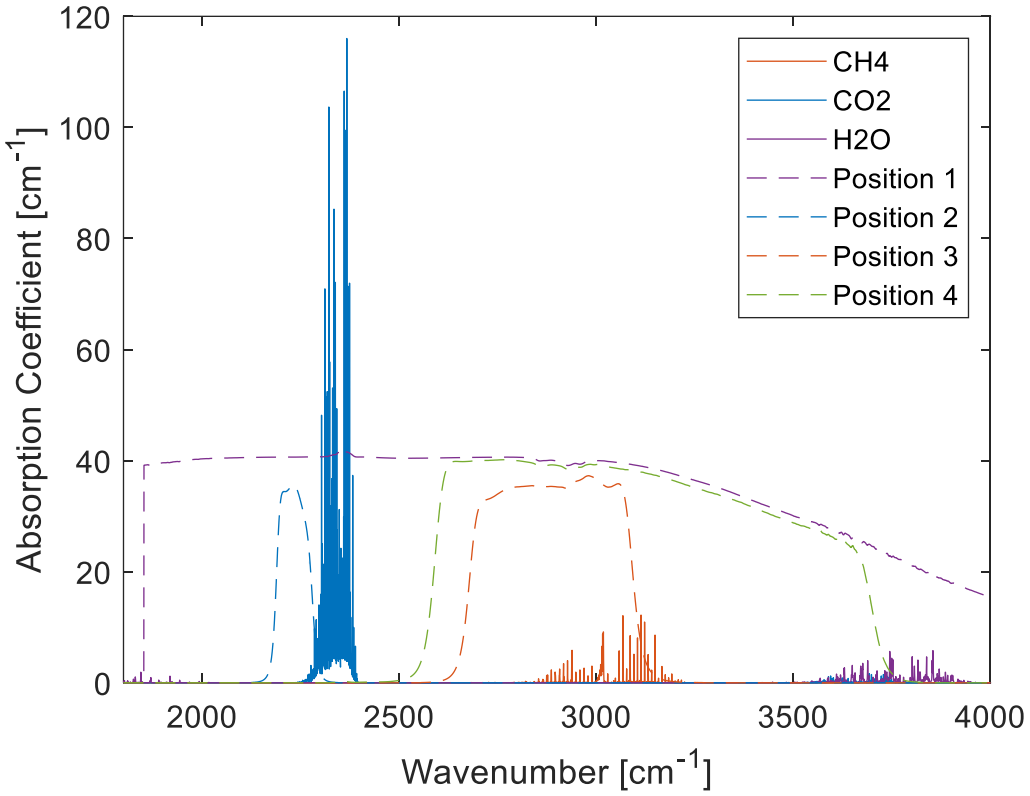

Figure 27: CH_4, CO_2, and H_2O spectral absorption coefficients alongside filter transmittances

4.1.2 Initial experimental observations

The FAST M150 being a 4-position filter wheel camera means that up to 4 parameters can be inferred simultaneously. The experimental design to validate QOGI using this camera aimed to maximize the capability of the additional spectral channels and involved releasing a mixture of heated CH_4 and CO_2. The QOGI will infer the two species' peak volume fractions, gas temperature (assumed to be the same for both gases), and plume LOS thickness. Several combinations of mixture ratio, flow rate, gas temperature, and background temperature were used but only one test case will be explored in depth because of thermal emission from the filters, which precluded accurate QOGI. The chosen test case uses a 50/50 mixture (by volume) of CH_4 and CO_2 at 10 SLPM total with a heated hose temperature

setpoint of 180°C and a background temperature setpoint of 15.0°C. The gas temperature measured at the stack exit was about 90°C. The actual background temperature was 15.6°C according to the FAST M150 and an infrared thermometer. The measurement duration was 10 seconds at a frame rate of 100 Hz which produced 1000 frames.

Looking at the radiometric temperature images in Figure 28 and Figure 29 reveals two problems immediately with the measurements from the filtered channels. First, the background temperatures of the plates in the filtered channels are much higher than the actual temperature of 15.6°C. Second, there appears to be some vignetting which inflates the pixel values near the edges of the image. It was later discovered that the increase in radiometric temperatures is due to emission from the uncooled filters which is increasing the intensity received by the FPA. By conservation of energy, light incident on the filter can be absorbed, reflected, or transmitted. As shown by the filter transmittance measurements in Section 4.1.1, the filters do not transmit 100% of the incident light so a fraction must be absorbed or reflected. According to Kirchhoff's law, the spectral directional emissivity must be equal the spectral directional absorptivity for any surface. Assuming the filters are diffuse surfaces, this means that the wavelengths of light that are absorbed by the filter will also be emitted by the filter. Therefore, the filters will emit light according to their spectral emissivity and temperature. This is problematic if the radiance from the scene is comparable to the radiance from the filter because the measured intensity will have a considerable amount of error due to the warm filter emission. After reviewing the camera calibration report, it was discovered that the validated temperature ranges for the filtered channels are much higher than the scene temperatures being used, as seen in Table 3.

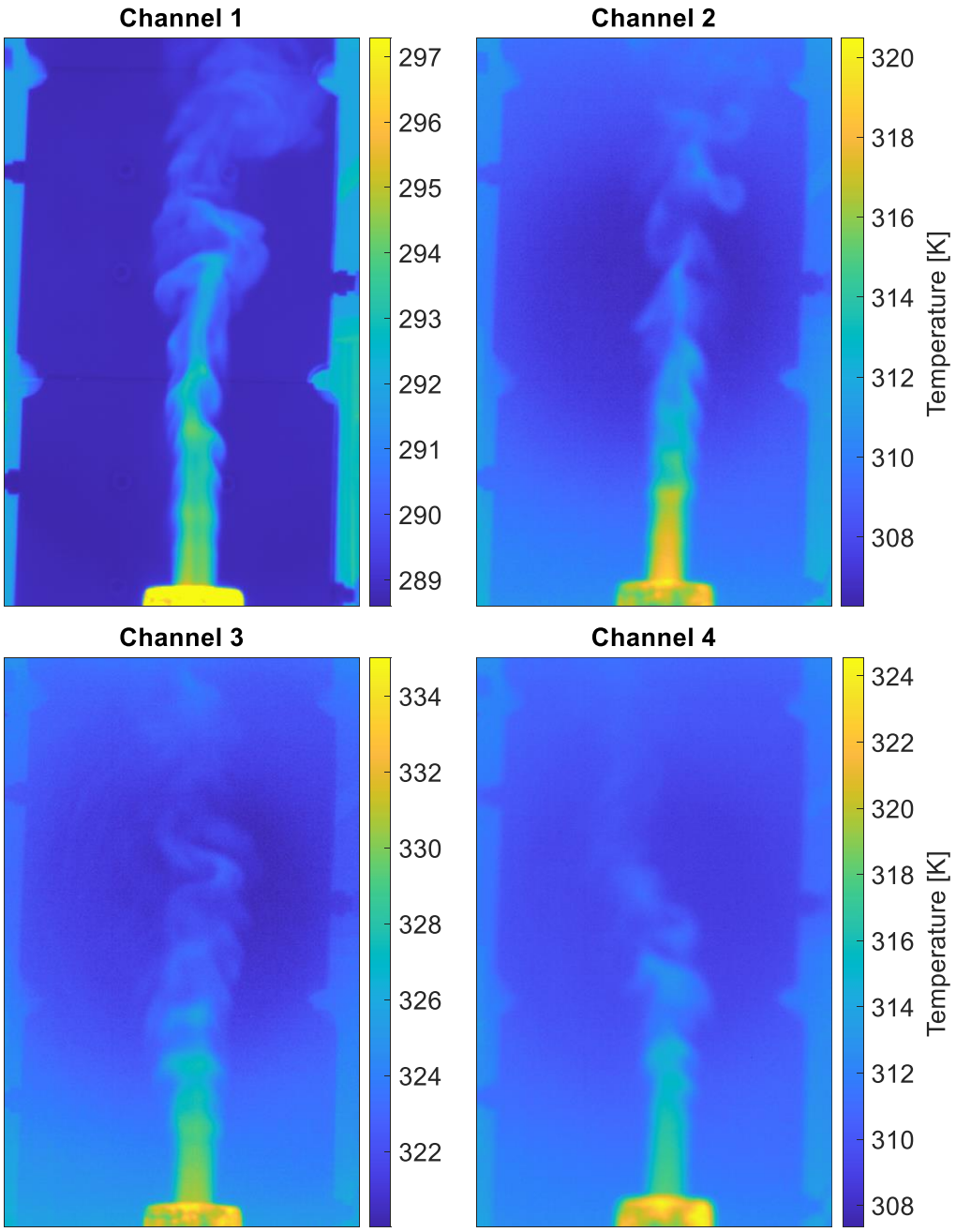

Figure 28: FAST M150 instantaneous radiometric temperature images of heated CH_4 and CO_2 through controlled release apparatus

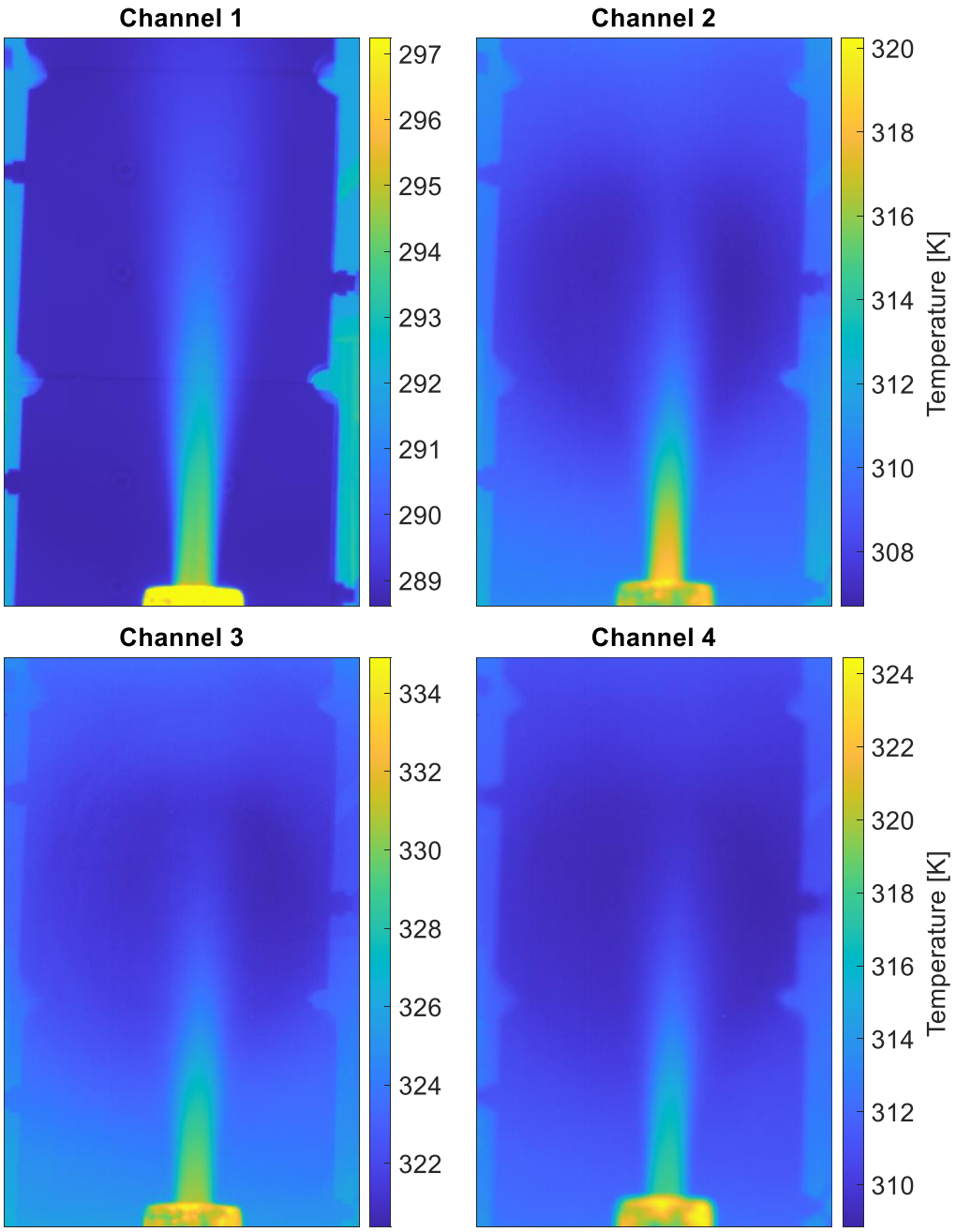

Figure 29: FAST M150 time-averaged radiometric temperature images of heated CH_4 and CO_2 through controlled release apparatus

Table 3: FAST M150 calibration temperature ranges

	Calibration Temperature Min [°C]	Calibration Temperature Max [°C]
Channel 1	0	333
Channel 2	125	374
Channel 3	136	320
Channel 4	112	301

Based on the calibration temperature ranges, it cannot be expected that the manufacturer's calibration is accurate for the temperatures of the current experiment. An accurate background temperature can still be measured from channel 1 but any values from the filtered channels are expected to be outside the calibration range.

The calibrated intensities from the manufacturer's calibration can be verified using the Planck function. The true blackbody intensity emitted by the background plates in the wavelength range of the FAST M150 can be found by integrating the Planck function in Equation (13) between the wavelength range of the camera (1.5 to 5.4 μm or 1852 to 6667 cm^{-1}) at the blackbody temperature of 15.6°C (288.7 K). This gives a value of 2.09 W/m^2-sr which is very close to the background intensity measured in position 1 which does not contain a filter. However, this intensity is attenuated by the lens (and filters in the other channels) which means a different background intensity is expected to be incident on the FPA. To estimate the background blackbody intensity incident on the FPA in each of the filter wheel positions, Equation (13) is multiplied by the filter and lens transmittance then integrated over the wavelength range of the camera.

Table 4: Expected and measured background intensities from each channel of the FAST M150

	Expected Background Intensity Including Lens Attenuation [W/m^2-sr]	Expected Background Intensity Excluding Lens Attenuation [W/m^2-sr]	Measured Background Intensity [W/m^2-sr]
Channel 1	1.67	2.09	2.10
Channel 2	0.124	0.153	0.425
Channel 3	0.054	0.067	0.311
Channel 4	0.104	0.131	0.328

In channel 1, the expected background intensity through the lens incident on the FPA is 1.67 W/m^2-sr but the measured intensity is 2.10 W/m^2-sr which is very close to the actual background blackbody intensity of 2.09 W/m^2-sr. This indicates that the calibration of the camera is able to eliminate the intensity offset created by the emission from the lens. However, for the filtered channels the measured background intensity is consistently higher than the expected intensities due to filter emission. These incorrect intensities could not be used to perform QOGI.

4.1.3 Manual calibration in lower temperature ambient conditions

To further investigate and potentially mitigate the warm filter emission problem, a manual calibration of the camera was performed at room temperature and at 8°C outdoors using the cooled plates of the controlled-release apparatus. The filters and camera body are expected to be at ambient temperature; therefore the filters will have been slightly cooled. The calibration procedure has been discussed in Section 2.5. The calibration was performed over a range of background temperatures from 3.5°C to 60°C which should be sufficient for the temperatures expected in the lab experiments. First, the calibration was performed at a room temperature of 21°C and the results are shown in Figure 30 and Figure 31.

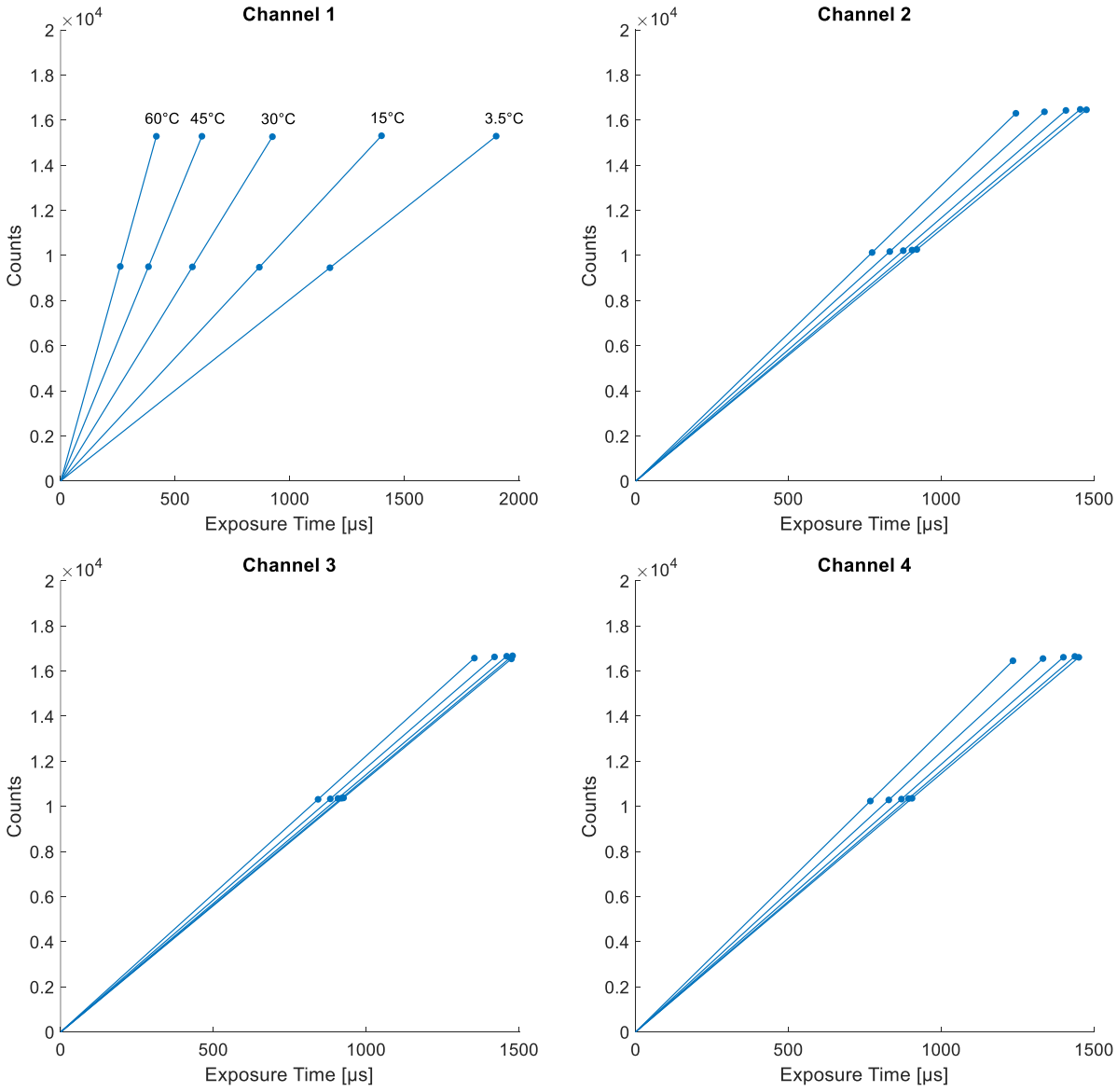

Figure 30: Counts versus exposure time calibration curves for FAST M150 at room temperature

The counts versus exposure time curves in Figure 30 for channels 2, 3, and 4 are tightly grouped which shows that as the radiance from the blackbody source increases with temperature, the response of the camera changes only slightly. This demonstrates a problem with the uncooled filters because a small change in the measured counts would indicate a large change in temperature, at least at the chosen

temperature range. The response curves for channel 1 without a filter are more separated and enable more precise calibration. A good observation from the curves in Figure 30 are that they all intersect the vertical counts axis at essentially zero for zero exposure time. This is consistent with the idea that the camera should measure zero photons with an exposure time of zero.

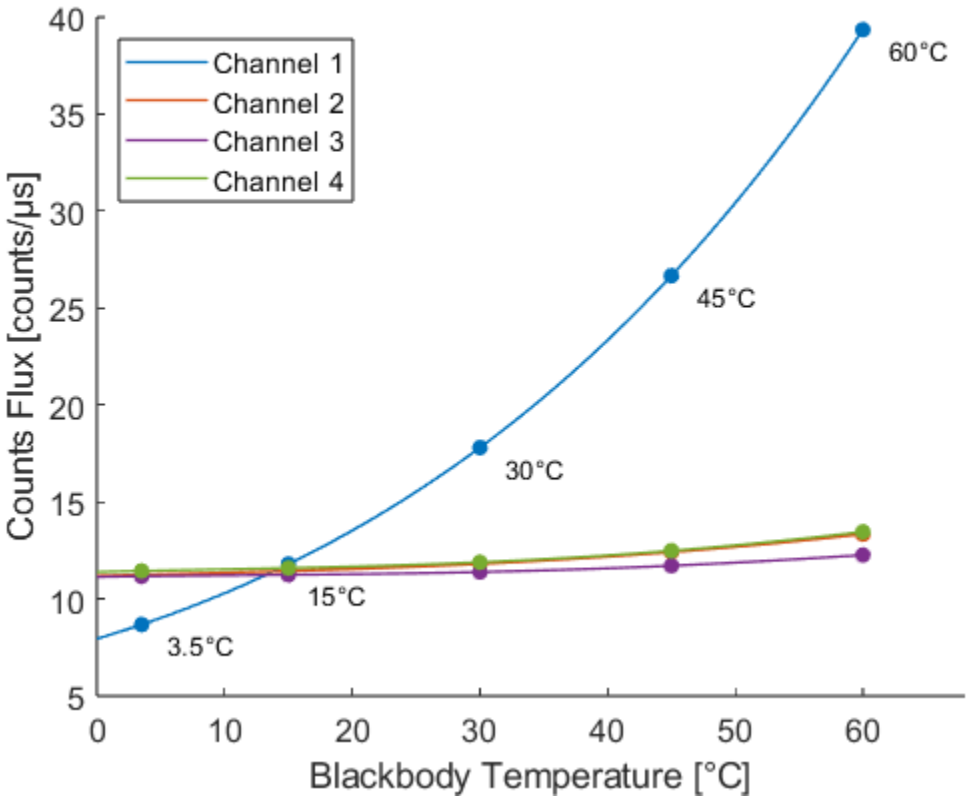

Figure 31: Counts flux versus blackbody temperature calibration curves for FAST M150 at room temperature

Looking at the counts flux versus blackbody temperature curves in Figure 31, channels 2, 3, and 4 are tightly grouped once again and mostly flat unlike the calibration curve for channel 1. The curvature of the counts flux curves in Figure 31 indicates the sensitivity of the camera response to the scene radiance or temperature, so it's clear that the filtered channels are less sensitive compared to the

unfiltered channel. The lower sensitivity of the filter channels is fundamentally due to the narrow widths of the bandpass filters; the bandpass reduces the intensity incident on the FPA and therefore the signal response to a change in temperature will be less for the filtered channels. Another observation from Figure 31 is that below a blackbody temperature of about 14°C, the counts flux curves of the filtered channels exceed that of the unfiltered channel. This means that the camera response of the filtered channels below this temperature is greater than the unfiltered channel which is unintuitive considering the bandpass filters attenuates the incident intensity for all scenes. The best explanation is that the emission from the uncooled filters has become higher than the radiance from the scene for blackbody temperatures below 14°C. Cooling the filters will decrease their emitted radiance so the calibration was redone outdoors in 8°C ambient conditions.

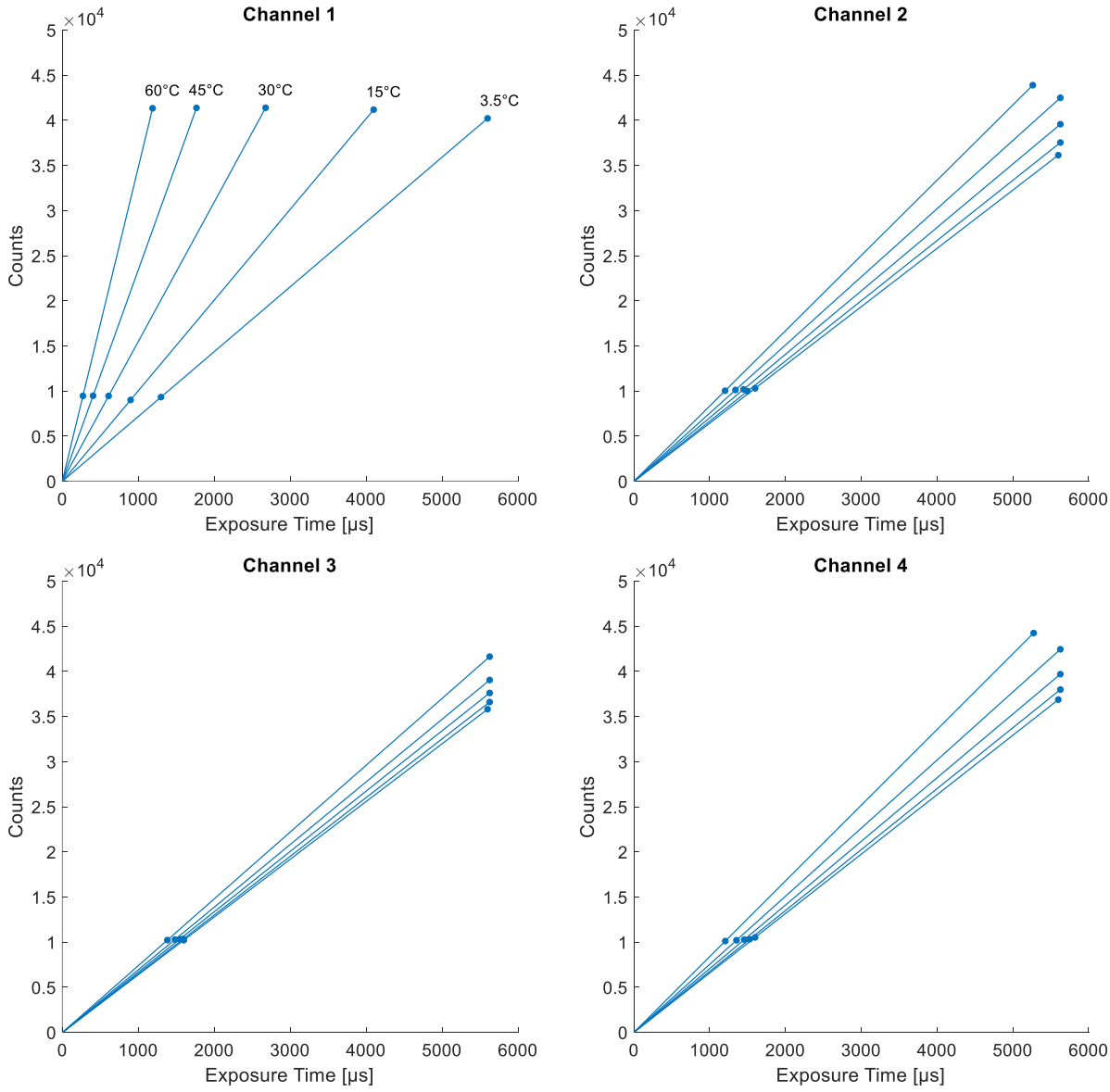

Figure 32: Counts versus exposure time calibration curves for FAST M150 at 8°C

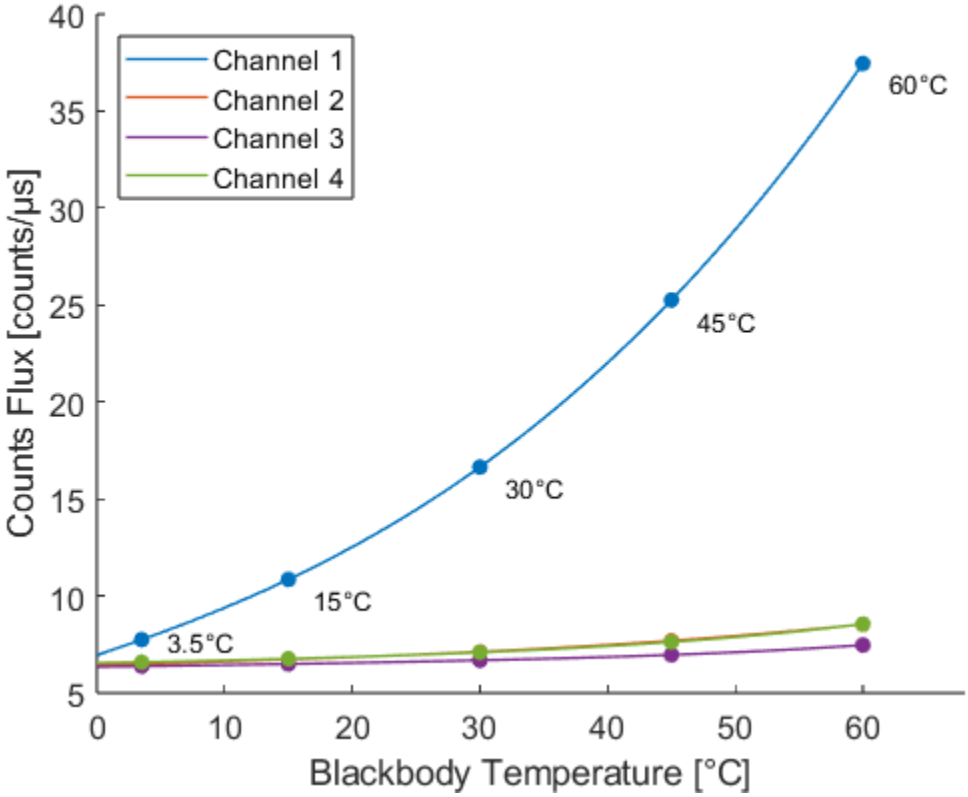

Figure 33: Counts flux versus blackbody temperature calibration curves for FAST M150 at 8°C

Not much appears to have changed with the counts versus exposure time curves in Figure 32 by cooling the filters, however the counts flux curves of the filtered channels in Figure 33 have clearly shifted downwards indicating a decrease in signal for all blackbody temperatures. This is consistent with the warm filter emission hypothesis since the filters have been cooled to near 8°C and therefore emit with less intensity.

4.1.4 Manually calibrated experimental results

In the same 8°C ambient conditions which the manual calibration was performed, the controlled-release apparatus was used to vent 10 SLPM of CH_4 and CO_2 at a 50/50 ratio and heated hose temperature of 180°C once again. The background temperature was set to 3.5°C and verified with an infrared thermometer. The measurement duration was 8 seconds at a frame rate of 100 Hz which produced 800 frames. Figure 34 shows the time-averaged radiometric temperature images which reveal that the temperatures from the filtered channels are still higher than expected due to filter emission. The background temperatures of the plates according to the manual calibration are given in Table 5. Another observation from the outdoor tests is the effect of wind on the plume which clearly moves to the left after it exits the stack.

Table 5: Background temperatures from FAST M150 after manual calibration, 3.5°C actual

	Background Temperature
Channel 1	4.4°C / 277.5 K
Channel 2	16.8°C / 289.9 K
Channel 3	26.5°C / 299.6 K
Channel 4	18.5°C / 291.6 K

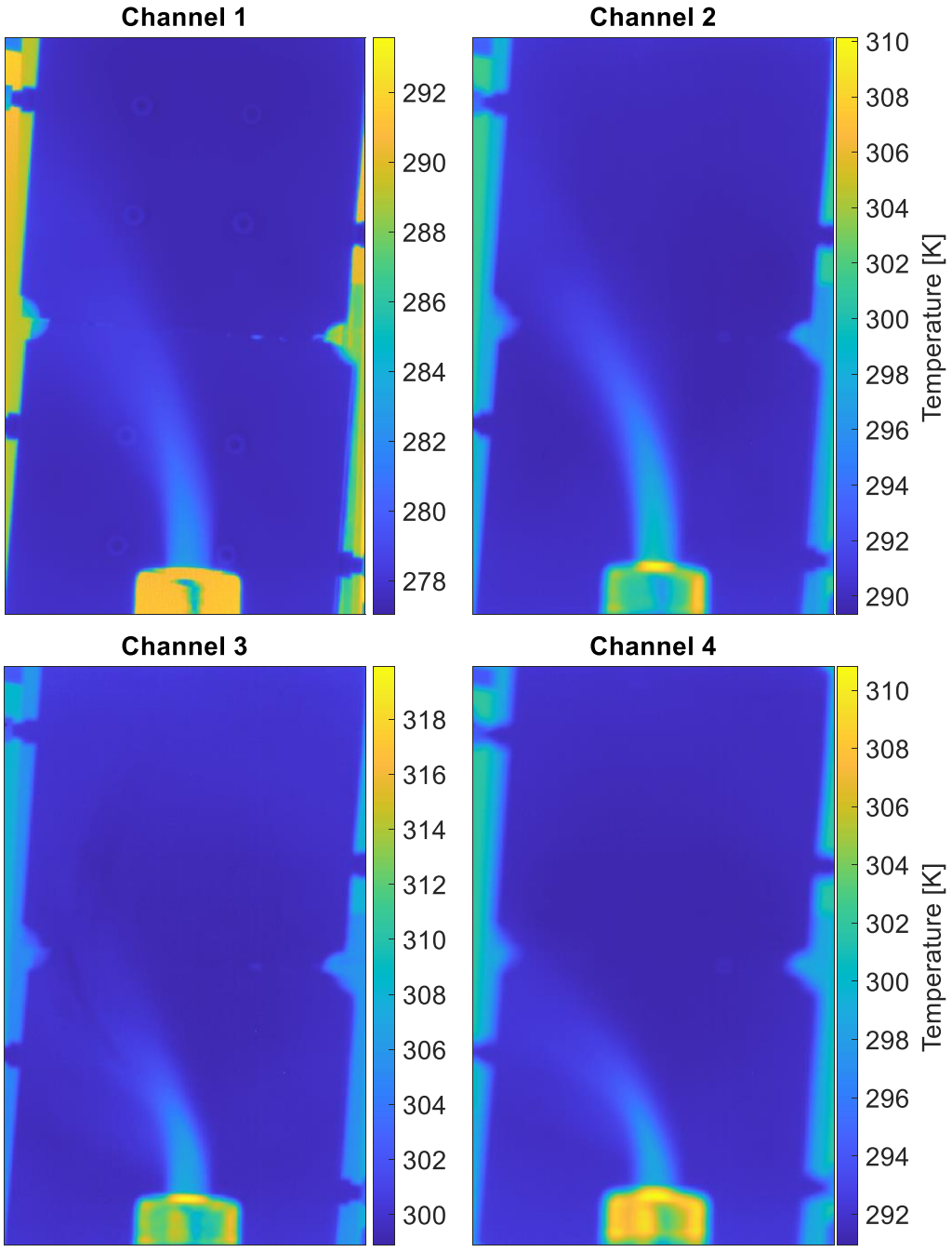

Figure 34: FAST M150 time-averaged, manually calibrated radiometric temperature images of heated CH_4 and CO_2 in 8°C ambient conditions

Despite the inaccurate pixel intensities due to filter emission, a QOGI analysis can still be performed to examine the effects. The control surface is placed about 1 cm above the stack exit and the inferred parameters are: 1) peak CH_4 volume fraction, 2) peak CO_2 volume fraction, 3) peak temperature, and 4) LOS plume thickness. The peak temperature and LOS plume thickness parameters are non-dimensionalized between 0 and a realistic maximum value to accommodate the least-squares solver. To maximize the intensity from the gas the control surface is drawn near the stack exit where the gas temperature and path concentration are highest.

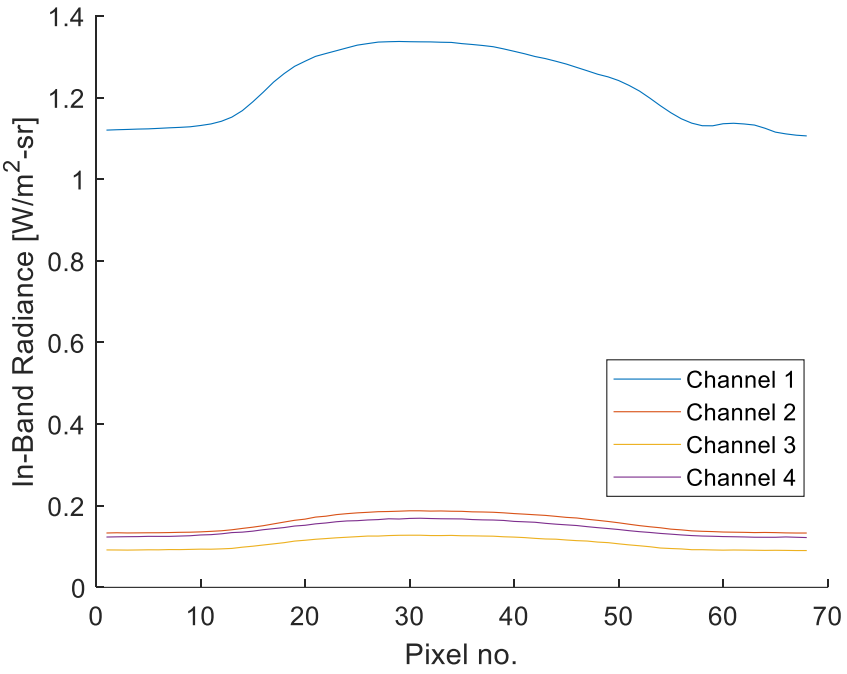

Figure 35: FAST M150 manually calibrated pixel intensities across control surface

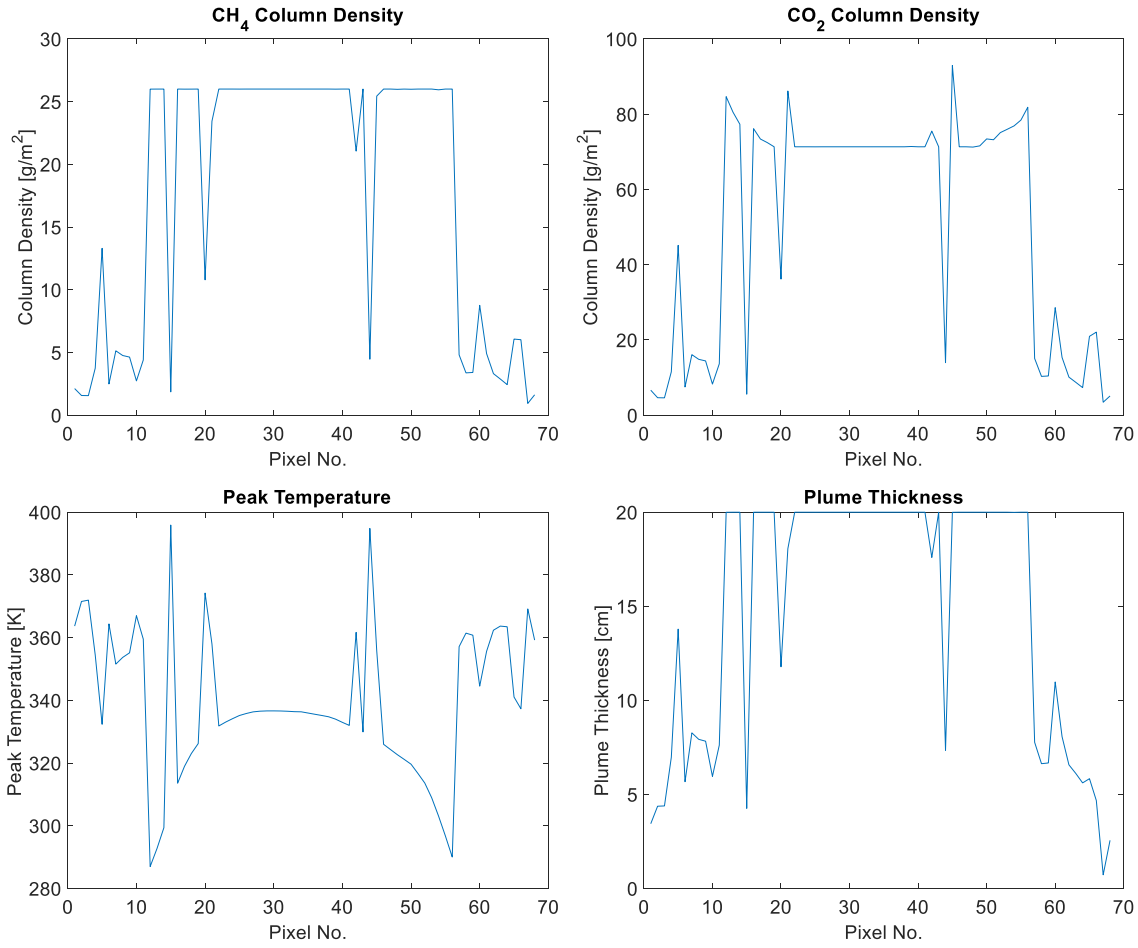

Figure 36: FAST M150 QOGI-inferred parameters for heated gas release outdoors

Looking at Figure 36, it is immediately clear that there is a lot of noise in the inferred results. This is due to the ill-posedness of the problem which can amplify small amounts of error or noise in the pixel intensities into large errors in the solution. Aside from the noise in the inferred results, one other key observation can be made: the bias in intensity due to filter emission causes the inferred parameters to be higher to account for the higher intensity in the filtered channels. In fact, Figure 37 shows that the non-dimensional solution parameters for the species volume fractions and plume thickness are reaching the upper bounds set in the script. For the species volume fractions, there physically cannot be more

than 100% of the species at a point in the plume. For the plume thickness, the stack exit diameter is about 2 cm and the upper bound was set as 10 cm. Even with an unrealistic plume thickness and peak volume fractions of 100% the solution cannot explain the intensity in the filtered channels. The plume temperature is realistic, however, peaking at 337 K or 64°C when the temperature of the gas in the stack is about 90°C. This is because channels 3 and 4 both capture CH_4 and although their measurements are incorrect in absolute terms, their relative intensities can be used to infer the temperature.

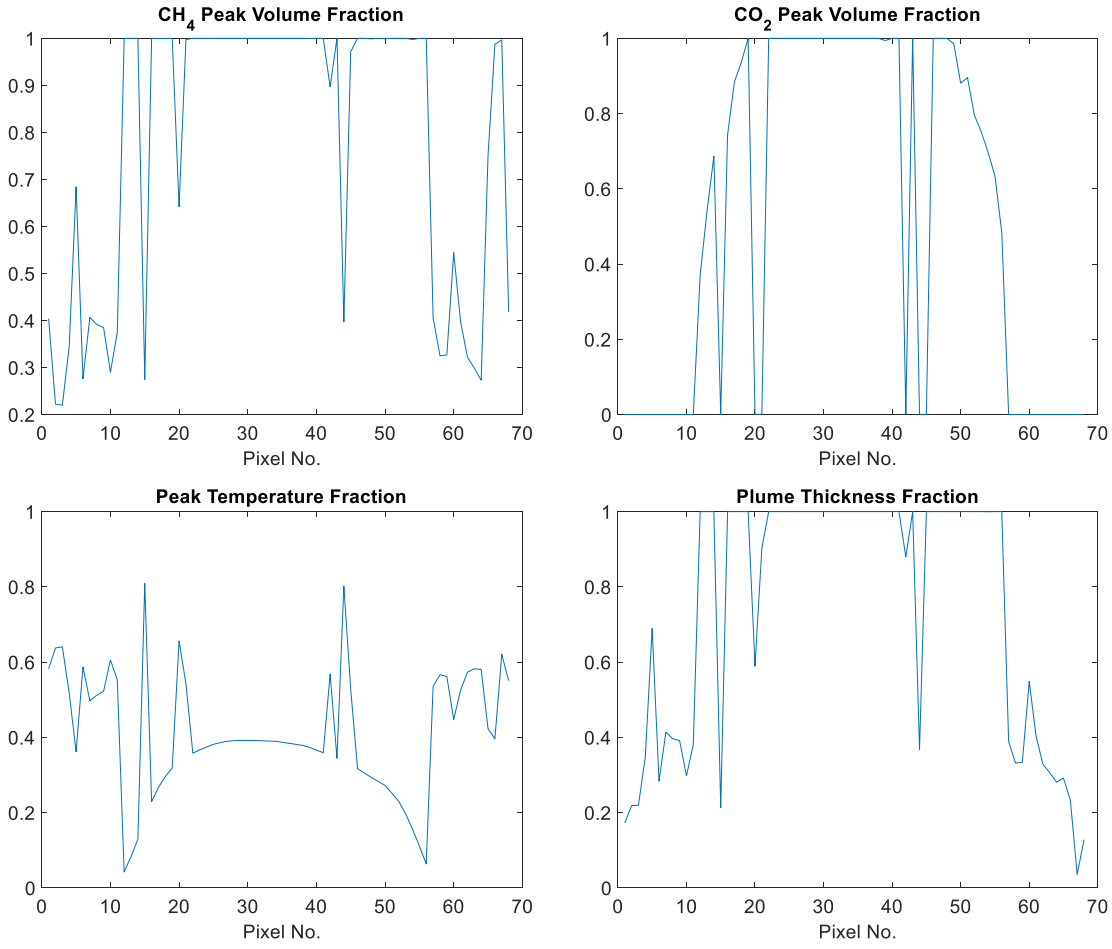

Figure 37: FAST M150 QOGI-inferred non-dimensional parameters for heated gas release outdoors

Despite the problems in the spectroscopic model caused by the filter emission, the optical flow velocimetry can still be tested in isolation. Figure 38 shows the time-averaged velocity field over 8 seconds and 800 frames using the Horn-Schunck optical flow algorithm. The optical flow algorithm is able to determine the direction of the flow in general, however the velocity field near the stack exit appears to be near-zero since the pixel brightnesses are typically constant between frames in this area. The maximum velocity in the time-averaged velocity field is 0.17 m/s which is reasonable although a ground-truth cannot be obtained. The average velocity of the gas exiting the stack based on the volumetric flow rate of 10 SLPM and diameter of 1.9 cm is 0.59 m/s which is much greater than the optical flow estimates. Manually tracking a few turbulent structures across frames, counting the pixel displacements, and dividing by the time between frames gives a velocity of about 0.3 m/s. Considering that the turbulent structures often move faster than the bulk fluid, a maximum time-averaged velocity of 0.17 m/s seems to be a reasonable estimate. Thus the optical flow velocimetry performed well in this experiment with the FAST M150 due to its fast frame rate of 100 Hz.

If the column densities from the spectroscopic model were believed to be accurate at this point, the mass flow rate of each species could be determined by multiplying the column densities and the velocities and integrated across a control surface. However, the spectroscopic model was affected by filter emission and the analysis of data from this experiment will not proceed.

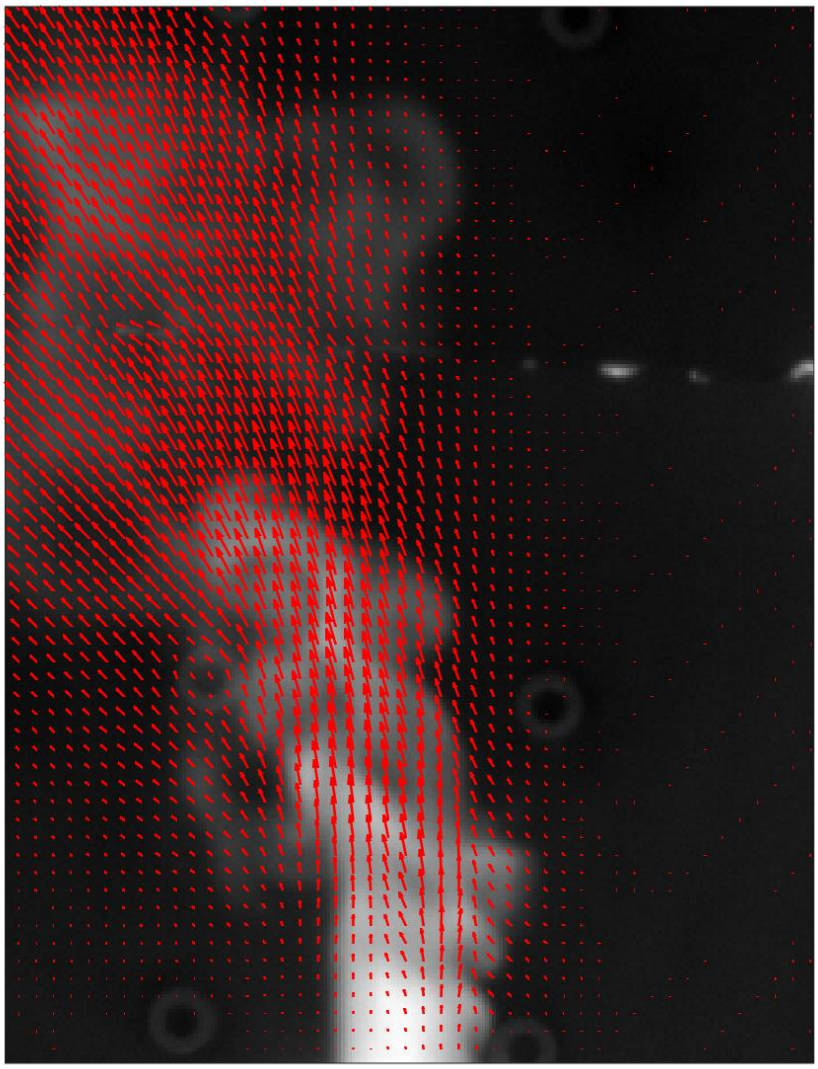

Figure 38: FAST M150 time-averaged velocity field from optical flow

A block diagram of the camera's optical elements with the transmitted and emitted spectral intensities is shown in Figure 39. This model was used to explain and potentially correct the warm filter emission problem. The spectral intensity from the scene I_λ enters the lens and a fraction $I_{\lambda,\tau}$ is transmitted. By conservation of energy, the wavelengths of light that are not transmitted must be absorbed or reflected and by Kirchhoff's law, the spectral absorptivity is equal to the spectral emissivity

assuming the surface is diffuse. Therefore, $I_{\lambda,\varepsilon+\rho}$ is the emitted plus reflected spectral intensity from the lens which is the complement of the lens transmittance times the blackbody spectral intensity at the camera body temperature. This separation of transmitted, emitted, and reflected spectral intensities continues through the externally-mounted bandpass filters and internally-mounted filter before the FPA. Since the transmittances of the lens and external filters were measured using the FTIR and the camera body is approximately at ambient temperature, the emitted and reflected spectral intensities can be calculated and subtracted from the measured signal. Unfortunately, this ended up being inaccurate presumably because the optical properties of the internal filter could not be measured and the spectral response function of the FPA is not known and could not be considered. These details in the spectroscopic model of the camera's optical path are critical in accurately calculating the warm filter emission component of the measured intensity.

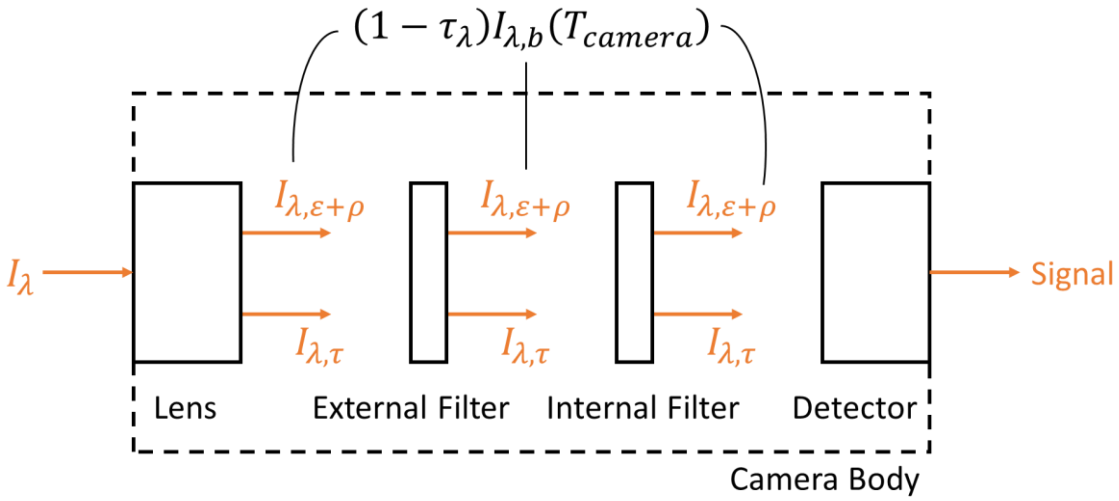

Figure 39: Block diagram of FAST M150 optical elements with transmitted and emitted intensities

4.2 Field testing

Based on the findings from the lab-scale testing with the Telops FAST-M150 and low temperature gases, the focus of the field testing with the multispectral camera was on high temperature gases from the flare and combustor. The combustor is a recent advancement and improvement on flares wherein the methane is combined with a controlled amount of air and combusted inside a vertical column to achieve higher conversion efficiency. The objective of the field testing with the FAST M150 was to trial the camera and QOGI algorithms on high temperature CH_4 and CO_2.

Figure 40: Alberta field measurements (left) methane release into lit flare (right) combustor

The ideal stoichiometric combustion reaction of methane in air is as follows:

$$CH_4 + 2O_2 \rightarrow CO_2 + 2H_2O \tag{16}$$

For a calculation of combustion efficiency, the species of interest are CH_4 and CO_2 in order to perform a mass balance on carbon and calculate the conversion efficiency between products and reactants. Figure 27 showed that these two species are present in the spectral range of the FAST M150 and its filters. H_2O is also present in the unfiltered and fourth channels which means it should be considered in the spectroscopic model. Incomplete combustion may also lead to the formation of CO and soot. CO has spectral absorption lines in the 2000 to 2250 cm^{-1} (4.44 to 5.00 μm) which is captured by the second channel, while soot behaves like a broadband emitter in the MWIR [60][61]. Soot formation from methane combustion is expected to be relatively low at atmospheric pressure [62][63][64] if the flare or combustor are operating in ideal conditions. However, soot is visibly apparent in the flare as evident by the yellow-orange flame and black smoke on the left of Figure 40. Simultaneously inferring peak temperature and peak CH_4, CO_2, CO, H_2O, soot volume fractions with a four-channel multispectral camera is severely ill-posed so QOGI is not expected to perform well in this scenario. Nonetheless, the field measurements provided useful insights into the operation of the multispectral camera and measuring the flare and combustor. The optical flow velocimetry can also be trialed and compared to the wind speed for reference.

4.2.1 Flare measurements

Figure 41 shows the radiometric temperatures images of the flare from each of the four channels using the FAST M150. One of the challenges in making the measurement of the flare was selecting an exposure time that balanced the intensity from the background and flare. As seen in each of the channels and, especially, the filtered channels, the background pixels contain a lot of noise because the exposure time was not long enough to acquire enough photons to overcome the FPA noise. Meanwhile, the highest intensity pixels of the flare and wind collar are saturated or exceed the calibration limits. This means only a fraction of pixels have correct values usable for QOGI. After consulting with Telops, the

recommendation was made to use their EHDRI (Enhanced High Dynamic Range Imaging) functionality which uses a number of exposure times sequentially during an acquisition to maximize the information from the scene. Unfortunately, the measurements could not be repeated with this functionality in the field trial but still informs future research when measuring scenes with a wide temperature range.

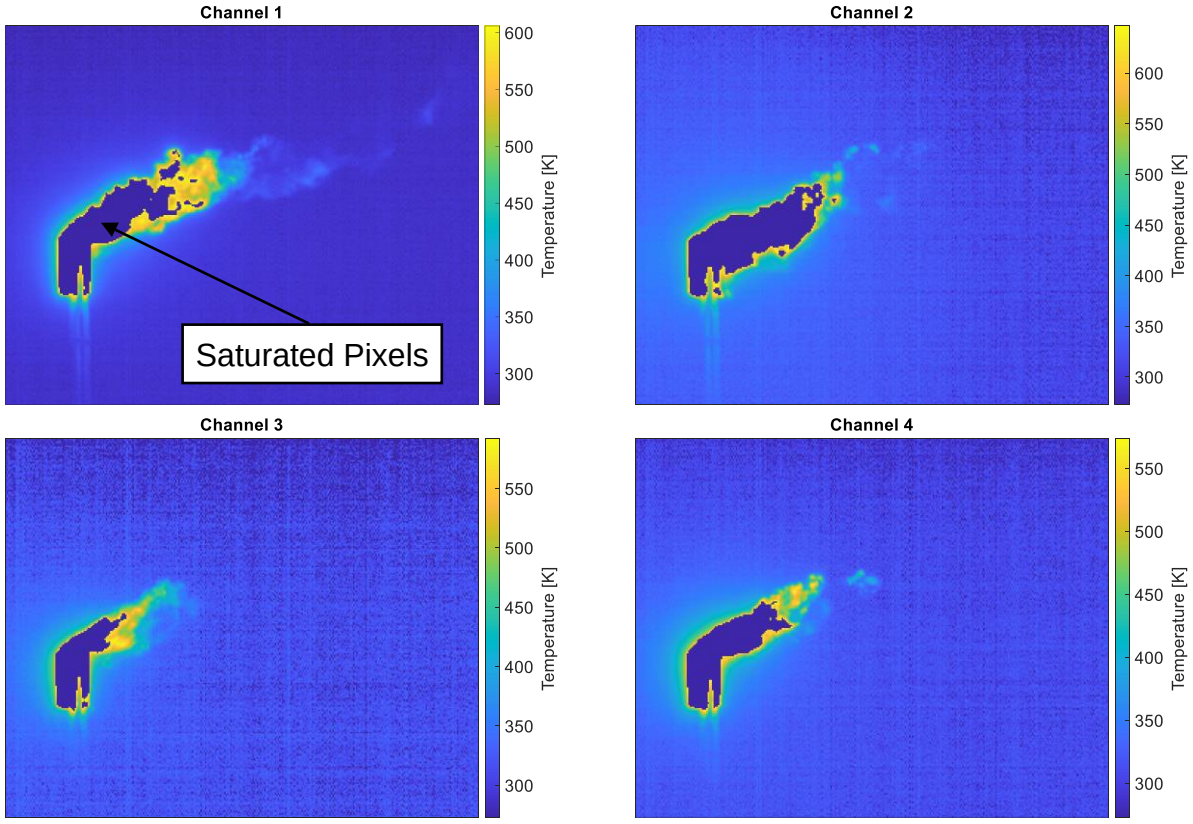

Figure 41: Radiometric temperature images of flare from Alberta field testing using FAST M150

Due to the fixed nature of the FAST M150 filter wheel, the images from each channel are not sequential and therefore it is not possible to comment on the ability of the multispectral camera to distinguish different species instantaneously. For example, channel 3 isolates CH_4 and channel 4 isolates CH_4 and H_2O and it seems the channel 4 in Figure 41 has a greater number of pixels with gas

which could be due to the inclusion of H_2O. However, the flare is very unstable and the two images are uncorrelated in time which makes it difficult to draw definitive conclusions.

One other observation is of the number of high intensity pixels in channel 3. The bright pixels could indicate either unburned CH_4 or soot, both of which are critical to the motivation of this research and may be quantifiable with a more capable multispectral camera and HDR imaging.

The final observation is that there appears to be some blooming around the highest temperature pixels which increased with exposure time. The hypothesis is that this is due to diffusion of light in the lens and filters. The blooming artifact affects the background pixels, which do not have sufficient signal to begin with, and so the calibration into radiometric temperature is amplifying the effect due to the Planck relation with intensity. The RAW, NUC, and in-band radiance images exhibit less blooming.

Optical flow velocimetry was performed over 10 seconds at 200 Hz corresponding to 2000 frames. The average velocity field is shown in Figure 42. The maximum velocity obtained is about 7 m/s whereas the wind speed at the time was about 4 m/s and gusting up to 6 m/s. The velocities near the bright flare tend to be lower because the brightness is relatively constant, however, this still seems to be a positive result for the optical flow velocimetry.

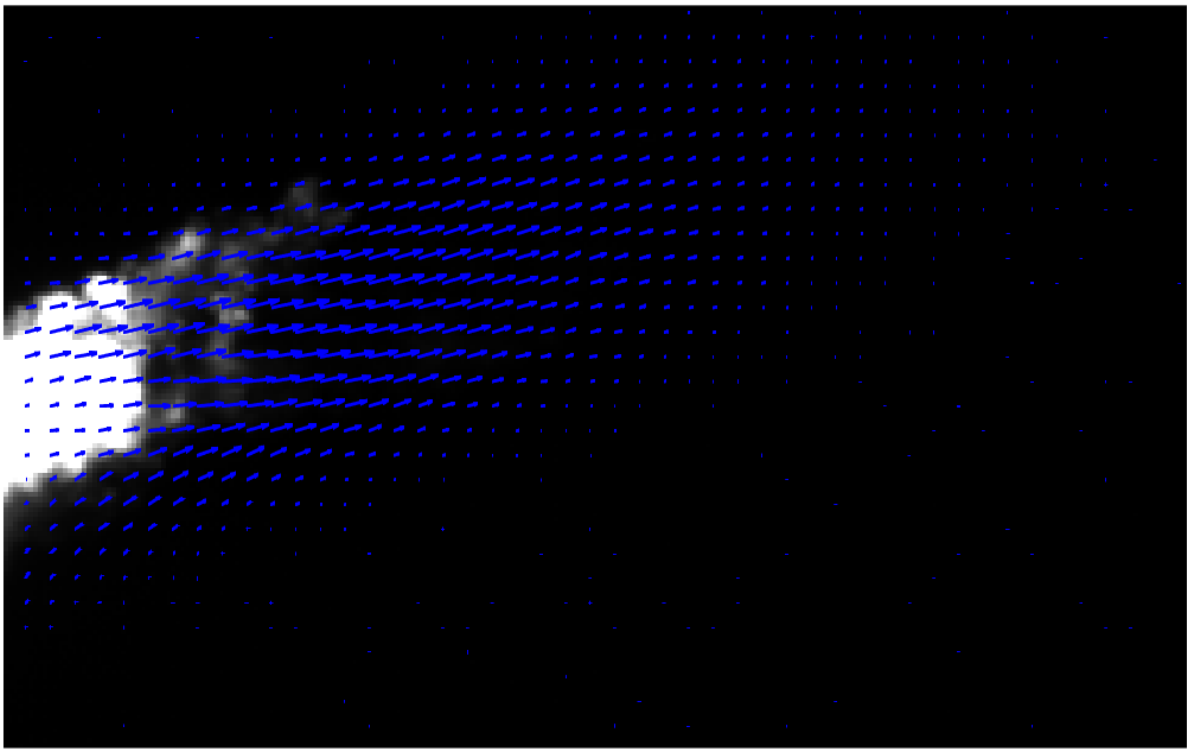

Figure 42: Average velocity field of flare from Alberta field testing using optical flow velocimetry

4.2.2 Combustor measurements

Figure 43 shows the radiometric temperature images of the combustor with the FAST M150. Saturation still occurs in some pixels but in general higher exposure times had to be used because the majority of the combustion was occurring inside the vertical stack and only the combustion products are imaged. Considering that the combustor is expected to be over 90% efficient in converting CH_4, channel 3 should only be used to visualize the oxidized soot which was not visible to the eye. Channel 4 then captures the water vapour which is contained in many more pixels.

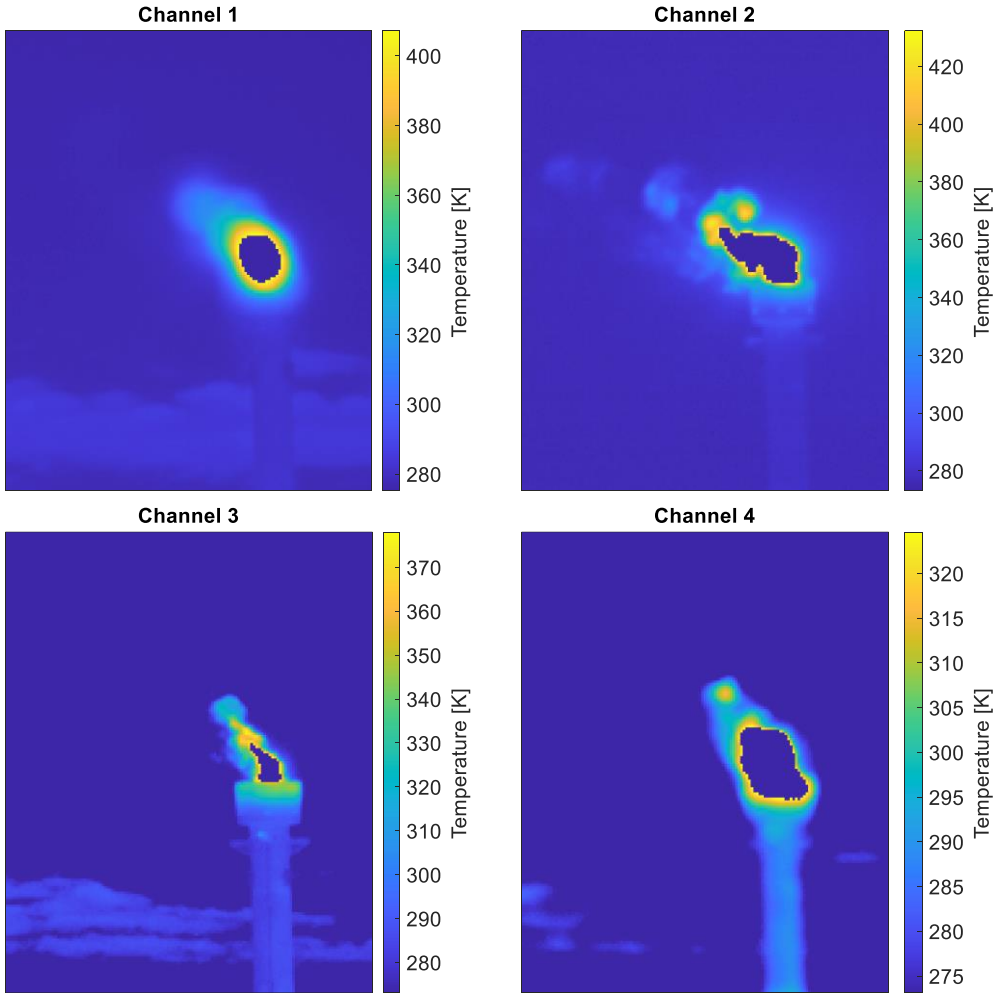

Figure 43: Radiometric temperature images of combustor from Alberta field testing using FAST M150

4.3 Simulation

To overcome the problem caused by the uncooled filters in the FAST M150 multispectral camera and evaluate the performance of the spectroscopic and velocimetry models independently, a CFD-Large Eddy Simulation was setup of a gas release so that the advantages of cooled-filter multispectral QOGI can be demonstrated.

4.3.1 Setup, camera model, and noise model

The CFD-LES software used is Fire Dynamics Simulator (FDS) by the National Institute of Standards and Technology (NIST) of the United States Department of Commerce [65]. A gas plume is simulated with a specified composition, flow rate, temperature, and ambient conditions. The CFD-LES simulation of the gas plume provides the 3D distributions of species volume fractions, temperatures, pressures, and velocities. Then the RTE is used to calculate the spectral intensity along each LOS through the plume and into a hypothetical multispectral camera to produce synthetic images. The multispectral camera is modeled after the Telops FAST M150 in terms of spectral range and filters, except the bandpass filter of channel 2 is shifted by 110 cm^{-1} to better align with the spectral lines of CO_2 as seen in Figure 27. Increasing the overlap of the CO_2 spectral lines and filter transmittance improves the signal to noise ratio. Also, the effect of uncooled filter emission seen with the FAST M150 in experiments is omitted in the simulated images.

Identical and independently distributed (IID) noise is added to the synthetic images proportional to the noise specification given in the FAST M150 test report from the manufacturer. There is temporal noise inherent to the FPA which is quantified as a noise equivalent temperature difference (NETD). The NETD is calculated by dividing the standard deviation of the temporal noise by the response per degree of the camera, expressed in milliKelvins. The NETD of the FAST M150 is 17 mK and this is

replicated by adding randomly sampled intensities from a normal distribution to each pixel such that the NETD of the synthetic image is also 17 mK [66][67].

The simulation consists of a 10 cm tall vertical stack with a 2 cm hole through which the gas is released. A 50/50 mixture (by volume) of CH_4 and CO_2 at a total flow rate of 7.2 SLPM is used. The temperature of the gas at the bottom boundary is 90°C which is based on the thermocouple measurement of the gas in the controlled-release experiments. The ambient air is 20°C and the background temperature is 15°C. Wind and atmospheric instability is not simulated. The simulation domain is 1.4 m x 1.4 m x 0.3 m with a discretization of 71 x 71 x 151 resulting in a uniform element length of 2 mm in each direction. The pixel size in the controlled release experiments using the FAST M150 was about 0.5 mm but refining the simulation mesh to this size made the computation of the synthetic images intractable. The simulation duration was 10 seconds at a sampling rate of 100 Hz but the first 3 seconds are not analyzed while the flow stabilizes. The simulation required about 10 hours to complete with an AMD Ryzen 7 5800X at 4.7 MHz. Generating 700 synthetic images required about 18 hours to complete.

4.3.2 Simultaneous gas temperature and species volume fraction inference

The biggest advantage of a multispectral camera to QOGI is the ability to infer multiple parameters simultaneously. The four parameters to be inferred are: 1) peak CH_4 volume fraction, 2) peak CO_2 volume fraction, 3) peak temperature, and 4) LOS plume thickness. To mitigate the variability due to the location of the control surface, six control surfaces are used spaced 2 cm apart starting 2 cm above the release point as seen in Figure 44. Figure 45 shows the QOGI-inferred column densities and vertical velocities versus the CFD ground truth for each control surface height. Table 6 summarizes the resulting flow rates and the corresponding percentage error. The vertical velocity from the CFD is a mass-

weighted average of the velocities along each LOS, which is slightly different from the intensity-weighted average of the optical flow velocities. A mass-weighted average velocity is a more appropriate target because when multiplied by the column density, it gives the exact mass flow rate.

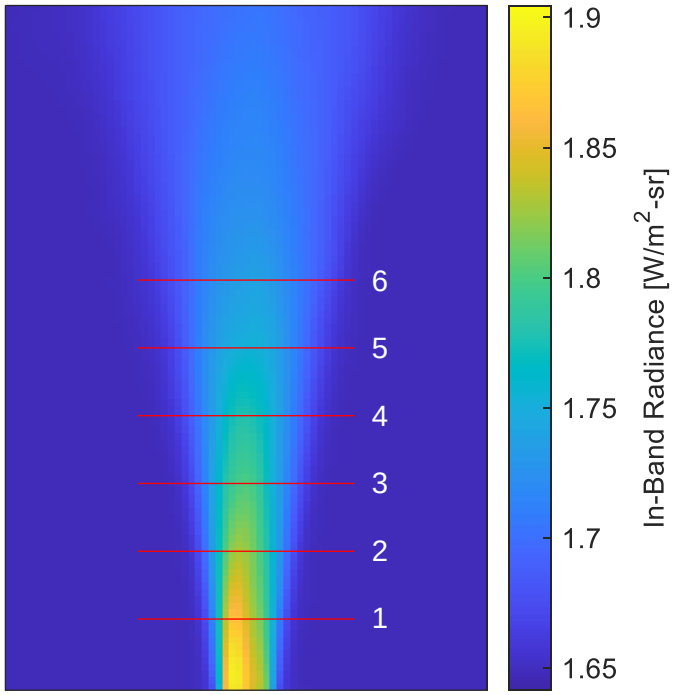

Figure 44: Time-averaged synthetic image with control surface heights for QOGI

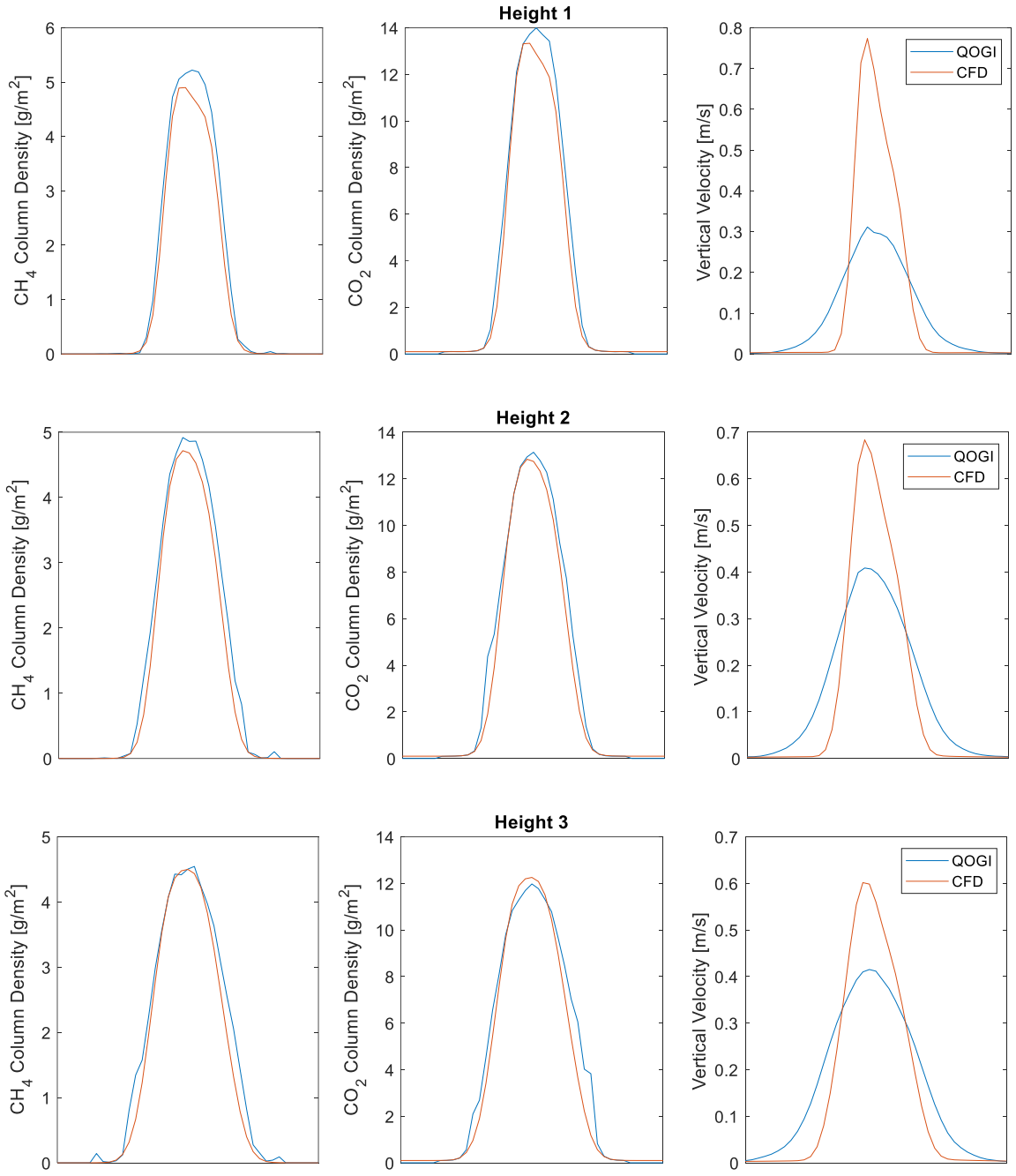

Figure 45a: QOGI-inferred column densities and velocities versus CFD ground truth

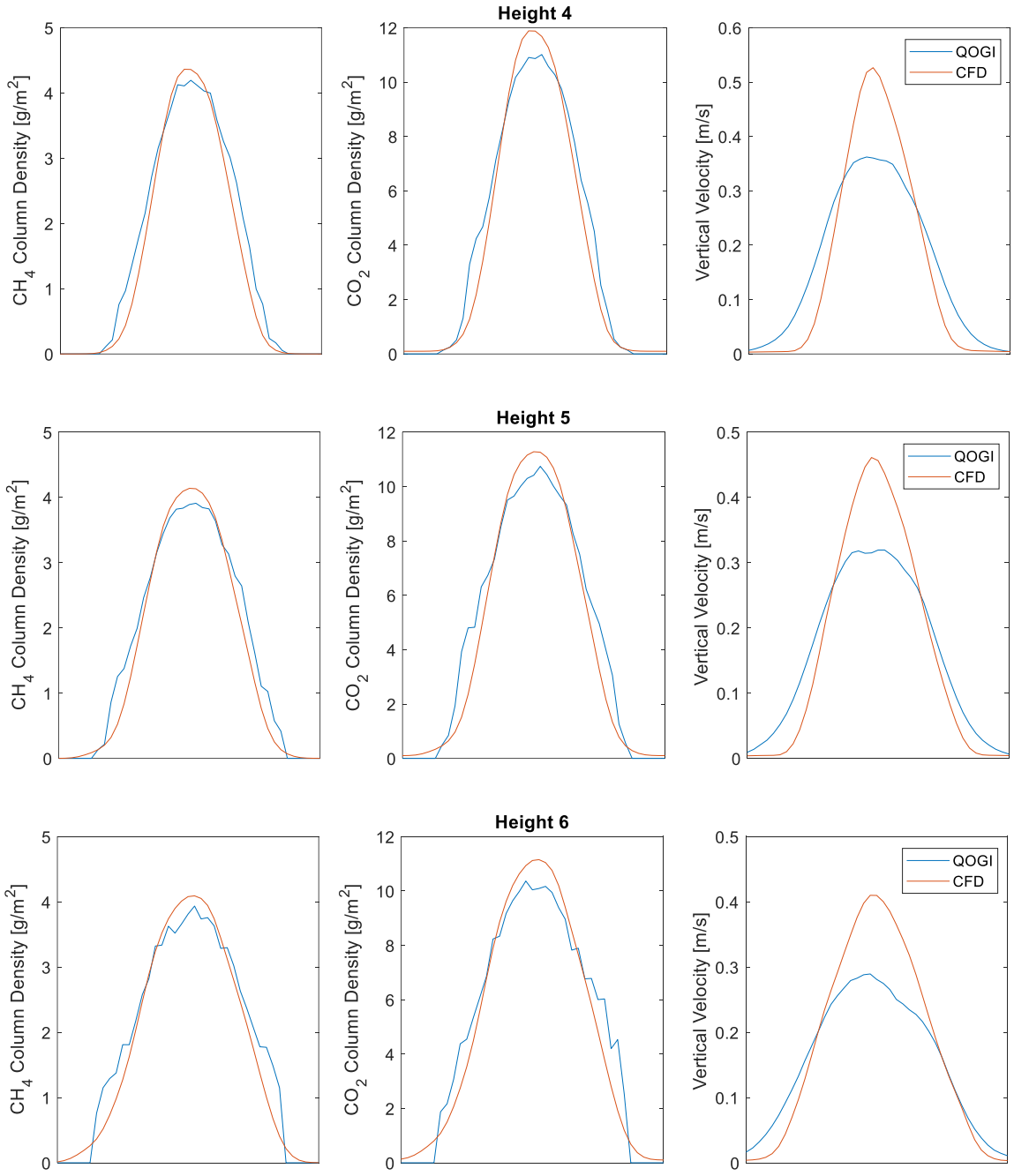

Figure 45b: QOGI-inferred column densities and velocities versus CFD ground truth

Table 6: QOGI-inferred and CFD ground truth flow rates summarized

	Flow Rate, CH_4 [SLPM]	Flow Rate, CO_2 [SLPM]
Height	**QOGI / CFD / % Error**	**QOGI / CFD / % Error**
1	2.15 / 3.64 / -41%	2.08 / 3.57 / -42%
2	3.02 / 3.65 / -17%	2.92 / 3.59 / -19%
3	3.25 / 3.65 / -11%	3.17 / 3.59 / -12%
4	3.22 / 3.63 / -11%	3.09 / 3.57 / -13%
5	3.08 / 3.61 / -15%	3.04 / 3.55 / -14%
6	2.90 / 3.65 / -21%	2.83 / 3.59 / -21%

Table 6 shows that the QOGI estimated flow rate is consistently below the CFD ground truth by 11 to 42%. Based on the results shown in Figure 45, this error is primarily due to the optical flow velocimetry as the column densities are accurate at all heights. The optical flow particularly struggles at the lowest control surface where the pixel intensities are relatively constant between frames. Figure 46 shows examples of the instantaneous column densities and velocities for two frames at control surface height 3. First, the column densities reveal quite a bit of noise due to the ill-posedness of the spectroscopic model. The optical flow improves the ill-posedness of the brightness constancy equation by imposing a smoothness constraint. Next, the inferred column densities are generally more accurate when compared to the CFD ground truth despite the noise, while the inferred velocities are close to the CFD ground truth in most frames but very inaccurate in other frames.

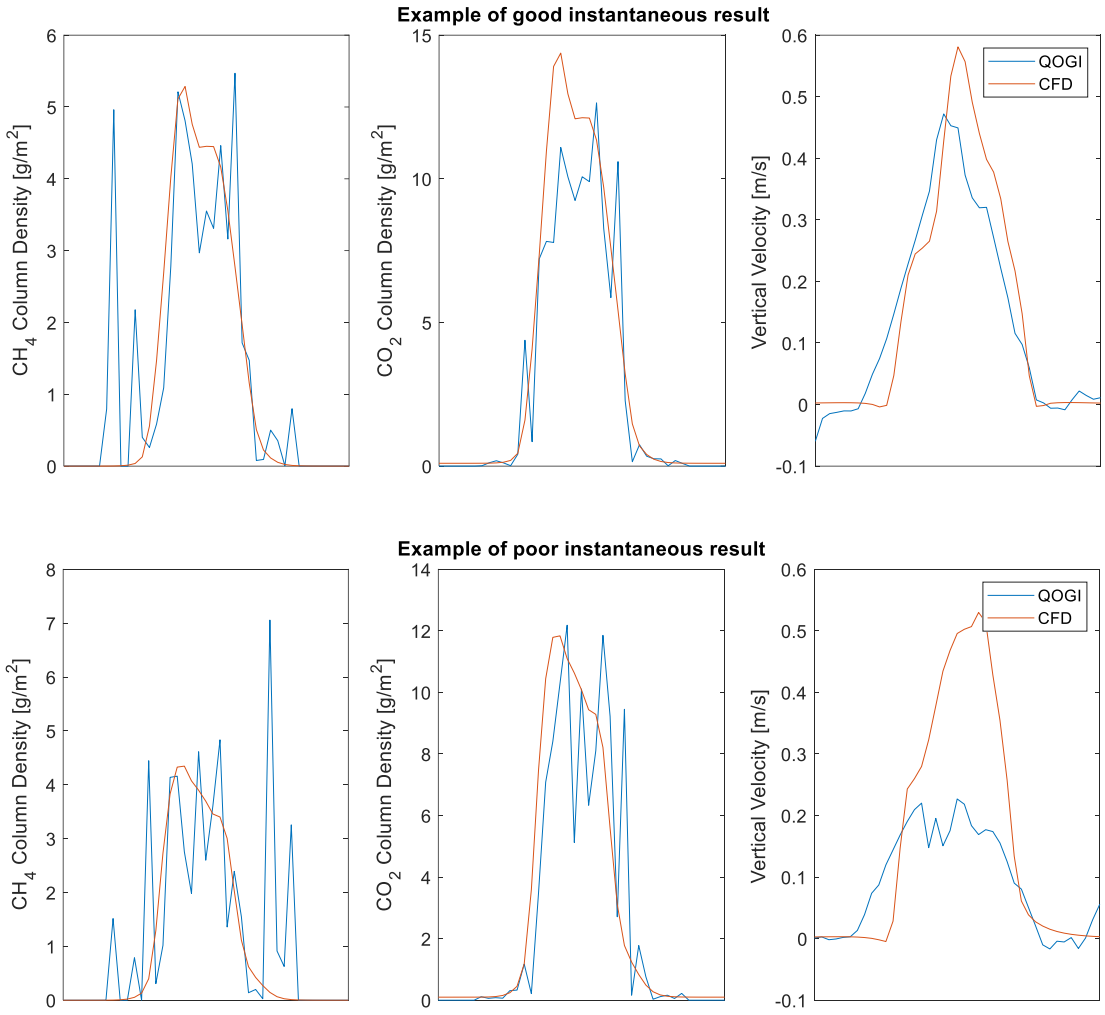

Figure 46: Sample instantaneous QOGI and CFD column densities and velocities

Figure 47 shows the instantaneous flow rates of CH_4 and CO_2 obtained by multiplying the column densities and velocities and integrating across the control surface as in Equation (12). Note that the average flow rates shown in Figure 47 are slightly different than those shown in Table 6. This is because the results in Table 6 are obtained by inferring the column densities of the time-averaged pixel intensities while the results in Figure 47 are obtained by inferring the instantaneous column densities then averaging over time. The former approach can be considered more accurate because the Gaussian

plume profile assumption along the LOS is truer when averaging the pixel intensities over time, while the latter approach can be considered more accurate because a true average flow rate should be calculated from the instantaneous rates. Inferring based on the averaged pixel intensities also has the advantage of reduced computation time for the spectroscopic model.

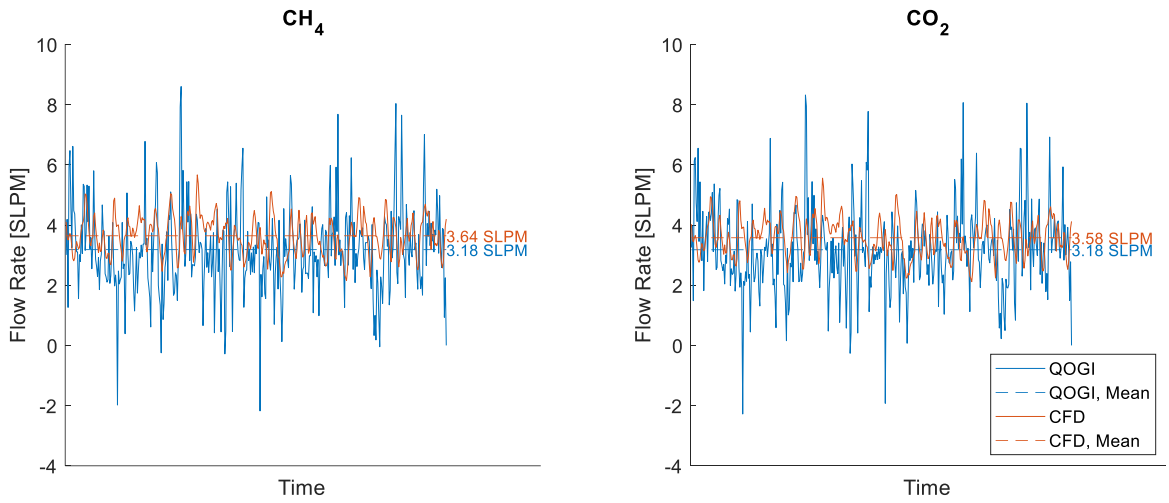

Figure 47: Instantaneous flow rates of QOGI and CFD ground truth

The effect of the inconsistency in the optical flow velocities is evident by the large fluctuations in the instantaneous flow rates. Improving the velocimetry would provide the most benefit to the QOGI accuracy in this case.

4.3.3 Effect of filter emission

The effect of filter emission can be included in the synthetic images by calculating the blackbody intensity at the filter temperature, multiplying by the filter emissivities, integrating over the wavelength range of the camera and adding the value to the true LOS intensity. In practice, the filter temperature cannot be known exactly, but a reasonable estimate would be ambient temperature, which is 20°C in the simulation. Figure 48 shows the pixels intensities across the control surface at height 3 for each

channel, with and without filter emission and FPA noise. Channel 1 sees a small increase in pixel intensities due to emission from the lens but as shown by the calculations in Table 4, this bias is small enough to be corrected with calibration. Channels 2, 3, and 4 show much larger increases in pixel intensities due to filter emission.

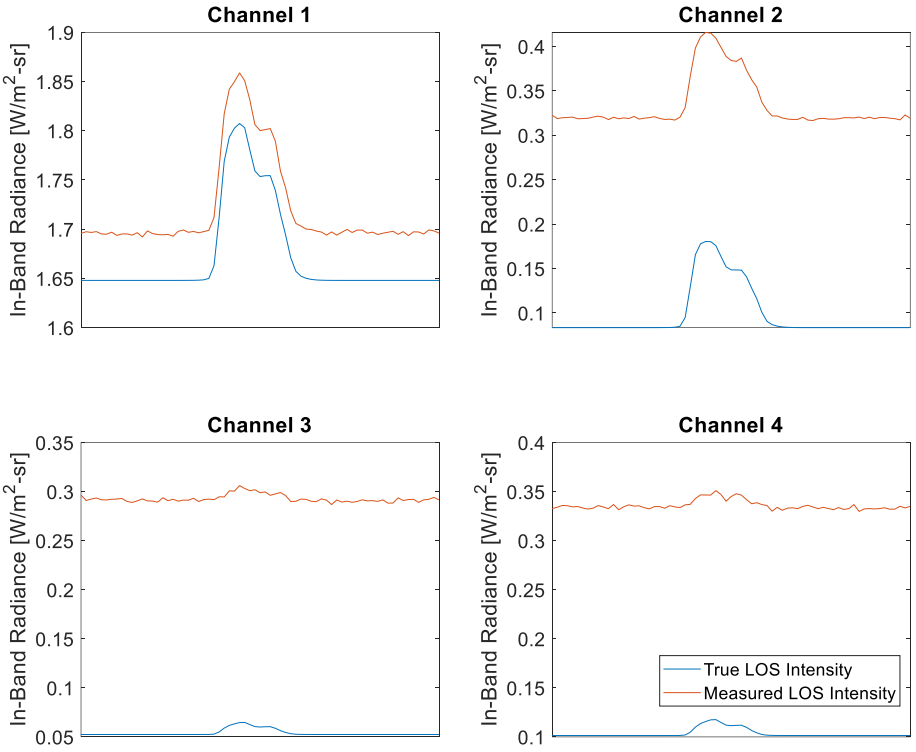

Figure 48: Pixel intensities across a control surface when including filter emission in synthetic images

Figure 49 shows the non-dimensionalized parameters inferred using these pixel intensities which reveals that the solution is unrealistic since the peak temperature exceed the upper bound of 90°C and the plume thickness is 90 to 100% of the 14 cm LOS distance. Figure 50 shows an example of the measured intensities across each channel for a single pixel versus the modeled intensities which are the resulting pixel intensities from the inferred volume fractions, temperature, and plume thickness. This shows that the residuals from the least-squares minimization are very large; the modeled pixel

intensities in the filtered channels are much lower than the measured intensities and vice-versa for the unfiltered channel. This demonstrates why QOGI is unfeasible with uncooled filters.

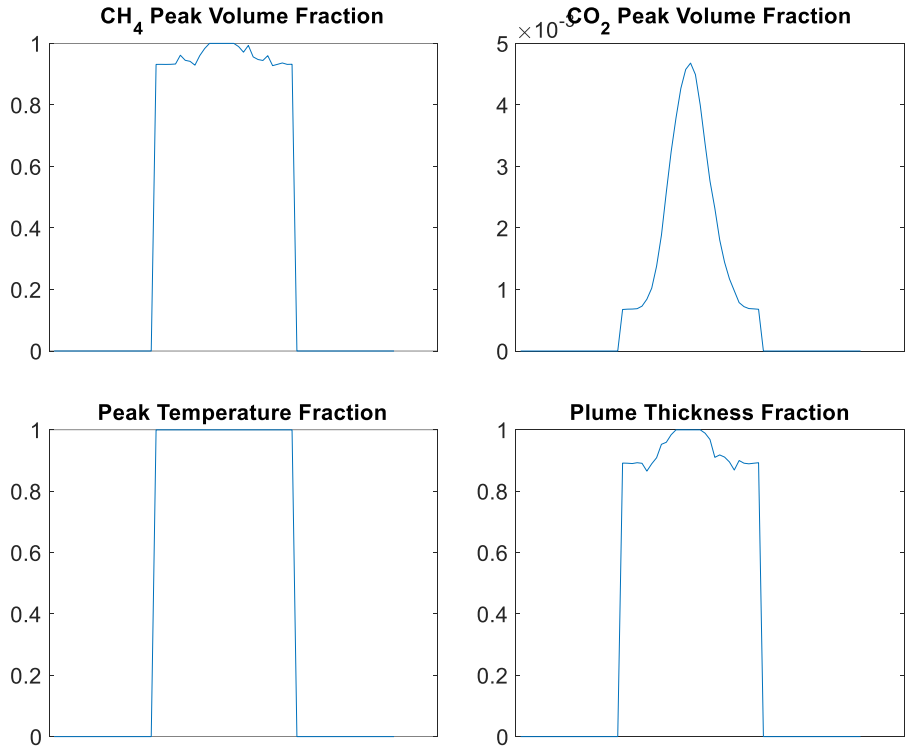

Figure 49: QOGI-inferred non-dimensional parameters for synthetic images including filter emission

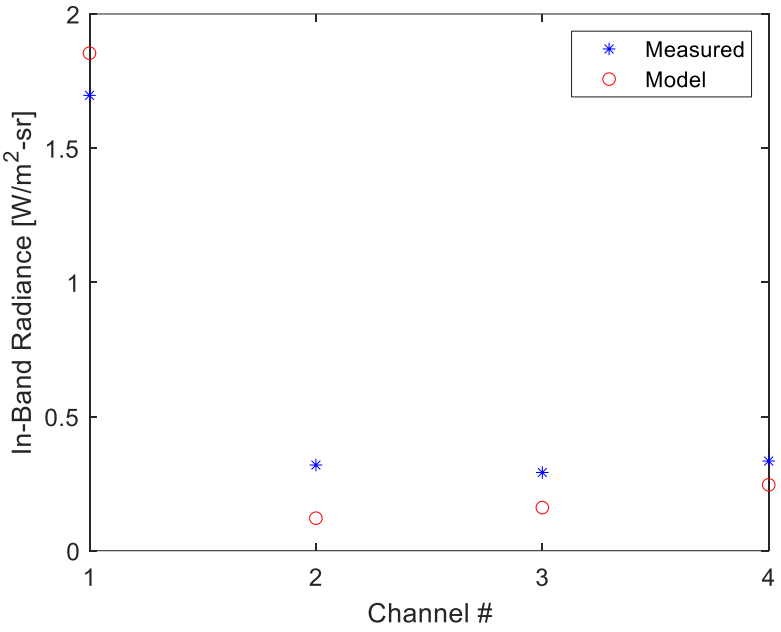

Figure 50: Measured versus modeled pixel intensities for a sample pixel when including filter emission in synthetic images

4.4 Chapter summary

This chapter focused on QOGI using multispectral broadband MWIR imaging. The Telops FAST M150 4-position filter wheel camera was tested first using the lab-scale controlled release apparatus after measuring the filter and lens transmittances using an FTIR to improve the accuracy of the spectroscopic model. Initial observations of the calibrated radiometric temperature and in-band radiance data revealed that the filtered channels were not producing accurate values at low temperatures. It was hypothesized that emission from the ambient temperature filters was biasing the measurements. A manual calibration was performed indoors at 21°C and outdoors at 8°C which would cool the filters. The resulting calibration curves demonstrated a decrease in signal corresponding to the reduction in filter emission, but the amount of cooling was insufficient when the QOGI analysis was repeated outdoors. The optical flow velocimetry at 100 Hz was reasonably successful but is believed to slightly underestimate the

actual gas velocities. Thus, the lab-scale experimental testing was able to only partially validate the multispectral QOGI camera and algorithms.

Due to the limited filter selection and calibration ranges of the FAST M150, field testing of the multispectral camera focused on qualitative observations of a flare and combustor and an attempt at optical flow velocimetry. Identifying the different combustion products and potentially unburned methane from the flare and combustor was not possible due to the unsynchronized image acquisition of the fixed filter wheel. Optical flow velocimetry of the flare at a 200 Hz frame rate was successful with a maximum velocity of 7 m/s when the wind speed was about 4 m/s gusting up to 6 m/s. A multispectral camera with sequential or simultaneous acquisition capabilities would be preferred for instantaneous QOGI analysis.

A CFD-LES simulation of a heated CH_4 and CO_2 plume was used along with a hypothetical model of the FAST M150 with cooled filters to generate synthetic images that could be analyzed using the multispectral QOGI algorithms. The multispectral QOGI analysis on the simulated data was able to infer CH_4 and CO_2 column densities and temperatures simultaneously. The QOGI estimates underpredicted the actual flow rates by 11% to 42%, mostly below 20% in error. The inferred column densities were shown to be very accurate, and the error in flow rate was largely due to fluctuations in the optical flow velocimetry which was unable to accurately estimate the velocity field in many frames. The effect of warm filters was simulated by adding the filter emission to the synthetic images and this further showed that QOGI is not feasible with uncooled filters.

This chapter demonstrated the unique capabilities and accuracy of multispectral QOGI, highlighted the need for a cooled filter multispectral camera with sequential or simultaneous acquisition, and the potential for improvements to the optical flow velocimetry algorithms.

Chapter 5

Conclusions

5.1 Summary of Thesis

OGI using MWIR cameras has become the standard for LDAR surveys in the oil and gas industry. Emissions quantification is needed to understand the impact of upstream oil and gas on climate change and work towards the global commitments made to reduce emissions and ultimately achieve a net-zero sustainable future. Methane is a potent GHG that has received special attention from researchers and regulators as studies revealed significant, unaccounted emissions of methane from oil and gas facilities. Many screening and quantification technologies are being employed to address the problem but more work is needed to assess their performance, especially in terms of quantification. QOGI is well-suited as a remote sensing technique but so far mostly single-channel broadband MWIR systems are found in industry. These QOGI systems are highly sensitive to uncertain gas temperature and their accuracy has not been studied adequately.

This thesis has developed a spectroscopic and optical flow velocimetry model to quantify emission rates using single-channel and multispectral broadband MWIR cameras. The algorithms were first validated using a FLIR GF320 single-channel MWIR camera using a controlled release apparatus with methane at ambient temperature. The inferred column densities were reasonable but the optical flow velocimetry was unsuccessful due to the 15 Hz frame rate of the camera. When using an average velocity based on the flow rate and exit diameter, the QOGI estimate was 21% less than the actual flow rate near the stack exit where the assumed velocity is more accurate and up to 60% less further from the exit. The QOGI algorithms were benchmarked against the FLIR QL320 tablet-based quantification system and achieved similar performance depending on the choice of settings in the tablet. The choice

of wind speed range had a significant impact on the flow rate estimate, likely due to changes in the cross-correlation velocimetry algorithm employed by the QL320. The effect of uncertain gas temperature was also tested by heating the methane with a heated hose. Using the gas temperature measured at the exit with a thermocouple, the QOGI algorithms overpredicted the actual flow rate by 21 to 37%. The QL320 was tested by specifying two temperatures: the gas temperature measured at the exit and the ambient temperature. Depending on the choice of temperature, the estimates were between 5-times higher and 5-times lower than the actual flow rate, demonstrating the importance of gas temperature in QOGI. Field testing was performed using the FLIR GF320, QL320, and QOGI algorithms. At a relatively low flow rate of 5 kg/hr, the QL320 underpredicted the actual flow rate by 49% while the QOGI algorithms overpredicted by 400% due to the downwash of the methane into the wake of the stack and the use of wind speed in-lieu of velocimetry. At higher flow rates of 20 to 50 kg/hr, the QL320 underpredicted the actual flow rate by 46% and the QOGI algorithms underpredicted by 35%. Comparing the inferred column densities to those estimated by a Gaussian dispersion model suggest that the column densities are underpredicted while the use of wind speed overestimates the gas velocity close to the stack.

Multispectral MWIR imaging was tested using the Telops FAST M150 which is a four-filter fixed-position filter wheel camera. The filters were measured using an FTIR to construct the spectroscopic model. Initial lab-scale experimental validation tried to quantify heated CH_4 and CO_2 simultaneously to maximize the capabilities of the multispectral camera. It was discovered that emission from the uncooled filters was significant for the scene temperatures being observed which made QOGI unfeasible. Manual calibration was attempted with the camera outdoors at 8°C which reduced the filter emission but it was still insufficient for accurate QOGI. Performance of the optical flow velocimetry was better due to the 100 Hz frame rate used but were lower than the expected velocities based on the

average exit velocity and manually tracking turbulent structures in the flow. Field measurements using the multispectral camera focused on qualitatively assessing a flare and combustor since four filters were inadequate to characterize the main combustion products and temperature for QOGI. Measurements were challenging due to the wide range of temperatures in the scene which made a single exposure time suboptimal. The multispectral images might have been able to separate the presence of water vapour and soot qualitatively but the unsynchronized images made definitive conclusions impossible. Optical flow velocimetry on the flare performed well with an estimated peak velocity of 7 m/s which is comparable to the wind speeds of 4 to 6 m/s. To avoid the limitations of the uncooled, fixed-position filters of the FAST M150, synthetic images were generated using a CFD-LES simulation of a heated CH_4 and CO_2 release. QOGI on the synthetic images performed very well and underpredicted the ground truth flow rates by 11% to 42%. The optical flow velocimetry was the main source of error due an inability to accurately estimate the velocity in many frames.

5.2 Proposed Future Work

Several challenges were encountered throughout this research which leads to the following proposals for future work.

5.2.1 Multispectral MWIR camera advancements

Two major shortcomings were demonstrated by this research using the Telops FAST M150 multispectral camera: warm filter emission makes QOGI of low temperature gases impossible; and unsynchronized acquisition between spectral bands necessitates time-averaging of measurements, which prevents detailed analysis of the instantaneous plume dynamics. Cooled filter multispectral cameras with rotating filter wheels or split FPAs should be developed to eliminate these problems and enable robust QOGI estimates. The LWIR multispectral camera prototype developed by ONERA

appears to achieve this with cryogenically cooled filters and a split FPA to image the four filters simultaneously [42]. This development is encouraging and should address the two shortcomings of the FAST M150, so it is recommended that this camera be tested independently using similar methods outlined in this thesis. That is, lab-scale experimental testing of a controlled methane release at non-ambient temperature and potentially other gas species to utilize the full multispectral capability. The ONERA camera operates in the LWIR (7 – 12 μm) which means it would not be able to image CO_2 for an application such as flare combustion efficiency. Nonetheless, a MWIR version could be designed using the same principles and a different FPA for different applications.

Additional advancements to MWIR cameras may come in the form of FPA manufacturing improvements. The resolution of the FPA can be improved by reducing the pixel pitch so that more pixels can fit onto the same size sensor. The manufacturing of the MWIR semiconductor materials can also improve to increase their sensitivity and reduce noise. These are less critical to the advancement of multispectral QOGI compared to cooled filter, synchronized acquisition capabilities.

5.2.2 Improve velocimetry model

This research has indicated that the velocimetry model is often the largest source of error in QOGI estimates. Prioritizing future work to improve the velocimetry model would be most beneficial to QOGI. Optical flow velocimetry was used throughout this research because of its ease of implementation and open-source availability. However, image correlation velocimetry and machine vision approaches should also be explored in detail. The cross-correlation velocimetry algorithms used by the QL320 are clearly superior to optical flow when applied to images acquired at 15 Hz, but this may be due to optimization of the algorithms for the QL320 application rather than an inherent performance advantage. Ideally more information on the QL320 velocimetry algorithms should be

made available publicly so that the field of QOGI may benefit from knowledge of the current state-of-the-art. Higher frame rate cameras would surely benefit velocimetry, but there will be a point of diminishing returns where higher frames rates only increase computational time and file size without any improvement in accuracy.

The optical flow velocimetry used in this research may benefit from optimization for QOGI, such as a parametric study of the optimal frame rate, resolution, and regularization parameter for a given gas velocity. Additional algorithms may be developed to mitigate the velocity field fluctuations observed in many frames such as an outlier rejection function. A plume dispersion model that couples the velocities and column densities could also serve as an additional prior that improves the accuracy of the velocimetry.

5.2.3 Integrate instantaneous plume dynamics

The accuracy of the spectroscopic model when analyzing single frames can be improved by considering the instantaneous plume dynamics, which do not follow Gaussian distributions. In this research the LOS distribution is assumed to be Gaussian which is true on average but not at a given instant. Bayesian inference could be used wherein simulated data of a plume is used to generate the likelihood and prior probability of the LOS distribution of the species volume fraction and temperature, and then the posterior probability of the column density given the measured pixel brightness will be

$$\mathrm{P}(\rho \mid \mathrm{b}) = \frac{\mathrm{P}(\mathrm{b} \mid \rho)\,\mathrm{P}_{\mathrm{pr}}(\rho, \chi(\mathrm{s}), \mathrm{T}(\mathrm{s}))}{\mathrm{P}(\mathrm{b})} \tag{17}$$

where ρ is the column density, b is the pixel brightness, P(b|ρ) is the likelihood of measuring the pixel brightness for a given column density, P_{pr} are the prior probabilities of the column densities and LOS distributions, and P(b) is the probability of measuring a given pixel brightness. This effectively

considers a wider range of LOS distributions which exist when analyzing the instantaneous plume dynamics, and provides a framework for uncertainty quantification of the column density since it will be expressed as a probability density function.

5.2.4 More rigorous error and uncertainty quantification

More rigorous error and uncertainty quantification of QOGI needs to be performed as QOGI continues to be adopted in the field and in legislation. This thesis provided a methodology for doing controlled release experiments and synthetic image generation using CFD-LES data to estimate the error associated with QOGI, but more experiments are needed to yield statistically significant estimates of QOGI accuracy. A detailed design of experiments to test the accuracy of QOGI technology and models while isolating variables would be beneficial, especially using the methodology of synthetic image generation where the ground truth is known exactly. Field measurements are also very important because the accuracy of QOGI will change depending on real-world conditions. The PTAC- and CRIN-funded project that is being conducted in parallel with this research aims to assess the performance of QOGI under industrially-relevant conditions and ultimately obtain a quantification of uncertainty for the technology. Such work is of vital importance and lacks sufficient study by the current state-of-the-art, likely due to the recency of QOGI.

References

[1] "World Energy Production," *Enerdata*, 2021. https://yearbook.enerdata.net/total-energy/world-energy-production.html

[2] "Energy Mix," *Our World in Data*, 2021. https://ourworldindata.org/energy-mix

[3] "2030 Emissions Reduction Plan: Clean Air, Strong Economy," *Government of Canada*, Jul. 12, 2022. https://www.canada.ca/en/services/environment/weather/climatechange/climate-plan/climate-plan-overview/emissions-reduction-2030.html

[4] S. Solomon and Intergovernmental Panel on Climate Change, *Climate Change 2007 - The Physical Science Basis*. Cambridge University Press, 2007.

[5] R. A. Alvarez, S. W. Pacala, J. J. Winebrake, W. L. Chameides, and S. P. Hamburg, "Greater focus needed on methane leakage from natural gas infrastructure," *Proceedings of the National Academy of Sciences*, vol. 109, no. 17, pp. 6435–6440, Apr. 2012, doi: 10.1073/PNAS.1202407109.

[6] A. R. Brandt *et al.*, "Methane Leaks from North American Natural Gas Systems," *Science (1979)*, vol. 343, no. 6172, pp. 733–735, 2014, doi: 10.1126/SCIENCE.1247045.

[7] R. A. Alvarez *et al.*, "Assessment of methane emissions from the U.S. oil and gas supply chain," *Science (1979)*, vol. 361, no. 6398, pp. 186–188, Jul. 2018, doi: 10.1126/SCIENCE.AAR7204.

[8] "Greenhouse gas sources and sinks in Canada: executive summary 2022," *Government of Canada*, Jul. 22, 2022. https://www.canada.ca/en/environment-climate-change/services/climate-change/greenhouse-gas-emissions/sources-sinks-executive-summary-2022.html

[9] "Natural Gas Explained," *U.S. Energy Information Administration*, 2022. https://www.eia.gov/energyexplained/natural-gas/where-our-natural-gas-comes-from.php.

[10] J. S. Rutherford *et al.*, "Closing the methane gap in US oil and natural gas production emissions inventories," *Nat Commun*, vol. 12, no. 1, Dec. 2021, doi: 10.1038/s41467-021-25017-4.

[11] D. R. Tyner and M. R. Johnson, "Where the Methane Is - Insights from Novel Airborne LiDAR Measurements Combined with Ground Survey Data," *Environ Sci Technol*, vol. 55, no. 14, pp. 9773–9783, Jul. 2021, doi: 10.1021/acs.est.1c01572.

[12] T. A. Fox, T. E. Barchyn, D. Risk, A. P. Ravikumar, and C. H. Hugenholtz, "A review of close-range and screening technologies for mitigating fugitive methane emissions in upstream oil and gas," *Environmental Research Letters*, vol. 14, no. 5, May 2019, doi: 10.1088/1748-9326/AB0CC3.

[13] C. S. Bell, T. Vaughn, and D. Zimmerle, "Evaluation of next generation emission measurement technologies under repeatable test protocols," *Elementa: Science of the Anthropocene*, vol. 8, Jan. 2020, doi: 10.1525/elementa.426.

[14] A. Daniels, *Field Guide to Infrared Systems, Detectors, and FPAs*, Third Edition. Bellingham: SPIE Press, 2018.

[15] A. Rogalski, "Infrared detectors: an overview," *Infrared Phys Technol*, vol. 43, no. 3–5, pp. 187–210, 2002, doi: 10.1016/S1350-4495(02)00140-8.

[16] D. A. Scribner, M. R. Kruer, and J. M. Killiany, "Infrared Focal Plane Array Technology," in *Proceedings of the IEEE*, Jan. 1991, vol. 79, no. 1, pp. 66–85. doi: 10.1109/5.64383.

[17] C. C. Hsieh, C. Y. Wu, F. W. Jih, and T. P. Sun, "Focal-plane-arrays and CMOS readout techniques of infrared imaging systems," *IEEE Transactions on Circuits and Systems for Video Technology*, vol. 7, no. 4, pp. 594–605, Aug. 1997, doi: 10.1109/76.611171.

[18] D. F. Flanigan, "Detection of organic vapors with active and passive sensors: a comparison," *Applied Optics, Vol. 25, Issue 23, pp. 4253-4260*, vol. 25, no. 23, pp. 4253–4260, Dec. 1986, doi: 10.1364/AO.25.004253.

[19] T. J. Kulp, P. E. Powers, and R. B. Kennedy, "Remote imaging of controlled gas releases using active and passive infrared imaging systems," in *Proceedings of SPIE, Infrared Technology and Applications*, Aug. 1997, vol. 3061. doi: 10.1117/12.280321.

[20] "Reduction in the Release of Volatile Organic Compounds Regulations (Petroleum Sector)," *Government of Canada*, Oct. 26, 2020. https://laws-lois.justice.gc.ca/eng/regulations/SOR-2020-231/page-1.html

[21] P. Powers, R. Kennedy, T. J. Kulp, and U.-B. Goers, "Development of a pulsed backscatter-absorption gas-imaging system and its application to the visualization of natural gas leaks," *Appl Opt*, vol. 37, no. 18, pp. 3912–3922, Jun. 1998, doi: 10.1364/AO.37.003912.

[22] K. J. Nutt, N. Hempler, G. T. Maker, G. P. A. Malcolm, M. J. Padgett, and G. M. Gibson, "Developing a portable gas imaging camera using highly tunable active-illumination and computer vision," *Opt Express*, vol. 28, no. 13, pp. 18566–18576, Jun. 2020, doi: 10.1364/OE.389634.

[23] S.-A. Ljungberg, T. Kulp, T. McRae Sven-Ake Ljungberg, T. J. Kulp, and T. G. McRae, "State of the art and future plans for IR imaging of gaseous fugitive emissions," in *Proceedings of SPIE*, Apr. 1997, vol. 3056, no. 4. doi: 10.1117/12.271624.

[24] Edward Naranjo, S. Baliga, P. Bernascolle, and E. Naranjo, “IR gas imaging in an industrial setting,” in *Proceedings of SPIE*, May 2010, vol. 7661, no. 3, pp. 160–167. doi: 10.1117/12.850137.

[25] D. Furry, A. Richards, R. Lucier, and R Madding, “Detection of volatile organic compounds (VOC’s) with a spectrally filtered cooled mid-wave infrared camera,” in *InfraMation Proceedings*, 2005. doi: 10.1038/s41598-022-09597-9.

[26] M. Kastek, T. Sosnowski, T. Orzanowski, K. Kopczyński, and M. Kwaśny, “Multispectral gas detection method,” in *Air Pollution*, 2009, vol. 123, pp. 227–236. doi: 10.2495/AIR090211.

[27] S. Sabbah, R. Harig, P. Rusch, J. Eichmann, A. Keens, and J.-H. Gerhard, “Remote sensing of gases by hyperspectral imaging: system performance and measurements,” *Optical Engineering*, vol. 51, no. 11, p. 111717, Jul. 2012, doi: 10.1117/1.OE.51.11.111717.

[28] M. A. Rodríguez-Conejo and J. Meléndez, “Hyperspectral quantitative imaging of gas sources in the mid-infrared,” *Appl Opt*, vol. 54, no. 2, pp. 141–149, Jan. 2015, doi: 10.1364/AO.54.000141.

[29] S. J. Grauer, B. M. Conrad, R. B. Miguel, and K. J. Daun, “Gaussian model for emission rate measurement of heated plumes using hyperspectral data,” *J Quant Spectrosc Radiat Transf*, vol. 206, pp. 125–134, Feb. 2018, doi: 10.1016/j.jqsrt.2017.11.005.

[30] M. Lev-On, H. Taback, D. Epperson, J. Siegell, L. Gilmer, and K. Ritter, “Methods for quantification of mass emissions from leaking process equipment when using optical imaging for leak detection,” *Environmental Progress*, vol. 25, no. 1, pp. 49–55, Apr. 2006, doi: 10.1002/EP.10102.

[31] A. Safitri, X. Gao, and M. S. Mannan, “Dispersion modeling approach for quantification of methane emission rates from natural gas fugitive leaks detected by infrared imaging technique,” *J Loss Prev Process Ind*, vol. 24, no. 2, pp. 138–145, Mar. 2011, doi: 10.1016/J.JLP.2010.11.007.

[32] J. Sandsten *et al.*, “Real-time gas-correlation imaging employing thermal background radiation.,” *Opt Express*, vol. 6, no. 4, pp. 92–103, Aug. 2000, doi: 10.1364/OE.6.000092.

[33] Y. Zeng and J. Morris, “Calibration and Quantification Method for Gas Imaging Camera,” 2016

[34] H. Abdel-Moati, J. Morris, Y. Zeng, P. Kangas, and D. McGregor, “New Optical Gas Imaging Technology for Quantifying Fugitive Emission Rates,” in *International Petroleum Technology Conference*, Dec. 2015. doi: 10.2523/IPTC-18471-MS.

[35] J. Sandsten and M. Andersson, “Volume flow calculations on gas leaks imaged with infrared gas-correlation,” *Opt Express*, vol. 20, no. 18, pp. 20318–20329, Aug. 2012, doi: 10.1364/OE.20.020318.

[36] N. Hagen, “Survey of autonomous gas leak detection and quantification with snapshot infrared spectral imaging,” *Journal of Optics*, vol. 22, no. 10, Sep. 2020, doi: 10.1088/2040-8986/ABB1CF.

[37] “Opgal EyeCSite - Quantitative Optical Gas Imaging (QOGI) Software,” *Opgal*. https://www.opgal.com/products/eyecsite/

[38] C. Caico *et al.*, “An evaluation of an optical gas imaging system for the quantification of fugitive hydrocarbon emissions,” 2017.

[39] Y. Zeng, J. Morris, A. Sanders, S. Mutyala, and C. Zeng, “Methods to determine response factors for infrared gas imagers used as quantitative measurement devices,” *J Air Waste Manage Assoc*, vol. 67, no. 11, pp. 1180–1191, Nov. 2017, doi: 10.1080/10962247.2016.1244130.

[40] L. Jackiw, “Verification of Quantitative Optical Gas Imaging System,” 2018.

[41] A. P. Ravikumar, D. Singh, B. Barlow, C. Robinson, and W. Funk, “Alberta Methane Field Challenge,” Aug. 2020.

[42] G. Druart *et al.*, “Test of SIMAGAZ: a LWIR cryogenic multispectral infrared camera for methane gas leak detection and quantification,” in *Proceedings of SPIE*, Apr. 2021, vol. 11727. doi: 10.1117/12.2586933.

[43] J. Meléndez and G. Guarnizo, “Multispectral Mid-Infrared Camera System for Accurate Stand-Off Temperature and Column Density Measurements on Flames,” *Sensors 2021, Vol. 21, Page 8395*, vol. 21, no. 24, p. 8395, Dec. 2021, doi: 10.3390/S21248395.

[44] M. Gålfalk, G. Olofsson, and D. Bastviken, “Approaches for hyperspectral remote flux quantification and visualization of GHGs in the environment,” *Remote Sens Environ*, vol. 191, pp. 81–94, Mar. 2017, doi: 10.1016/J.RSE.2017.01.012.

[45] T. Ren, M. F. Modest, A. Fateev, G. Sutton, W. Zhao, and F. Rusu, “Machine learning applied to retrieval of temperature and concentration distributions from infrared emission measurements,” *Appl Energy*, vol. 252, p. 113448, Oct. 2019, doi: 10.1016/J.APENERGY.2019.113448.

[46] T. Ouyang *et al.*, “NOx Measurements in Vehicle Exhaust Using Advanced Deep ELM Networks,” *IEEE Trans Instrum Meas*, vol. 70, pp. 1–10, 2021, doi: 10.1109/TIM.2020.3013129.

[47] J. Wang *et al.*, “Machine vision for natural gas methane emissions detection using an infrared camera,” *Appl Energy*, vol. 257, p. 113998, Oct. 2020, doi: 10.1016/j.apenergy.2019.113998.

[48] A. P. Ravikumar, J. Wang, M. McGuire, C. S. Bell, D. Zimmerle, and A. R. Brandt, “‘Good versus Good Enough?’ Empirical Tests of Methane Leak Detection Sensitivity of a Commercial Infrared Camera,” *Environ Sci Technol*, vol. 52, no. 4, pp. 2368–2374, Feb. 2018, doi: 10.1021/acs.est.7b04945.

[49] Y. Zeng and J. Morris, “Detection limits of optical gas imagers as a function of temperature differential and distance,” *J Air Waste Manage Assoc*, vol. 69, no. 3, pp. 351–361, Mar. 2019, doi: 10.1080/10962247.2018.1540366.

[50] D. Zimmerle, T. Vaughn, C. Bell, K. Bennett, P. Deshmukh, and E. Thoma, “Detection Limits of Optical Gas Imaging for Natural Gas Leak Detection in Realistic Controlled Conditions,” *Environ Sci Technol*, vol. 54, no. 18, pp. 11506–11514, Sep. 2020, doi: 10.1021/acs.est.0c01285.

[51] A. Montazeri, X. Zhou, and J. D. Albertson, “On the viability of video imaging in leak rate quantification: A theoretical error analysis,” *Sensors*, vol. 21, no. 17, p. 5683, Aug. 2021, doi: 10.3390/s21175683.

[52] J. R. Howell, M. Pinar Mengüç, K. Daun, and R. Siegel, *Thermal Radiation Heat Transfer*, Seventh Edition. CRC Press, 2021.

[53] L. S. Rothman *et al.*, “The HITRAN2012 molecular spectroscopic database,” *J Quant Spectrosc Radiat Transf*, vol. 130, pp. 4–50, Nov. 2013, doi: 10.1016/J.JQSRT.2013.07.002.

[54] B. K. P. Horn and B. G. Schunck, “Determining Optical Flow,” *Artif Intell*, vol. 17, no. 1–3, pp. 185–203, 1981.

[55] B. D. Lucas and T. Kanade, “An Iterative Image Registration Technique with an Application to Stereo Vision,” in *Proceedings of Imaging Understanding Workshop*, 1981, pp. 121–130.

[56] P. Tremblay *et al.*, “Pixel-wise real-time advanced calibration method for thermal infrared cameras,” in *Proceedings of SPIE*, Apr. 2010, vol. 7662, p. 766212. doi: 10.1117/12.850560.

[57] Infrared Training Center, “Optical Gas Imaging Course Manual.” Pub ITC, Burlington, Apr. 01, 2019.

[58] J. H. Perry and C. v. Herrmann, “The Joule-Thomson effect of methane, nitrogen, and mixtures of these gases,” *Journal of Physical Chemistry*, vol. 39, no. 8, pp. 1189–1195, 1935, doi: 10.1021/J150369A003.

[59] D. R. Caulton *et al.*, “Quantifying uncertainties from mobile-laboratory-derived emissions of well pads using inverse Gaussian methods,” *Atmos Chem Phys*, vol. 18, no. 20, pp. 15145–15168, Oct. 2018, doi: 10.5194/acp-18-15145-2018.

[60] A. D. van Rheenen, E. Brendhagen, and L. T. Heen, “Comparison of distance dependence of ship signature and intensity of ship exhaust gas measured in both MWIR and LWIR transmission bands,” in *Proceedings of SPIE*, Sep. 2009, vol. 7476, p. 747605. doi: 10.1117/12.830317.

[61] R. M. Brenner, “Quantification of Flare Combustion Efficiency through Mid-Wavelength Infrared Spectroscopy,” University of Waterloo, 2022.

[62] S. J. Brookes and J. B. Moss, “Measurements of soot production and thermal radiation from confined turbulent jet diffusion flames of methane,” *Combust Flame*, vol. 116, no. 1–2, pp. 49–61, 1999, doi: 10.1016/S0010-2180(98)00027-3.

[63] D. J. Corbin and M. R. Johnson, “Detailed expressions and methodologies for measuring flare combustion efficiency, species emission rates, and associated uncertainties,” *Ind Eng Chem Res*, vol. 53, no. 49, pp. 19359–19369, Nov. 2014, doi: 10.1021/IE502914K.

[64] I. Glassman, R. A. Yetter, and N. Glumac, “Combustion,” 5th ed., 2015, pp. 438–466.

[65] “Fire Dynamics Simulator (FDS) and Smokeview (SMV),” *National Institute of Standards and Technology*. https://pages.nist.gov/fds-smv/

[66] J. M. Lopez-Alonso, “Noise Equivalent Temperature Difference (NETD),” in *Encyclopedia of Optical Engineering*, CRC Press, 2003, pp. 1466–1474.

[67] “How is NEDT measured?,” *Teledyne FLIR*. https://www.flir.com/support-center/Instruments/how-is-nedt-measured/